ANALYSIS OF WAVEFORM DISTORTIONS PRODUCED BY INTERFEROMETER RESPONSE FUNCTIONS FOR FUTURE SEARCHES OF GRAVITATIONAL-WAVE SIGNALS FROM CORE-COLLAPSE SUPERNOVAE

by

ANTON GRIBOVSKIY

DISSERTATION

Submitted in partial fulfillment of the requirements
of the degree of Doctor of Philosophy at
The University of Texas at Arlington
May, 2021

Arlington, Texas

Supervising Committee:

Malik Rakhmanov, Supervising Professor
Zdzislaw Musielak
Manfred Cuntz
Ramon Lopez
Soumya Mohanty

ABSTRACT

Analysis of Waveform Distortions Produced by Interferometer Response Functions for Future Searches of Gravitational-Wave Signals from Core-Collapse Supernovae

Anton Gribovskiy, PhD

The University of Texas at Arlington, 2021

Supervising Professor: Malik Rakhmanov

Multi-messenger astronomy recently added a fundamentally new component to its wide array of observational tools: a gravitational-wave detector. A number of binary black holes mergers have already been detected by gravitational-wave interferometers and the data have been analyzed by the scientific community. Moreover, simultaneous observation of gravitational waves with electromagnetic signals led to the first observation of a binary neutron star merger. Success in gravitational-wave detection motivated the efforts to improve current detectors and initiated the design of future detectors with significantly enhanced sensitivities. The detector improvements will lead to increase of the detection range for binary star mergers and will also allow observation of new sources. One of the most sought-after sources is the core-collapse supernova. According to extensive numerical simulations, gravitational-wave signals emitted during the core collapse can have frequencies in the kilohertz range, approaching the free spectral range of Fabry-Pérot arms of future detectors. The long-wavelength approximation, commonly used in the analysis of gravitational-wave interferometers, is not applicable in this regime. Therefore, it is necessary to develop new approaches to calculate waveform deformations, to analyze interferometer responses, and to estimate their implications for calibration for these large-scale detectors.

We utilize the time-domain interferometer impulse response and Fourier-Laplace domain transfer function of gravitational wave detectors without any limitation on the maximum frequency of the signal. These tools will allow us to develop a general theory for waveform deformations as the signal propagates through the interferometer arms. In particular, we analyze the time of arrival of the gravitational wave and show that in addition to the geometrical delay due to the detector location

on Earth, it has an additional contribution originating from the interferometer transfer function. Accurate calculation of the signal arrival time is important for the determination of the source position on the sky. We analyze this intrinsic delay for different interferometer configurations and present the results as sky-maps for two polarizations of the gravitational wave. In this work we give the classification of various waveform distortions of the signal for applications to searches of gravitational waves from core-collapse supernovae. We analyzed in detail three different features commonly present in numerical waveforms of the supernova. These features are the core bounce, the SASI modes, and the core oscillations. For each of these features we analyze the time delays, the frequency shifts, signal-envelope broadening, and the signal-frequency chirps. In addition to the analytical calculations, we developed numerical simulations of the interferometric gravitational-wave detection to assess accuracy of analytical approximations we used. Good agreement found in almost all cases we considered. Moreover, we found that the detector properties and waveform deformations are largely controlled by the complex zeros of the interferometer response. The significance of the zeros motivated the development of algorithms for effective calculations of the zeros (real and imaginary parts) as functions of the sky location. Substantial difficulty in these calculations comes from the transcendental nature of the characteristic equation. Therefore, an algorithm was built on combination of analytical and numerical methods and used recursive techniques to attain the necessary precision. The results of this work can be used for understanding the waveform deformations of the core-collapse supernova signals, in the development of search algorithms for detection of supernovae gravitational-wave emissions, and for optimization of future gravitational-wave detectors.

ACKNOWLEDGEMENTS

I deeply appreciate my supervisor, Dr. Malik Rakhmanov, for his support and mentorship during my journey towards the Doctorate degree. His patience and guidance led me through all difficulties that I've encountered during my research. I've learned a lot during our numerous discussions about detection of gravitational waves.

I want to express gratitude to my dissertation committee members, Dr. Manfred Cuntz, Dr. Dr. Ramon Lopez, Dr. Soumya Mohanty, and Dr. Zdzislaw Musielak, for their time and valuable comments and corrections. Additionally, I want to thank UTA-UTRGV collaborative program coordinator, Dr. Qiming Zhang for his guidance through the procedure of dissertation defense.

Special thanks from me go to my friend and colleague Artemiy Bogdanovskiy for his emotional support and numerous discussions that we had together. I am very grateful to my mother, Lyudmila Gribovskaya, and my brother, Gleb Gribovskiy, for their support and care. Their undoubtful belief in my success helped me find strength to keep going and to not give up.

TABLE OF CONTENTS

Abstract ii

Acknowledgements v

List of Figures vii

Introduction 1

1 Detection of Gravitational Waves 10

1.1 General relativity . . . 10

1.2 Gravitational waves . . . 14

1.3 Gravitational waves from Core-Collapse Supernova . . . 16

1.4 Detection of gravitational waves . . . 21

1.5 Round-trip interferometer . . . 29

1.6 Michelson interferometer . . . 35

1.7 Detection prospects of CCSNe gravitational-wave signals . . . 42

2 Gravitational wave detector group delay 44

2.1 Complex phase of transfer function . . . 44

2.1.1 Sine-Gaussian signal . . . 47

2.1.2 Chirp signal . . . 48

2.2 Numerical estimation of signal parameters . . . 52

2.2.1 Definition for signal arrival time . . . 52

2.2.2 Instantaneous amplitude and frequency of a signal . . . 53

2.3 Group delay analysis . . . 54

2.4 Michelson interferometer group delay sky maps 59

3 Distortions of CCSN gravitational-wave signals 63

3.1 Second order approximation of the transfer function complex phase 63

3.2 Sources of distortions 65

3.3 Distortion of a short pulse 67

3.4 Distortion of a Sine-Gaussian wave packet 72

3.4.1 First order distortions: time shift and frequency shift 74

3.4.2 Second order distortions 80

3.5 Distortions of signals with changing frequency 81

4 Zeros of interferometer transfer function 87

4.1 One-arm detector 88

4.2 Round-trip interferometer critical points 93

4.3 Michelson Interferometer 96

4.4 Michelson interferometer critical points 99

5 Conclusions 103

References 107

LIST OF FIGURES

1 Gravitational-wave signals detected by Washington (left) and Louisiana (right) detectors on September 14, 2015. Top row shows time series of the signals after filtering. Second row shows the numerical relativity simulations. (The residual errors represent the difference between the data and the simulation.) Bottom row shows spectrograms of the signals. (The figure is from [7].) 4

2 Localization of the source performed by different detectors. The left panel shows localization regions from LIGO interferometers (light-green) an combined LIGO-Virgo network (dark green), Fermi and INTEGRAL satellites of IPN (light blue), and Fermi-GBM (dark blue). The top right panel shows the location of the source taken in the Swope optical telescope at 10.9 hours after the merger. Bottom right shows an image taken 20 days before the event on DLT-40 telescope. Position of the possible source is shown with the reticle mark. (The figure is from [20].) 5

1.1 Examples of numerical simulations of gravitational waves from rapidly-rotating CCSN. On the left there are time series (top) and spectrogram (bottom) of the signals made by Richers et al [37]. Top left panel shows waveforms from explosion of PNS with different rotational parameters. The spectrogram on bottom left panel corresponds to the case of PNS rotating at 9.5 rad/s. On the right there are time series (top) and spectrogram (bottom) of the waveform from the numerical simulation conducted by Cerda-Duran et al [38]. In this simulation the PNS was initially rotation with angular rate of 2 rad/s. The spectrogram on the bottom right shows the bounce and additional core oscillation modes that appear during the explosion. 17

1.2 Examples of numerical simulation of gravitational waves from slowly rotating CCSN. The left panel shows spectrogram of the waveforms from simulations made by Kuroda et al [40] for $15M_{\odot}$ progenitor. Additional overlay to this simulation shows fits to the f-mode and SASI. Frequency of the f-mode carries important information about the state of the PNS during the explosion, while development of SASI carries information about the equation of state. The right panel shows a spectrogram of the gravitational-wave signal from the simulation made by Radice et al [41] for a progenitor with mass $M = 9m_{\odot}$. The line on this spectrogram corresponds to f-mode as well as low lower g-modes, but signs of SASI mode are not present. 19

1.3 Laser beam in a one-arm detector. 29

1.4 Round-trip phase change response to delta (left) and step (right) functions for different source locations. We assume that the arm vector $\hat{\boldsymbol{a}}$ is perpendicular to the polarization vector $\hat{\boldsymbol{q}}$. 31

1.5 Propagation of a gravitational-wave front through an interferometer arm with length L. Blue line marks photons that are moving in the same direction with the gravitational-wave front when it reaches them. 33

1.6 Round-trip transfer function response for different angles between the arm and direction to the GW source. For acute angles phase response of the transfer function oscillates between 0° and −90°, while for obtuse angles phase response constantly decreasing. 34

1.7 Round-trip transfer function response on the complex plane. 35

1.8 Laser beam in a Michelson interferometer. 36

1.9 Coordinate system introduced for a Michelson interferometer with arm directions $\hat{\boldsymbol{a}}$ and $\hat{\boldsymbol{b}}$. Orthogonal axes $\hat{\boldsymbol{x}}$ and $\hat{\boldsymbol{y}}$ share the same bisector with the vectors $\hat{\boldsymbol{a}}$ and $\hat{\boldsymbol{b}}$. Azimuth angle ϕ and elevation angle θ set direction towards the source $\hat{\boldsymbol{n}}$. Vectors $\hat{\boldsymbol{p}}$ and $\hat{\boldsymbol{q}}$ are two polarization vectors of an incoming gravitational wave. 39

1.10 Michelson interferometer response to + polarization δ function. Left: source with optimal orientation $\phi = 0°$, $\theta = 90°$. Right: source with orientation $\phi = 135°$, $\theta = 0°$. 40

1.11 Michelson round-trip response to × polarization δ function. Left: source located at $\phi = 5°$, $\theta = 30°$, angle between interferometer arms $\alpha = 60°$. Right: source located at $\phi = 135°$, $\theta = 10°$, angle between interferometer arms $\alpha = 90°$. 41

2.1 Group delay and chirp delay dependence as a function of source location. Frequencies of the gravitational signals are normalized over FSR. These graphs show antisymmetric property of the group delay (left): when μ changes sign, group delay flips relative to time T. At the same time chirp delay (right) has symmetric property. 55

2.2 Group delay and chirp delay for different source location and high source frequencies. Group and chirp delays have more variance when frequency increases. 55

2.3 Frequency dependence of group delay and chirp delay for different source locations. When amplitude of the transfer function approaches zero, chirp delay of the interferometer becomes inversely proportional to the frequency. 56

2.4 Behavior of functions τ and γ next to critical points. The group delay drastically changes with small change of source location. The chirp delay drastically changes with small change of source frequency. 56

2.5 Distortion of a signal at carrier frequency 1 FSR by one-arm detector. Source location is at 89°. Derivative of phase of the interferometer transfer function is 27.7 T. 57

2.6 Detection of a gravitational wave signal with abrupt start. Input corresponds to the gravitational wave signal, output corresponds to the interferometer output. Right panel shows the moment when gravitational wave starts. 58

2.7 Group delay for a Gaussian packet with center frequency 0.8 FSR for Michelson interferometer. Top row: measured group delay of a signal plotted on a sphere. Middle row: measured group delay in cylindrical projection. Bottom row: analytical calculation of the group delay. Left panels show the group delay for + polarization and right panels show the group delay for × polarization. White line on the graph corresponds to the location of the source with zero group delay. 60

2.8 Group delay for different frequencies and polarizations. Top panels show group delay for + polarization. Bottom panels show group delay for × polarization. From left to right the signal frequency is 0.5, 0.7, 0.9, and 1.2 FSR. 61

2.9 Contour plot of the group delay for different frequencies and polarizations. Top panels show group delay for + polarization. Bottom panels show group delay for × polarization. From left to right the signal frequency is 0.5, 0.7, 0.9, and 1.2 FSR. 62

3.1 Example of a filter that signal passes through when pole of the transfer function is determined during the calibration with 5% error. Top: amplitude transfer function, bottom: phase transfer function. 66

3.2 Examples of distortion of a pulse by a Michelson interferometer for different frequencies and different source locations. The interferometer response was normalized to have the same amplitude for the largest peak. The azimuth and elevation of the source: top left (30°, 60°), top right (120°, 60°), bottom left (0°, 90°), bottom right (210°, 60°). . 67

3.3 Distortion of a symmetric (left) and an asymmetric (right) pulses by a single arm interferometer for pulse frequency equal to 4 FSR and source azimuth 135° and elevation 62°. On the left panel response is overlapped with the interferometer impulse response. Dash-dotted lines on the pictures show moments of arrival of the photons bounced from the end mirrors when signal passed through these mirrors. 69

3.4 Examples of distortion of a pulse by Michelson interferometer for different frequencies and different source locations. Here the frequencies are much higher than the FSR. The interferometer response was normalized to have the same maximum value as the original signal. Azimuth and elevation of the source: top left (30°, 60°), top right (120°, 60°), bottom left (0°, 90°), bottom right (210°, 60°). 70

3.5 Interferometer normalized response to symmetric and asymmetric signals with center frequency $f = 0.7 f_{\mathrm{rt}}$. On the left: original signal is symmetric, so response of the arm has symmetric property relative to the moment of time $t = 2.3T$. On the right original signal is antisymmetric, so response has antisymmetric property relative to the same moment of time. 72

3.6 The envelope of the response of a Michelson detector to Sine-Gaussian signal coming from a source with azimuth 30° and elevaton 60°. Left: full envelope, right: zoom to the top part of the envelope 76

3.7 The dependence of the interferometer group delay with frequency. The group delay is normalized over the photon one-way transit time. 76

3.8 The difference between the numerical simulation and analytical calculation of the group delay (top) and the frequency detuning (bottom). The calculations were made for the source located at (30°, 60°). The analytical calculations of the group delay show good agreement with the numerical simulations for all frequencies, while the analytical calculations of the frequency detuning have drastic difference with numerical simulations for the signal with frequency close to 3 FSR. 77

3.9 Instantaneous frequency detuning produced by a Michelson interferometer for different source location. Azimuth and elevation of the source: top left (30°, 60°), top right (120°, 60°), bottom left (0°, 90°), bottom right (210°, 60°). These pictures demonstrate deviation of the instantanious frequency from the original signal, as well as small chirpness of the output signal. 78

3.10 The frequency detuning of a single arm detector normalized over $T\sigma_f^2$. The lines for sources with opposite azimuths and same elevation (e.g. 30° and 210°) match each other because the amplitude of the transfer function has the same dependence on frequency for such locations. 79

3.11 Change of a signal envelope width with frequency. Envelope width is normalized over T^2/σ_t. Lines from opposite azimuths (e.g. 30° and 210°) match each other because they have matching amplitudes of the transfer function for those angles. 82

3.12 The chirp acquired by a signal after the interferometer normalized over $T^2\sigma_f^2$. 83

3.13 The difference between the numerical simulations and analytical calculations for signal broadening (top) and acquired chirp (bottom). The calculations were made for source azimuth 120° and elevation 60°. Discrepancy between the numerical simulation and analytical calculation appear at frequencies when the transfer function approaches zero. 84

3.14 Example signal 1. Original GW signal has constant chirp. Left: GW spectrogram. Right: frequency shift between the original signal and detected signal. 85

3.15 Example signal 2. Original GW has quadratic chirp. Left: GW spectrogram. Right: frequency shift between the original signal and detected signal. 86

4.1 Dependence of one-arm detector transfer function zeros from source location. Top left and bottom right graphs represent dependence of real or imaginary part of the zero with direction, while on the bottom left graph shows movement of the zeros on complex plane when direction to the source changes. 94

4.2 The absolute value of the one arm interferometer transfer function for different frequencies and source angles. White dots correspond to the zeros of the first kind and red dots correspond to the zeros of the second kind. 95

4.3 Examples of zeros for signal frequencies at non-integer FSR for the case (4.23). the left panel shows additional zero which appears for azimuth angle -45° at frequency $4f_{\rm rt}/3$ for arm angle 60°. The left panels shows the zero with the same azimuth that appear for signal frequency $4f_{\rm rt}/(2+\sqrt{2})$ and interferometer with angle between arms 90°. . . 100

4.4 Example of the zero for the case in (4.24) that appears at low frequency approximately $0.752f_{\rm rt}$ for azimuth 45° and elevation 35.26°. The angle between the arms is 120°. The zeros from the case (4.24) are marked with red cross, while zeros from the case (4.23) are marked with red dot. 101

4.5 Michelson interferometer sensitivity for signal frequency at $4f_{\rm rt}$ (left) and $5f_{\rm rt}$ (right). Top plots correspond to the interferometer with 60° angle between arms, bottom plots correspond to the interferometer with 90° angle between arms. Interferometer arms are marked with black lines. The zeros corresponding to the case (4.25) are marked with white dots and zeros corresponding to the case (4.23) are marked with red dots. The red dot corresponds to only one solution when $u = v$. 102

INTRODUCTION

Gravitational waves were predicted by Albert Einstein in 1916 [1]. He linearized the equations for gravitational field and showed that the perturbations of the metric tensor satisfy the wave equation. These perturbations represent weak (linearized) gravitational waves which propagate through space with the speed of light. An important conclusion made by Einstein was that gravitational waves carry energy. Similarly to an accelerated electron that emits electromagnetic radiation, a binary star system will be losing its energy through emission of gravitational waves. At some point, the stars of the binary system will merge producing a strong gravitational-wave signal.

This prediction was put to the test in 1981 when Joseph Taylor and Joel Weisberg reported their observation of a binary pulsar PSR 1913+16 (neutron star system) over the period of six years [2]. Discovered in 1974 by Russel Hulse and Joseph Taylor [3], this binary pulsar sends out periodic electromagnetic waves that allow an observer to measure its period of rotation. According to Taylor, the period of the binary system decreases over time and the amount by which it changes is consistent with the energy loss due to continuous emission of gravitational waves. In 1993, Hulse and Taylor received Nobel Prize "for the discovery of a new type of pulsar, a discovery that has opened up new possibilities for the study of gravitation."

Even though the discovery of Hulse and Taylor served as a proof that gravitational waves exist, direct observation of gravitational waves was yet to come. Moreover, the scientific advances needed to detect gravitational waves will be very useful for astronomy and astrophysics. For example, gravitational waves can be the only way to directly observe black holes which otherwise cannot be observed because they usually do not emit electromagnetic radiation. Another interesting astrophysical source is the explosion of a star known as Core Collapse Supernova (CCSN). It can also emit gravitational waves that will carry information about the explosion process. These signals are likely to have a broadband spectrum with frequencies from tenths to thousandths of hertz.

One of the earliest attempts to search for supernovae was made in 1966 when Joseph Weber built the first bar detector of gravitational waves [4]. Weber's detector was an aluminum cylinder with 1-m diameter and 2-m length having the resonance frequency of 1660 Hz. The cylinder hung on a single wire suspension that was resting on a steel and rubber stack placed in a vacuum chamber. Multiple piezoelectric transducers were connected to the cylinder to detect its vibrations. If a gravitational wave passes through the cylinder it would oscillate with its resonance frequency and the signal from the piezoelectric transducers would produce a trigger indicating possible detection. Weber was operating two such bar detectors, one in Argonne National Laboratory, and the other on the University of Maryland campus. He reported 17 significant two-detector coincidence events within an 81-day observation window [5]. Unfortunately, his observations were met with scepticism because the sensitivity of his bar detectors was not sufficiently high and the false alarm rate was too large to ignore.

Resonant bars were not the only type of gravitational-wave detectors that were considered in the 1960s. Michael Gertsenshteĭn and Vladimir Pustovoĭt proposed an interferometric gravitational wave detector [6] in 1963. Their idea was to use a Michelson interferometer for detection of gravitational waves. In their scheme the laser beams traveling within the two interferometer arms are recombined at the beam splitter. If a gravitational wave passes through the detector it would cause changes in the optical path lengths inside the arms. These changes will result in variations of light intensity after the beam splitter that can be measured with photodetector. It is important to note that the change in the optical path length induced by the gravitational wave is proportional to the arm length. Therefore, the interferometer sensitivity for low-frequency gravitational waves can be improved by increasing the length of the interferometer arms.

Many improvements to the interferometer configuration were made after this scheme was proposed. Fabry-Pérot cavities were added to the interferometer to increase the photon lifetime in the arms thus improving the detector sensitivity. Additional mirrors were placed at the input and output ports of the interferometer to increase the circulating power and tune the detector bandwidth. All these improvements were tested in different laboratories around the world. Decades of research and development led to the construction of the first large scale detector capable of direct observation of gravitational waves. At the present time the largest gravitational-wave detectors in the world belong to the US Laser Interferometry Gravitational wave Observatory (LIGO). This observatory consists of

two detectors with 4-km arm lengths separated by a distance of 3000 km. The groundbreaking ceremony for the first detector took place at the end of 1994 at Hanford, Washington and was followed by another in Livingston, Louisiana next year. Both detectors came online circa 2002 and stayed operational until 2010. No gravitational waves were detected during this period. This outcome motivated substantial improvement of the detector hardware and in 2010 both detectors were shut down for upgrades which lasted five years. The new observatory was called "Advanced LIGO" and began its operation in September 2015. Similar efforts were made in Europe leading to French-Italian interferometer called Virgo. It has arm length of 3 km and optical configuration similar to that of LIGO. Construction of Virgo detector started in 1996 near Pisa, Italy. In its initial stage the Virgo detector started its operation in 2003. It was shut down in 2011 to be upgraded to "Advanced Virgo" which resumed its operation in 2016.

Finally, on September 14, 2015 two LIGO detectors made the first known simultaneous observation of a gravitational-wave signal [7]. It took 20 years of construction, operation and hardware improvement to achieve this remarkable milestone. Long predicted by general relativity, it was the first observation of gravitational waves from a binary black hole merger. In 2017 the LIGO Scientific Collaboration received Nobel Prize "for decisive contribution to the LIGO detector and the observation of gravitational waves."

The signal detected by LIGO interferometers has a frequency chirp from 50 to 270 Hz, as shown in Fig. 1. It agrees well with models of numerical relativity. From the observed signal scientists were able to estimate the distance, the initial and final masses of the system and the spin of the merging objects [8]. Following the initial observation there were many more detections of gravitational waves made by LIGO and Virgo [9–17]. All these events are described in the gravitational-wave transient catalogs of compact binary mergers [18, 19]. Thus far almost all detected signals were produced by merging black holes. The exception is one event that was produced by colliding neutron stars. In this case the detected gravitational wave signal lasted 30 seconds and had frequencies ranging from 50 to 500 Hz. The collision of two neutron stars also produced an electromagnetic signal detected by Interplanetary Gamma-Ray Burst Timing Network (IPN) which includes Fermi and INTEGRAL satellites [20]. Using this information, the Swope optical telescope at Las Campanas laboratory in Chile was able to pinpoint the exact location of the source on the sky, which was later confirmed by other optical, infrared, ultraviolet, and radio telescopes.

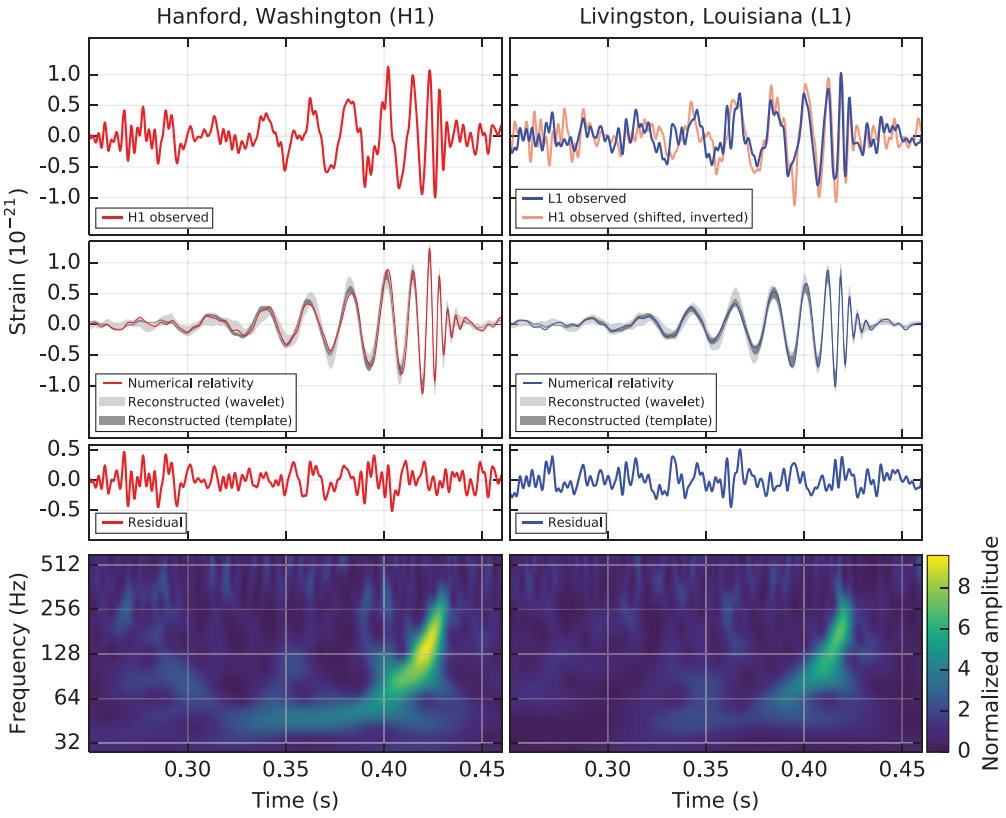

Figure 1: Gravitational-wave signals detected by Washington (left) and Louisiana (right) detectors on September 14, 2015. Top row shows time series of the signals after filtering. Second row shows the numerical relativity simulations. (The residual errors represent the difference between the data and the simulation.) Bottom row shows spectrograms of the signals. (The figure is from [7].)

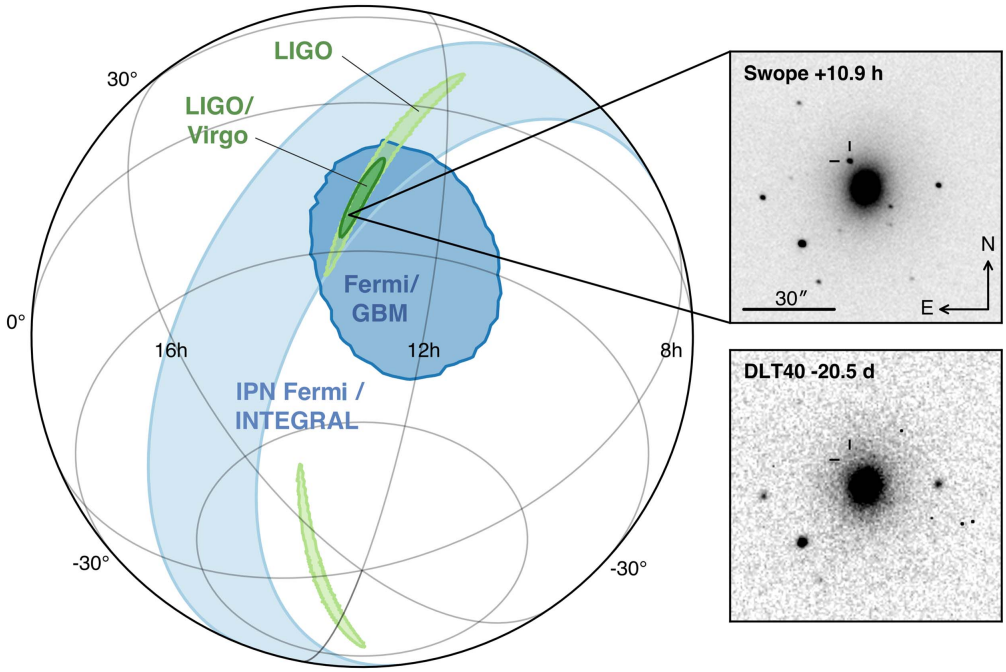

Figure 2: Localization of the source performed by different detectors. The left panel shows localization regions from LIGO interferometers (light-green) an combined LIGO-Virgo network (dark green), Fermi and INTEGRAL satellites of IPN (light blue), and Fermi-GBM (dark blue). The top right panel shows the location of the source taken in the Swope optical telescope at 10.9 hours after the merger. Bottom right shows an image taken 20 days before the event on DLT-40 telescope. Position of the possible source is shown with the reticle mark. (The figure is from [20].)

The detection of gravitational waves played an important role in this discovery. It helped identify the source, localize it in the sky and estimate its parameters. However, there is still some uncertainty about this event. It is not clear what exactly happened with the remnant after the collision. The commonly accepted theory is that the remnant collapsed to a black hole [21] but it is not clear at what time [22]. Moreover, there is a theory that the remnant could form a long-lived neutron star under some conditions [23]. This problem can only be solved with observation of gravitational waves after the merger [24]. However, such gravitational waves would be in 1–4 kHz frequency range. At these frequencies LIGO and Virgo detectors have very limited sensitivity.

Thus, gravitational waves have become an important tool for multi-messenger astronomy. Simultaneous observations of electromagnetic and gravitational waves, accompanied by neutrinos, provide a perfect framework for astrophysical analyses. It also improves the detection capability of each individual approach. The possibility of combining different clues from different detection channels allows probing deeply into the nature of the astrophysical events and the universe at large. Among the most promising sources for multi-messenger astronomy are neutron star binaries and core-collapse supernovae. While we have only one example of a neutron-star merger, the gravitational waves from supernovae are yet be observed.

The growing interest in gravitational-wave astronomy calls for new and more sensitive detectors. These future detectors are often referred to as the third generation (3G) gravitational-wave detectors. Among them is the Cosmic Explorer proposed by LIGO Laboratory [25]. With the arm length of 40 km it is going to be the largest interferometer on Earth, and it is expected to be an order of magnitude more sensitive than the current LIGO detectors. Another 3G detector is called the Einstein Telescope. Proposed by the European collaboration it will have the shape of an equilateral triangle formed by three independent interferometers with arm length of 10 km [26].

Drastic increase of the interferometer arm length requires placing the detector in space. Several proposals have been made for space based detectors such as the Laser Interferometer Space Antenna (LISA) [27–30], TAIJI [31], and TianQin [32]. These interferometers will consist of three spacecraft on the solar or Earth orbit, at the same distance as Earth, arranged in an equilateral triangle configuration. Each satellite will be equipped with two lasers and two test masses together forming three Michelson interferometers. All test masses will be free-falling while moving on their geodesic trajectories effectively eliminating the suspension noise that dominates the low frequency band of

Earth-based detectors. With arm lengths of the order 10^5 – 10^6 kilometers these detectors will be capable to detect gravitational-wave signals with sub-Hz frequencies characteristic for compact binaries in their early stages of evolution, long before the final collision occurs.

With the development of future gravitational-wave interferometers it will also be possible to detect new types of sources such as galactic CCSN [33] and extract additional information about the explosion from the detected gravitational-wave signatures [34]. CCSNe are of major interest for the scientific community because they help to understand better the origin of neutron stars and black holes, the nucleosynthesis of heavy elements, as well as the particle interactions that happen under the conditions of extreme pressure, gravity and density. However, the frequency of gravitational waves from CCSN can be very high so that the corresponding wavelengths can be comparable to the size of future detectors. In this case the long-wavelength approximation that was widely used in the analysis of current gravitational-wave interferometers will no longer be valid. The extension of the signal to higher frequencies results in additional distortions of the waveforms of the gravitational waves. These effects become even more important for space-based interferometers which can detect signals with wavelength much smaller than their arm lengths, thus operating in the regime quite opposite to that of the long-wavelength approximation.

Dissertation overview

In this work we will develop a mathematical approach to analyze, model and classify the signal distortions introduced by gravitational-wave interferometers. We will apply this analysis to study the distortions of gravitational-wave signals produced by CCSN.

In chapter 1 of this dissertation we will provide background information about the nature of gravitational waves. We will describe how gravitational waves interact with photons and how one can use electromagnetic waves to detect perturbations of the space-time metric. Equations for photon propagation in presence of a gravitational wave will be used to model one-arm and Michelson interferometers. These models include analytical equations for the detector transfer function and its impulse response. We will show how these two quantities can be used as two different methods for numerical simulations of gravitational wave detection and discuss their limitations. Next, we will consider various types of CCSN signals using the numerical waveforms published thus far. Dif-

ferent features of a gravitational-waves signature in these signals carry different information about physical processes during supernova explosion. This information will be essential for understanding the consequences of the induced distortions. The main features of the signals include short-duration pulses for bounce signal, quasi-monochromatic SASI modes, and chirped p- and g-modes that are usually present in the numerical waveforms from simulation of CCSN. The information carried by these features makes future detection of CCSN-produced gravitational waves of primary interest for the astrophysical community.

One of the simplest distortions that follow from the phase of the transfer function is group delay of gravitational wave signals. This phenomenon will be reviewed in chapter 2. We show how the group delay varies with frequency and source location in the sky. Note that different detectors will have different delays and this will result in a systematic error in the source localization and waveform reconstruction. We also derive analytical equations describing the group delay and the corresponding chirp delay. To validate our theoretical predictions we will use the interferometer model developed in the previous chapter to perform the numerical simulations. One of the most interesting results of our model is that for some source locations of the source the delay will be negative which means that the signal will be detected before the gravitational wave arrives at the detector site. This can be attributed to the anomalous dispersion of the interferometer transfer function. We will perform additional numerical simulation to consider possible violations of causality. We will also show how the regions on the sky with different group delays change with the frequency of the signal.

In chapter 3, we will conduct further analysis of the interferometer transfer function and derive additional equations that describe the signal distortions. These equations work well for SASI mode of the core collapse, and they will allow predicting the mode frequency detuning as well as the chirp and the signal broadening. Results that describe the mode frequency detuning will be applied to the analysis of distortions of the modes with changing frequency, such as p- and g-modes. In both cases our predictions from analytical equations will be compared with the numerical simulations. To analyze distortions of the bounce signal we will use the interferometer transfer function and the impulse response. We will show the symmetry property of the distortions that follow from the transfer function properties and confirm our predictions with numerical simulations. For each feature we will discuss the effect of the distortions on the information about the supernova explosion.

In chapter 4, we will study the transfer functions of one-arm and Michelson interferometers.

We will analyze the zeros of the transfer functions and show how they change the interferometer behavior for different locations of the source in the sky. We will develop an efficient algorithm for calculating the zeros of the one-arm interferometer with arbitrarily high precision. The algorithm and the information obtained with it will then be used to derive the equations for critical points of a Michelson interferometer. The critical points represent the source location and the signal frequency for which the detector generates largest distortions of the signals.

In the Conclusion chapter we will briefly summarize the results of this work and outline possible applications of this analysis for future detectors.

CHAPTER 1

DETECTION OF GRAVITATIONAL WAVES

1.1 General relativity

In general relativity the separation between two events is described with a quantity called interval which stays the same in any coordinate system. That is to say that interval is invariant under coordinate transformations. For flat (Minkowski) space-time the interval is given by

$$ds^2 = -c^2dt^2 + dx^2 + dy^2 + dz^2, \tag{1.1}$$

where c is the speed of light. General relativity allows more complicated forms of the interval which can be expressed with the help of metric tensor $g_{\mu\nu}$ that describes the local properties of the space-time. Denote the curvilinear coordinates x^{α}[1]. Then

$$ds^2 = g_{\mu\nu}dx^{\mu}dx^{\nu}. \tag{1.2}$$

The interval allows us to describe trajectory of a free-falling particle that moves in space-time defined by $g_{\mu\nu}$. This trajectory is called geodesic and the corresponding equation is geodesic equation. A particle moves according to the principle of least action with action S defined by

$$S = -mc\int ds. \tag{1.3}$$

[1]From now on we will use Greek letters to represent indices of space-time vectors and Latin letters for indices of space vectors.

From the least action principle ($\delta S = 0$) follows the geodesic equation:

$$\frac{d^2x^\mu}{ds^2} + \Gamma^\mu{}_{\alpha\beta}\frac{dx^\alpha}{ds}\frac{dx^\beta}{ds} = 0, \tag{1.4}$$

where $\Gamma^\mu{}_{\alpha\beta}$ are the connection coefficients

$$\Gamma^\mu{}_{\alpha\beta} = \frac{1}{2}g^{\mu\gamma}\left(\partial_\beta g_{\gamma\alpha} + \partial_\alpha g_{\gamma\beta} - \partial_\gamma g_{\alpha\beta}\right), \tag{1.5}$$

where $\partial_\alpha = \frac{\partial}{\partial x^\alpha}$.

The connection coefficients are important if we want to know how a vector field changes with coordinates. If we want to find vector difference at points x^β and $x^\beta + dx^\beta$ we need to perform a parallel transport of the vector from one point to another. However, in curvilinear coordinates a vector can change its component during parallel transport. This change is described with the help of connection coefficients Γ. The total change of a vector field A^μ during an infinitesimal transport by dx^β consists of two parts: one is the change of the vector field components dA^μ, and the other is the change of the vector due to change of the basis:

$$DA^\mu = dA^\mu + \Gamma^\mu{}_{\alpha\beta}A^\alpha dx^\beta. \tag{1.6}$$

This property of the geodesic line helps us understand better (1.4), because they correspond to the first Newton law in free space: in absence of external forces the velocity of an object is constant. Similarly, for space-time we can introduce generalized 4-velocity of an object $u^\mu = dx^\mu/ds$. During motion of the object, its 4-velocity stays constant:

$$Du^\mu = 0. \tag{1.7}$$

The connection coefficients carry important information about structure of space-time. For example, a vector A^α will change if we perform parallel transport along a closed infinitesimal contour. To create this contour we transport vector A^α by du^β, dv^ν, $-du^\beta$ and close it by $-dv^\nu$ translation. The area enclosed by the contour can be written as $\Delta s^{\beta\nu} = du^\beta dv^\nu - du^\nu dv^\beta$. The total change of the

vector is given by

$$\delta A_\mu = \frac{1}{2} R^\alpha{}_{\mu\beta\nu} A_\alpha \Delta s^{\beta\nu}, \tag{1.8}$$

where $R^\alpha{}_{\mu\beta\nu}$ is the Riemann curvature tensor:

$$R^\alpha{}_{\mu\beta\nu} = \partial_\beta \Gamma^\alpha{}_{\mu\nu} - \partial_\nu \Gamma^\alpha{}_{\mu\beta} + \Gamma^\alpha{}_{\gamma\beta}\Gamma^\gamma{}_{\mu\nu} - \Gamma^\alpha{}_{\gamma\nu}\Gamma^\gamma{}_{\mu\beta}. \tag{1.9}$$

Ricci tensor is obtained by contraction of the curvature tensor with respect to two if its indices:

$$R_{\mu\nu} = g^{\alpha\beta} R_{\alpha\mu\beta\nu} = R^\alpha{}_{\mu\alpha\nu}. \tag{1.10}$$

Similarly, we can define the scalar curvature of space-time:

$$R = g^{\mu\nu} R_{\mu\nu}. \tag{1.11}$$

Space-time curvature is a good candidate for the definition of Lagrange density required for gravitational field action because it is a scalar that contains metric tensor and its derivatives:

$$S_g = -\frac{c^3}{16\pi G} \int R \sqrt{|g|} d^4x, \tag{1.12}$$

where G is Newton constant and $g = \det g_{\mu\nu}$. Integration goes over the enclosed 4-volume in curvilinear coordinates. The quantity $\sqrt{|g|}$ can be viewed as the Jacobian of the transformation from the rectilinear to curvilinear coordinates.

Variation of the gravitational field action with respect to $\delta g^{\mu\nu}$ is

$$\delta S_g = -\frac{c^3}{16\pi G} \int \left(R_{\mu\nu} - \frac{1}{2} g_{\mu\nu} R \right) \delta g^{\mu\nu} \sqrt{|g|} d^4x. \tag{1.13}$$

Matter action that creates the gravitational field can be described by

$$S_m = \frac{1}{c} \int \mathscr{L} \sqrt{|g|} d^4x, \tag{1.14}$$

where $\mathscr{L}$ is the Lagrangian density of the system. Variation of the matter action is

$$\delta S_m = \frac{1}{2c}\int T_{\mu\nu}\delta g^{\mu\nu}\sqrt{|g|}d^4x, \tag{1.15}$$

where $T_{\mu\nu}$ is the stress-energy tensor,

$$T_{\mu\nu} = \frac{2}{\sqrt{|g|}}\left[\frac{\partial\sqrt{|g|}\mathscr{L}}{\partial g^{\mu\nu}} - \frac{\partial}{\partial x_\alpha}\left(\frac{\partial\sqrt{|g|}\mathscr{L}}{\partial\partial_\alpha g^{\mu\nu}}\right)\right]. \tag{1.16}$$

The principle of least action implies that the total variation of the action is equal to zero:

$$\delta S_g + \delta S_m = 0. \tag{1.17}$$

This condition gives us the Einstein equations for gravitational field:

$$R_{\mu\nu} - \frac{1}{2}g_{\mu\nu}R = \frac{8\pi G}{c^4}T_{\mu\nu}. \tag{1.18}$$

They describe how the curvature of space-time changes under the influence of matter.

The stress-energy tensor is equal to zero away from material objects:

$$T_{\mu\nu} = 0. \tag{1.19}$$

In this case, the gravitational field equations take the form

$$R_{\mu\nu} = 0. \tag{1.20}$$

This equation describes the spatial configuration and temporal evolution of the gravitational field away from the source. This field can time-dependent and propagate through space in a wave-like manner [1].

1.2 Gravitational waves

Consider small perturbations of the Minkowski metric

$$g_{\mu\nu} = \eta_{\mu\nu} + h_{\mu\nu}, \tag{1.21}$$

where $h_{\mu\nu}$ represents the perturbation. For convenience, we introduce the modified perturbation

$$\bar{h}_{\mu\nu} = h_{\mu\nu} - \frac{1}{2}\eta_{\mu\nu}h^{\alpha}{}_{\alpha}. \tag{1.22}$$

This quantity allows us to define the Ricci tensor (1.10) up to the first order of magnitude in more compact form

$$R_{\mu\nu} = \partial_\alpha \partial^\alpha \bar{h}_{\mu\nu}. \tag{1.23}$$

After substitution of this expression into equation (1.18), we obtain the equation that describes the generation of gravitational waves

$$\frac{1}{2}\left(-\frac{1}{c^2}\frac{\partial^2}{\partial t^2} + \frac{\partial^2}{\partial x^2} + \frac{\partial^2}{\partial y^2} + \frac{\partial^2}{\partial z^2}\right)\bar{h}_{\mu\nu} = \frac{8\pi G}{c^4}T_{\mu\nu}. \tag{1.24}$$

This is the wave equation and its solution can be written with the help of retarded Green function

$$\bar{h}_{\mu\nu}(t,\boldsymbol{x}) = \frac{4G}{c^4}\int \frac{T_{\mu\nu}(t_{ret},\boldsymbol{x}')}{|\boldsymbol{x}-\boldsymbol{x}'|}d^3\boldsymbol{x}', \tag{1.25}$$

where retarded time $t_{ret} = t - |\boldsymbol{x}-\boldsymbol{x}'|/c$ and integration is performed over the region of space that fully encompasses the source. In many cases we are interested in the gravitational wave far away from the source, say at distance r. Keeping only the monopole components we can simplify equation (1.25)

$$\bar{h}_{\mu\nu}(t,r) = \frac{4G}{c^4 r}\int T_{\mu\nu}(t-r/c,\boldsymbol{x}')d^3\boldsymbol{x}'. \tag{1.26}$$

The stress-energy tensor satisfies the law of momentum and energy conservation

$$\partial_\nu T^{\mu\nu} = 0, \tag{1.27}$$

from which it follows that

$$\partial_0^2 \int T^{00} x^i x^j d^3\boldsymbol{x} = 2 \int T^{ij} d^3\boldsymbol{x}. \tag{1.28}$$

The integral in the left part represents the quadrupole moment of the system:

$$I^{ij}(t) = \frac{1}{c^2} \int T^{00} x^i x^j d^3\boldsymbol{x}, \tag{1.29}$$

Therefore, the gravitational wave radiated by the source is given by

$$\bar{h}_{ij} = \frac{2G}{c^4 r} \ddot{I}_{ij}(t - r/c), \tag{1.30}$$

where $\ddot{I}_{ij} = c^2 \partial_0^2 I_{ij}$. Thus, the gravitational wave is generated by a system with time-varying quadrupole moment. This can be a binary star system or asymmetric stellar explosion. In contrast, a rotating spherical object would not produce gravitational waves.

To first order in h, a small gravitational wave is described by the wave equation and, therefore, it propagates through space as a wave. It can be approximated as a plane wave when the distance between the source and the observer becomes very large. Let the wave propagate along the z axis. In this case the gravitational wave equation will be

$$\left(\frac{1}{c^2} \frac{\partial^2}{\partial t^2} - \frac{\partial^2}{\partial z^2} \right) \bar{h}_{\mu\nu} = 0. \tag{1.31}$$

Because of the gauge freedom, we can choose $h_{\mu\nu}$ to be transverse and traceless [35]:

$$\begin{aligned} \partial_\mu h^\mu{}_\nu &= 0, \\ h^\mu{}_\mu &= 0. \end{aligned} \tag{1.32}$$

For a traceless gravitational wave $\bar{h}_{\mu\nu} = h_{\mu\nu}$. Therefore, we can replace $\bar{h}$ with h in equations (1.30) and (1.31).

After gauge fixing, the gravitational wave tensor will have only two independent components

which represent two gravitational-wave polarizations: h_+ and $h_\times$,

$$h_{\mu\nu} = \begin{pmatrix} 0 & 0 & 0 & 0 \\ 0 & h_+ & h_\times & 0 \\ 0 & h_\times & -h_+ & 0 \\ 0 & 0 & 0 & 0 \end{pmatrix}. \tag{1.33}$$

The coordinate system in which the gravitational-wave tensor has form (1.33) will be called the gravitational-wave frame.

We have thus seen that any motion of matter that breaks the spherical symmetry have to produce gravitational waves. This can be, for example, two stars orbiting each other and thus producing periodic gravitational waves. Or, this can be aspherical explosion of a star (supernova) that would produce a short pulse of gravitational waves. In both cases, the gravitational waves will carry important information about the physical processes happening at the source.

1.3 Gravitational waves from Core-Collapse Supernova

During its evolution a star burns its matter in a thermonuclear reaction, producing heavier elements. This process can not last forever and stops with the elements that turned into iron. After that, the future of the star depends on its initial mass. If it is big enough, then the pressure inside the core can overcome the electron-degeneracy pressure and the runaway thermonuclear reaction starts, detonating the star and producing elements that are heavier than iron [36]. For a star with initial mass between 1.4 and 9 solar masses, this event will appear as a supernova, leaving behind a white dwarf in its place. During the explosion of a heavier star with the mass up to 140 solar masses, protons start capturing electrons, producing neutrons, neutrinos, and gamma radiation. This process reduces pressure and increases density of the star core. The core implodes, producing a core-collapse supernova (CCSN) and leaving a neutron star as a remnant. For an even heavier star with the initial mass up to 200 solar masses, radiation pressure during the collapse is so high that it disperses the star without any remnant, producing a pair-instability supernova. Finally, a star with the mass over 200 solar masses will collapse into a black hole, which prevents some of the energy from leaving it and thus weakens the supernova phenomenon.

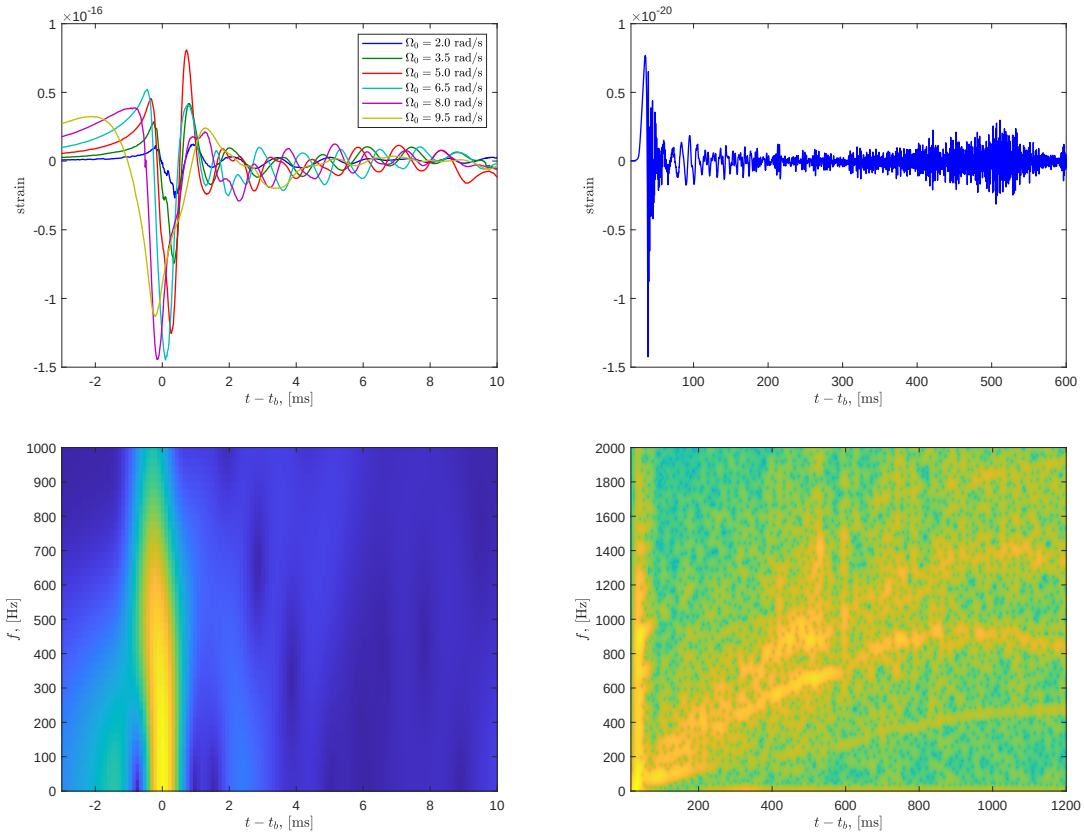

Figure 1.1: Examples of numerical simulations of gravitational waves from rapidly-rotating CCSN. On the left there are time series (top) and spectrogram (bottom) of the signals made by Richers et al [37]. Top left panel shows waveforms from explosion of PNS with different rotational parameters. The spectrogram on bottom left panel corresponds to the case of PNS rotating at 9.5 rad/s. On the right there are time series (top) and spectrogram (bottom) of the waveform from the numerical simulation conducted by Cerda-Duran et al [38]. In this simulation the PNS was initially rotation with angular rate of 2 rad/s. The spectrogram on the bottom right shows the bounce and additional core oscillation modes that appear during the explosion.

In this work we are interested in CCSNe. During the core collapse, there are two regions of the core behaving differently. The inner part of the core shrinks, and the matter from the outer part falls onto the inner part with the supersonic speed. At some moment, the inner part reaches supranuclear densities and stiffens, stopping the collapse and bouncing back. This process is called core bounce. It produces a shock wave that propagates towards the outer part. However, this shock wave loses its energy as it expands. At some moment the shock wave stalls, and without additional energy supplied to the shock wave the star collapses into the black hole. However, there are different mechanisms that provide additional energy to the shock wave, making the star explode. One of the sources of this energy is neutrino convection between the inner and outer parts. Neutrinos, emitted during the electron capture in the inner core, carry energy that is absorbed in the outer core behind the shock wave, preventing the star from collapsing. Another mechanism for the shock wave revival is Standing-Acretion Shock Instability (SASI), which produces non-radial oscillations of the shock wave. These oscillations allow small portions of matter from the outer core to reach the inner core. This process supplies electrons and protons to the region where electron capture happens, enhancing the neutrino convection and contributing to the star explosion. Neutrino convection, SASI, and accretion flow of the matter perturb the star core and produce aspherical oscillations [39]. These oscillations correspond to time-varying quadrupole moments and, according to equation (1.30) should produce gravitational waves. Therefore, the mechanisms that are essential for CCSNe also produce gravitational waves and these two processes are highly connected.

There is no simple physical model of the CCSN due to stochastic nature of the explosion. Instead, a rigorous numerical simulation is necessary to calculate dynamics of the core collapse. This simulation starts from a proto-neutron star (PNS) with its own mass and distribution of different elements produced during the thermonuclear fusion. After that, star evolution is calculated, taking into account general relativity, magnetohydrodynamics, and quantum effects, all at the same time. Therefore, the simulation depends on a large number of parameters. However, one of the most important parameters that affects emission of the gravitational waves is rotation of the original PNS [39].

Rapidly rotating stars are oblate due to centrifugal force. This leads to the slower core bounce along the equatorial plane than the rotational axis. An aspherical motion like this triggers a short (10-20 ms) bounce gravitational wave. Rotational non-axisymmetric instabilities give additional de-

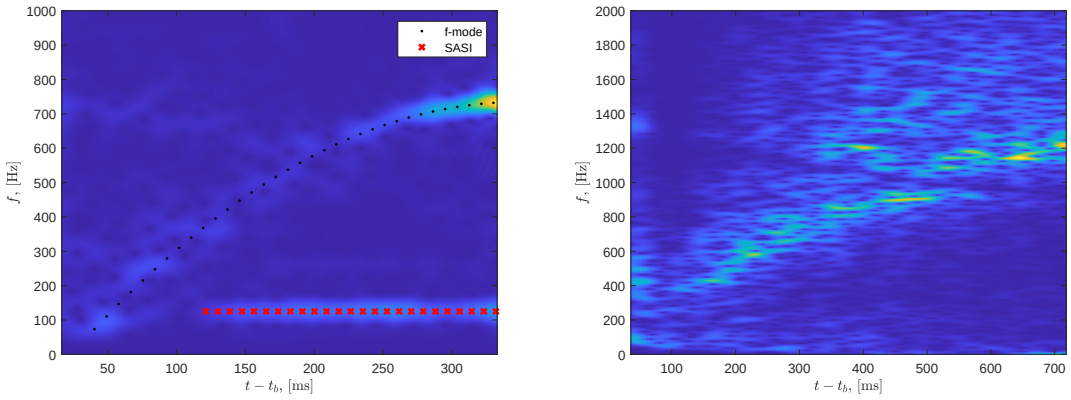

Figure 1.2: Examples of numerical simulation of gravitational waves from slowly rotating CCSN. The left panel shows spectrogram of the waveforms from simulations made by Kuroda et al [40] for $15M_\odot$ progenitor. Additional overlay to this simulation shows fits to the f-mode and SASI. Frequency of the f-mode carries important information about the state of the PNS during the explosion, while development of SASI carries information about the equation of state. The right panel shows a spectrogram of the gravitational-wave signal from the simulation made by Radice et al [41] for a progenitor with mass $M = 9m_\odot$. The line on this spectrogram corresponds to f-mode as well as low lower g-modes, but signs of SASI mode are not present.

formation to the star, which changes its quadrupole moment, resulting in the emission of gravitational waves after the bounce [42]. Simulations of rotating stars show that a gravitational wave produced by the core bounce signal has the highest amplitude. Usually, the amplitude of the gravitational wave grows with the rotational rate. However, at extreme rotations the centrifugal force prevents the matter from the outer core from falling onto the inner core, which reduces the inner core density during the bounce. For example, the amplitude of the bounce signal from the progenitor rotating at angular frequency 9.5 rad/s is less than the amplitude of the signal from the slower rotating progenitor, as shown in Fig. 1.1. In addition to the bounce signal, sometimes SASI and neutrino convection make the core of the PNS oscillate. These oscillations can be seen as ridges in the spectrograms of the gravitational-wave signal. The ridges show change of the oscillation frequency with time. Examples of such modes are shown in the bottom right panel of Fig. 1.1.

Non-rotating or slowly-rotating PNSs remain spherical during the bounce and do not emit gravitational waves at this moment of time. In the later stages of the core collapse neutrino convection and SASI drive the explosion and aspherical oscillations of the core. A perturbation of the shock wave generates vortices on its surface, which pull matter towards the inner core. When the core is hit with this inflow, it starts to oscillate. This oscillation produces acoustic waves that propagate

towards the shock wave and thus distorts it even more. It generates more vortices and amplifies the oscillation. This process generates a gravitational-wave signal with oscillation signatures from the core and SASI. The core mode changes its frequency because the core density increases during the process. At the same time the frequency of SASI mode stays the same. The SASI frequency corresponds to the time necessary for matter to reach the inner core and an acoustic wave to propagate back. Since matter falls into the core with subsonic speed, SASI mode frequency is lower than the frequencies of the core oscillation modes. An example of spectrograms of a gravitational-wave signal that shows f-mode and SASI is given in Fig. 1.2. The impact of SASI varies for different models of explosions, giving them distinctive gravitational-wave features. Some models do not exhibit SASI but still produce explosion, as shown in right panel of Fig. 1.2.

There are some works [37, 43, 44] that concentrate on bounce and early post bounce parts of gravitational-wave signals from rapidly rotating progenitors. The bounce usually produces higher amplitudes of gravitational wave, but they have short duration with less than 5 oscillations in the signal. The signal from core bounce can be used to estimate rotational parameters of the PNS [43, 45]. Additionally, this signal is a good time stamp which marks the start the explosion. The top-left panel in Fig. 1.1 shows a family of such signals.

A second type of feature is SASI [44, 46–51]. This instability is a result of positive feedback between vortices in the shock wave and oscillations of the core. The period of SASI signal corresponds to the time interval for this feedback to occur and remains constant during the explosion. This allows estimation of the ratio between shock and core radius by observation of the SASI mode frequency [52]. Gravitational-wave signal from SASI can be considered as a quasimonochromatic signal. An example of it is shown in right panel of Fig. 1.2.

The third type of features is related to different oscillations of the PNS core. They are often called p- and g- modes, depending on what is the nature of the restoring force, pressure or gravity, that corresponds to the oscillation. The frequencies of the p-modes are higher than g-modes. The fundamental p-mode (p_0 mode) is called f-mode, and it separates p- and g- modes on the spectrogram. The lifespan of these features is usually much longer than the duration of the bounce signal [44]. The frequency of these modes depends on properties of the PNS core and shock wave. By tracking changes of this frequency with time, it is possible to estimate this change. In the work [53] the frequency evolution of different modes is derived from simple spherically symmetric simulation without

additional assumption. In this work, authors try to estimate relationship between the frequency of different modes and properties of the core, such as core mass, radius, shock radius, core density and pressure. This relationship is estimated by introducing polynomial equations that describe dependence of the core modes with the star parameters. The polynomial coefficients of the equations are fitted to agree with results of numerical calculations [54–56]. It is important to note that these authors do not take into account the amplitude of the signal because the main information is carried by the frequency of the signal.

To generalize our analysis, we will use simple analytical waveforms that match different features of the numerical waveforms. To simulate a bounce signal, usually produced by rapidly rotating progenitors, we will use a sine-Gaussian signal with an envelope width of a few oscillations. We will approximate SASI modes as quasi-monochromatic signals with wide envelope and narrow spectral width. The amplitudes of p- and g- modes stochastically change with time. However, the most important information that these modes carry is in the frequency. Therefore, we will construct a simplified model, assuming constant amplitude of the modes and polynomial dependence of frequency with time [53].

1.4 Detection of gravitational waves

As was discussed in the previous chapter, interferometric methods can be used for measuring the variation in the distance between two points by means of a bouncing photon. These methods allow achieving high sensitivity for gravitational waves by increasing the length of the path that a photon travels in one round trip. To show how gravitational waves affect the distance, we will consider a simple example. Assume that we have two points in the XY plane in the gravitational wave frame. We can describe the relative position of these points with the vector

$$\boldsymbol{a} = (a_x, a_y, 0). \tag{1.34}$$

The definition of distance in general relativity depends on the way of measurement. For simplicity, we assume that $dt = 0$ and the distance between two points depends only on their coordinates at a single instance of time. In the absence of a gravitational wave, the distance between these two points

is

$$L_0 = \sqrt{a_x^2 + a_y^2}. \tag{1.35}$$

After the arrival of a gravitational wave, this distance becomes

$$\begin{aligned} L &= \sqrt{g_{ij} a_i a_j} \\ &\approx L_0 \left(1 + \frac{a_x^2 - a_y^2}{2L_0^2} h_+ + \frac{a_x a_y}{L_0^2} h_\times\right). \end{aligned} \tag{1.36}$$

The change in the distance, $\delta L = L - L_0$, will have same order of magnitude as the gravitational wave. The relative change of the distance is

$$\frac{\delta L}{L_0} = \frac{L - L_0}{L_0} = \frac{1}{2}\left(\hat{a}_x^2 - \hat{a}_y^2\right) h_+ + \hat{a}_x \hat{a}_y h_\times, \tag{1.37}$$

where the unit vector

$$\hat{\boldsymbol{a}} = \frac{\boldsymbol{a}}{L_0}. \tag{1.38}$$

This equation describes how space is squeezed or stretched in the direction $\hat{a}$ in the XY plane of the gravitational wave frame. However, the actual measurement of distance will depend on the way of the measurement is done. One of such ways is by bouncing a photon from the mirror and measuring its round-trip time [57].

In general, the impact of a temporal gravitational field on the electromagnetic field can be complex, but it can be simplified if we assume weak gravitational field created by a gravitational wave. We will consider small perturbations created by a gravitational wave in the electromagnetic field that propagate in flat space-time.

In the gravitational wave frame we have the following conditions: $g_{00} = -1$ and $g_{0i} = 0$. This allows us to consider the space properties separately from the time properties. With this notation the interval in the presence of a gravitational wave becomes

$$ds^2 = -c^2 dt^2 + (\delta_{ij} + h_{ij}) dx^i dx^j. \tag{1.39}$$

We will parametrize a geodesic line with parameter ξ: $t = t(\xi)$ and $x^i = x^i(\xi)$. Then the interval

along the geodesic line of a photon is zero. Therefore,

$$c^2\left(\frac{dt}{d\xi}\right)^2 = \left[\delta_{ij} + h_{ij}(x)\right]\frac{dx^i}{d\xi}\frac{dx^j}{d\xi}. \tag{1.40}$$

In the presence of a weak gravitational wave we assume that the trajectory of a photon would not deviate from a straight line. Therefore, we will define small perturbations of the geodesic line $\delta t(\xi)$ and $\delta t(\xi)$

$$t(\xi) = \bar{t}(\xi) + \delta t(\xi), \tag{1.41}$$

$$x^i(\xi) = \bar{x}^i(\xi) + \delta x^i(\xi), \tag{1.42}$$

where $\bar{t}$ and $\bar{x}$ is unperturbed trajectory for flat metric.

The unperturbed trajectory starts at point A with coordinates x_0^i and proceeds in the direction given by unit vector $\hat{a}$. The unperturbed geodesic line will be

$$\bar{x}^i(\xi) = x_0^i + \hat{a}^i\xi, \tag{1.43}$$

and in flat space-time

$$c^2\left(\frac{d\bar{t}}{d\xi}\right)^2 = 1, \tag{1.44}$$

or,

$$c\frac{d\bar{t}}{d\xi} = \pm 1. \tag{1.45}$$

By choosing ξ as increasing with time we obtain the time component dependence of the unperturbed geodesic line:

$$\bar{t}(\xi) = t_0 + \xi/c. \tag{1.46}$$

To derive the trajectory of the photon in the gravitational wave, as well as the time of the propagation, we can divide equation (1.4) over $d\xi$ and solve the corresponding system of differential equations. However, we are interested only in photon propagation time, so we can find it directly

from the first-order perturbed interval. With the perturbation, equation (1.39) becomes

$$c^2\left(\frac{d\bar{t}}{d\xi}+\frac{d\delta t}{d\xi}\right)^2=\left[\delta_{ij}+h_{ij}(x)\right]\left(\frac{d\bar{x}^i}{d\xi}+\frac{d\delta x^i}{d\xi}\right)\left(\frac{d\bar{x}^j}{d\xi}+\frac{d\delta x^j}{d\xi}\right). \tag{1.47}$$

To the first order in perturbation

$$c^2\left(\frac{d\bar{t}}{d\xi}\right)^2+2c^2\frac{d\bar{t}}{d\xi}\frac{d\delta t}{d\xi}=\left[\delta_{ij}+h_{ij}(x)\right]\frac{d\bar{x}^i}{d\xi}\frac{d\bar{x}^j}{d\xi}+2\frac{d\bar{x}^i}{d\xi}\frac{d\delta x^i}{d\xi}. \tag{1.48}$$

Using equation (1.44) we obtain

$$2c\frac{d\delta t}{d\xi}=h_{ij}(x)\hat{a}^i\hat{a}^j+2\hat{a}^i\frac{d\delta x^i}{d\xi}. \tag{1.49}$$

Within the first order perturbation theory we can replace the exact geodesic $x^\mu(\xi)$ with the unperturbed trajectory $\bar{x}^\mu(\xi)$ in the argument of h_{ij}:

$$h_{ij}(x^\mu(\xi))\approx h_{ij}(\bar{x}^\mu(\xi)), \tag{1.50}$$

with the result:

$$2c\frac{d\delta t}{d\xi}=h_{ij}(\bar{x}(\xi))\hat{a}^i\hat{a}^j+2\hat{a}^i\frac{d\delta x^i}{d\xi}. \tag{1.51}$$

Integrating this equation we find:

$$\delta t(\xi)=\frac{\hat{a}^i\hat{a}^j}{2c}\int_0^\xi h_{ij}(\bar{x}(\xi'))d\xi'+\frac{\hat{a}^i}{c}\left[\delta x^i(\xi)-\delta x^i(0)\right]. \tag{1.52}$$

We can now calculate the time of flight for a photon that propagates between two test masses. Let the first test mass be located at position $\boldsymbol{r}_0$ and the second at $\boldsymbol{r}_1$. In the absence of gravitational wave

$$\begin{aligned}\boldsymbol{r}_1&=\boldsymbol{r}_0+\hat{a}L,\\ t_1&=t_0+T,\end{aligned} \tag{1.53}$$

where L is the Euclidean distance between the masses and T is the photon propagation time

$$T=\bar{t}(L)-t_0=L/c \tag{1.54}$$

In the gravitational-wave frame of reference the coordinates $\boldsymbol{r}_0$ and $\boldsymbol{r}_1$ do not change. Therefore, the geodesic line of a photon propagating between these points will be such that at the beginning and end $\delta x(0) = 0$ and $\delta x(L) = 0$. This means that when we consider the total time deviation when a photon travels along the geodesic line, second item in equation (1.52) will be zero. To the first order in h the propagation time is

$$T_{01} = T + \delta T, \tag{1.55}$$

where $\delta T = \delta t(L)$ or

$$\delta T = \frac{\hat{a}^i \hat{a}^j}{2c} \int_0^L h_{ij}(\bar{x}(\xi)) d\xi. \tag{1.56}$$

For a plane gravitational wave function h_{ij} can be written as

$$h_{ij} = h_{ij}\left(t + \frac{\hat{\boldsymbol{n}} \cdot \boldsymbol{r}}{c}\right), \tag{1.57}$$

where $\hat{\boldsymbol{n}}$ is the unit vector pointing to the source of gravitational waves on the sky. Substituting this expression and equation for the unperturbed trajectory (1.43) into equation (1.56) we obtain

$$\delta T = \frac{\hat{a}^i \hat{a}^j}{2c} \int_0^L h_{ij}\left(t_0 + \frac{\hat{\boldsymbol{n}} \cdot \boldsymbol{r}_0}{c} + \frac{(1 + \hat{\boldsymbol{n}} \cdot \hat{\boldsymbol{a}})\xi}{c}\right) d\xi. \tag{1.58}$$

We can introduce $\beta = \xi/c$:

$$\delta T = \frac{\hat{a}^i \hat{a}^j}{2} \int_0^T h_{ij}\left(t_0 + \frac{\hat{\boldsymbol{n}} \cdot \boldsymbol{r}_0}{c} + (1 + \hat{\boldsymbol{n}} \cdot \hat{\boldsymbol{a}})\beta\right) d\beta. \tag{1.59}$$

In this form δT is a function of $\bar{\boldsymbol{x}}_0 = (t_0, \boldsymbol{r}_0)$, which is the beginning of the unperturbed trajectory. Expressing r_0 and t_0 from (1.53) and substituting it into (1.59) we can also write

$$\delta T' = \frac{\hat{a}^i \hat{a}^j}{2} \int_0^T h_{ij}\left(t_1 + \frac{\hat{\boldsymbol{n}} \cdot \boldsymbol{r}_1}{c} - (1 + \hat{\boldsymbol{n}} \cdot \hat{\boldsymbol{a}})\beta\right) d\beta. \tag{1.60}$$

In this form $\delta T'$ is a function of $\bar{\boldsymbol{x}}_1 = (t_1, \boldsymbol{r}_1)$ which is the end of unperturbed trajectory.

To finish the measurement of the time delay perturbation of a photon it is necessary to reflect the photon back to the original point $\boldsymbol{r}_0$. Let us consider a photon that started moving in the direction $\hat{\boldsymbol{a}}$ at the moment $t - 2T$ and finished at the moment t and the same point propagating in the direction

$-\hat{\boldsymbol{a}}$

$$\delta T_{\mathrm{rt}}(t) = \delta T(t - 2T, \boldsymbol{r}_0, \hat{\boldsymbol{a}}) + \delta T'(t, \boldsymbol{r}_0, -\hat{\boldsymbol{a}}). \tag{1.61}$$

Substituting equations (1.59) and (1.60) we obtain

$$\begin{aligned}\delta T_{\mathrm{rt}}(t) = \frac{\hat{a}^i \hat{a}^j}{2} \left[\int_0^T h_{ij}\left(t - 2T + \frac{\hat{\boldsymbol{n}} \cdot \boldsymbol{r}_0}{c} + (1 + \hat{\boldsymbol{n}} \cdot \hat{\boldsymbol{a}})\beta\right) d\beta \right. \\ \left. + \int_0^T h_{ij}\left(t + \frac{\hat{\boldsymbol{n}} \cdot \boldsymbol{r}_0}{c} - (1 - \hat{\boldsymbol{n}} \cdot \hat{\boldsymbol{a}})\beta\right) d\beta. \right]\end{aligned} \tag{1.62}$$

In this equation gravitational wave is integrated within time window with width $2T$. To reflect it in the equations we introduce a new variable $t' = 2T - (1 + \hat{\boldsymbol{n}} \cdot \hat{\boldsymbol{a}})\beta$ for the first integral and $t' = (1 - \hat{\boldsymbol{n}} \cdot \hat{\boldsymbol{a}})\beta$ for the second integral, which gives us

$$\begin{aligned}\delta T_{\mathrm{rt}}(t) = \frac{\hat{a}^i \hat{a}^j}{2} \left[(1 - \hat{\mathbf{n}} \cdot \hat{\mathbf{a}})^{-1} \int_0^{T(1 - \hat{\mathbf{n}} \cdot \hat{\mathbf{a}})} h_{ij}\left(t + \hat{\boldsymbol{n}} \cdot \boldsymbol{r}_0/c - t'\right) dt' + \right. \\ \left. (1 + \hat{\mathbf{n}} \cdot \hat{\mathbf{a}})^{-1} \int_{T(1 - \hat{\mathbf{n}} \cdot \hat{\mathbf{a}})}^{2T} h_{ij}\left(t + \hat{\boldsymbol{n}} \cdot \boldsymbol{r}_0/c - t'\right) dt' \right].\end{aligned} \tag{1.63}$$

First part of this equation corresponds to propagation of the photon from $\mathbf{r}_1$ to $\mathbf{r}_0$ and second corresponds to propagation from $\mathbf{r}_0$ to $\mathbf{r}_1$. This equation describes the simplest interferometer possible, when a gravitational wave is estimated by measurement of the deviation of round-trip time of a photon reflected from a still object. This technique is known as Doppler tracking [58, 59]. However, a more precise measurement can be achieved by observing the change of the photon phase. It can be done by interfering electromagnetic wave with another wave which propagated along different path. Deviation of the electromagnetic wave phase is proportional to the deviation of the time delay:

$$\delta\varphi = \omega \delta T. \tag{1.64}$$

For a plane electromagnetic wave electric field changes as

$$\mathscr{E}(\boldsymbol{r}, t) = \mathscr{E}_0 \exp(i\varphi(\boldsymbol{r}, t)), \tag{1.65}$$

where $\mathscr{E}_0$ is constant amplitude of the electromagnetic field and φ is the phase of the wave

$$\varphi(\mathbf{r},t) = \omega\left(t - \frac{\hat{\boldsymbol{a}}\cdot\boldsymbol{r}}{c}\right) + \delta\varphi(t), \tag{1.66}$$

We will consider the electromagnetic wave at the point $\boldsymbol{r}_0$. For simplicity, we can separate the slowly varying part of E from rapidly changing harmonic part $\exp(i\omega t)$:

$$\mathscr{E}(\boldsymbol{r},t) = E(t)\exp(i\omega t), \tag{1.67}$$

where the slowly varying part is given by

$$E(t) = \mathscr{E}_0\exp(-i\omega\boldsymbol{r}_0\cdot\hat{\boldsymbol{a}}/c + i\delta\varphi(t)). \tag{1.68}$$

We assume that the phase delay due to the gravitational wave is very small: $\delta\varphi \ll 1$, so we can write

$$E(t) = \mathscr{E}_0\exp(-i\omega\boldsymbol{r}_0\cdot\hat{\boldsymbol{a}}/c) + i\psi(t)\mathscr{E}_0\exp(-i\omega\boldsymbol{r}_0\cdot\hat{\boldsymbol{a}}/c). \tag{1.69}$$

The first part in this equation $\bar{E} = \mathscr{E}_0\exp(-i\omega/c)$ is the constant amplitude of the wave in flat space-time and the second part corresponds to electric field perturbation due to the gravitational wave

$$\delta E(t) = i\delta\varphi(t)\bar{E}. \tag{1.70}$$

This equation shows that the electrical field perturbation is proportional to the phase and photon time delay perturbation.

To derive the transfer function of a one-arm interferometer we will perform bilateral Laplace transform

$$\delta\tilde{T}_{\mathrm{rt}}(s) = \int_{-\infty}^{\infty}\delta T_{\mathrm{rt}}(t)e^{-st}dt, \tag{1.71}$$

which gives us

$$\delta\tilde{T}_{\mathrm{rt}}(s) = \frac{\hat{a}^i\hat{a}^j}{2s}e^{\hat{\boldsymbol{n}}\cdot\boldsymbol{r}_0/c}\left[\frac{e^{-sT(1-\mu)} - e^{-2sT}}{1+\mu} + \frac{1-e^{-sT(1-\mu)}}{1-\mu}\right]\tilde{h}_{ij}(s), \tag{1.72}$$

where $\mu = \hat{\boldsymbol{n}}\cdot\hat{\boldsymbol{a}}$ and $\tilde{h}_{ij}(s)$ is Laplace transform of the gravitational wave. Expression that stands in front of the gravitational wave Laplace transform is the transfer function of a one-arm detector [29,

60]

$$\tilde{D}(s) = \frac{e^{\hat{\boldsymbol{n}}\cdot\boldsymbol{r}_0/c}}{2s}\left[\frac{e^{-sT(1-\mu)} - e^{-2sT}}{1+\mu} + \frac{1-e^{-sT(1-\mu)}}{1-\mu}\right]. \tag{1.73}$$

This equation describes the sensitivity of a one-arm detector, or Doppler-tracking detector, to a gravitational wave. It is important to note that this transfer function depends on geometrical position of the source relative to the arm direction, which is expressed in the parameter μ. In the next chapter we will describe the properties of this transfer function in more details.

The remaining part of the equation (1.72) $\hat{a}^i\hat{a}^j$ represents the polarization sensitivity of the detector. In the gravitational-wave frame it is possible to define two vectors $\hat{\boldsymbol{p}}$ and $\hat{\boldsymbol{q}}$ that are perpendicular to each other and also perpendicular to $\hat{\boldsymbol{n}}$. Then, the gravitational-wave tensor can be expressed as

$$h_{ij} = (\hat{p}_i\hat{p}_j - \hat{q}_i\hat{q}_j)h_+ + (\hat{p}_i\hat{q}_j + \hat{q}_i\hat{p}_j)h_\times. \tag{1.74}$$

Therefore, the round-trip time delay perturbation can be expressed in a shorter form

$$\delta\tilde{T}_{\mathrm{rt}}(s) = \tilde{D}(s)\left(F_+\tilde{h}_+(s) + F_\times\tilde{h}_\times(s)\right), \tag{1.75}$$

where

$$F_+ = (\hat{\boldsymbol{a}}\cdot\hat{\boldsymbol{p}})^2 - (\hat{\boldsymbol{a}}\cdot\hat{\boldsymbol{q}})^2, \tag{1.76}$$

$$F_\times = 2(\hat{\boldsymbol{a}}\cdot\hat{\boldsymbol{p}})(\hat{\boldsymbol{a}}\cdot\hat{\boldsymbol{q}}) \tag{1.77}$$

are the polarization sensitivities of the detector. For low frequencies the transfer function $\tilde{D}$ is approximately equal to 1, and coefficients F_+ and $F_\times$ correspond to the polarization sensitivity in the long-wavelength approximation.

For a one-arm detector we can choose vector $\hat{\boldsymbol{q}}$ in such way that it is always perpendicular to the interferometer arm for any direction to the source. In that case $F_\times = 0$ and $F_+ = 1-\mu^2$. However, for a Michelson interferometer this selection will not be possible and it is necessary to take into account both polarization coefficients.

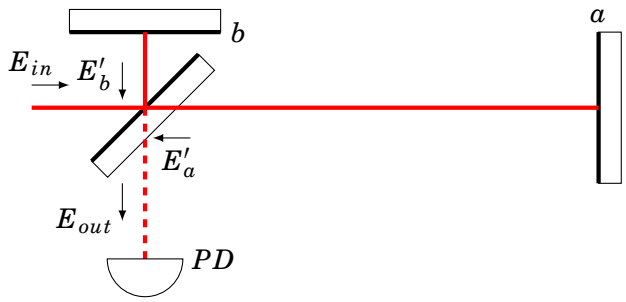

Figure 1.3: Laser beam in a one-arm detector.

1.5 Round-trip interferometer

An example of a one-arm detector is shown in Fig. 1.3. Even though this interferometer requires only one mirror, for precise measurements of the phase perturbation of reflected electromagnetic wave it is necessary to interfere the wave with itself. Therefore, input electric field amplitude E_{in} is split by a beam splitter. The first beam travels towards mirror and reflects from it, arriving back with the amplitude E'_a, which carries additional perturbation due to interaction of the electromagnetic field with the gravitational wave (1.70). Round-trip towards the mirror b is much shorter, and we consider corresponding perturbation of the field E'_b negligible. The output field E_{out} is the result of interference between fields E'_a and E'_b. The signal is measured in the dark port of the interferometer by the photodiode PD.

For simplicity, we assume that the beam splitter and all mirrors are lossless, and the beam splitter splits power equally. Then

$$E'_a(t) = \frac{E_{in}}{\sqrt{2}} \exp(-i\varphi_a)\big(1 + i\delta\varphi_a(t)\big), \tag{1.78}$$

$$E'_b = \frac{E_{in}}{\sqrt{2}} \exp(-i\varphi_b), \tag{1.79}$$

where $\varphi_a = 2\omega L_a/c$ and $\varphi_b = 2\omega L_b/c$ are the phases that the electromagnetic waves acquire during the round-trip propagation, and $\delta\varphi_a(t)$ is the phase perturbation (1.64). The output field in the dark port of the interferometer is equal to the difference between the arm fields $E'_b - E'_a$:

$$E_{out}(t) = \frac{E_{in}}{2}(\exp(-i\varphi_b) - \exp(-i\varphi_a)) - i\frac{E_{in}}{2}\exp(-i\varphi_a)\delta\varphi_a(t). \tag{1.80}$$

The photodiode current I_{PD} is proportional to the power of the electromagnetic wave $I_{PD} = S|E_{out}|^2$. Keeping only first order of the $\delta\varphi_a$, we get

$$I_{PD} = S|E_{in}|^2 \sin\left(\frac{\varphi_b - \varphi_a}{2}\right)\left[\sin\left(\frac{\varphi_b - \varphi_a}{2}\right) + \cos\left(\frac{\varphi_b - \varphi_a}{2}\right)\delta\varphi_a\right]. \tag{1.81}$$

This equation shows that the photodiode signal turns to 0 when the phase change of an electromagnetic wave during propagation is the same for both arms. Therefore, it is necessary to give the phase difference for the arm distances by slightly shifting one of the mirrors. In that case the photodiode signal will have two components which are the DC component introduced due to the arm phase mismatch, and the variable component proportional to the gravitational wave. This method of detection is known as homodyne detection, and is currently used in advanced LIGO [61].

In general, a photodiode's response to the changing electrical field can be more complicated, where it can act as a linear system. However, this dependence is usually taken into account during the interferometer calibration [62]. In this work we assume that the output signal of the interferometer with the subtracted constant part will be proportional to photon time delay perturbation due to a gravitational wave. Thus, we can use the transfer function $\tilde{D}(s,\mu)$ (1.73) and polarization sensitivity coefficients F_+ (1.76) and $F_\times$ (1.77).

We will start exploring the transfer function properties by calculating interferometer impulse response. For simplicity, in this section we assume only h_+ polarization of gravitational wave. Let the gravitational wave be a delta function with arrival time t_0. Then

$$h^{ij}(t) = h_0(\hat{p}^i\hat{p}^j - \hat{q}^i\hat{q}^j)\delta(t - t_0). \tag{1.82}$$

Additionally, we set the center of the coordinate frame at the beam splitter, so $\boldsymbol{r}_0 = \mathbf{0}$. We can substitute (1.82) to the equation 1.63 and obtain

$$\begin{aligned}\delta T_{\mathrm{rt}}(t) = \frac{h_0}{2}\left((\hat{\boldsymbol{p}}\cdot\hat{\boldsymbol{a}})^2 - (\hat{\boldsymbol{q}}\cdot\hat{\boldsymbol{a}})^2\right)\Bigg[&\frac{H(t - t_0 - 2T) - H\left(t - t_0 - T(1-\mu)\right)}{1+\mu} \\ &+ \frac{H\left(t - t_0 - T(1-\mu)\right) - H(t - t_0)}{1-\mu}\Bigg],\end{aligned} \tag{1.83}$$

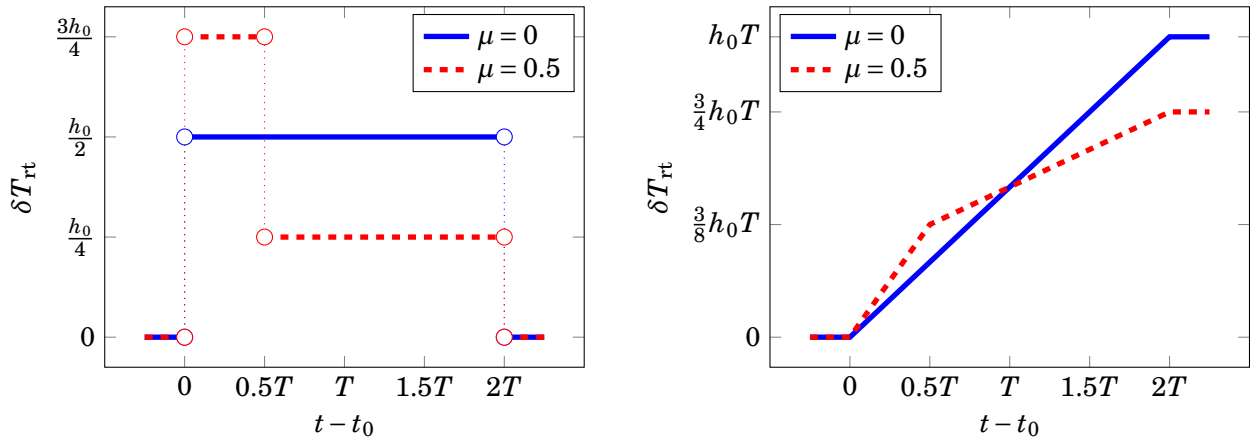

Figure 1.4: Round-trip phase change response to delta (left) and step (right) functions for different source locations. We assume that the arm vector $\hat{\boldsymbol{a}}$ is perpendicular to the polarization vector $\hat{\boldsymbol{q}}$.

where $H(t)$ is Heaviside step-function:

$$H(t) = \begin{cases} 1 & \text{if } t > 0, \\ 0 & \text{if } t < 0. \end{cases} \tag{1.84}$$

Note that the response to the delta function is not physical (Fig. 1.4 left). First, the units of the delta function is inverse seconds, which means the units of the phase response becomes radians per second. Second, the delta-function response has a couple of holes in the graph that correspond to photons bouncing from mirrors at the time of arrival of a gravitational wave on these points. Even though such a response is not physical, its Fourier transform corresponds to the frequency response of the system. This response corresponds to the kernel of the linear system. It can be used to calculate the response to any arbitrary functions by convolution of this function with the kernel.

A more physically meaningful response can be calculated for the step function (Fig. 1.4 right), which is an anti-derivative to the delta function.

The function in the square brackets from equation (1.83) together with the constant 1/2 make the impulse response function $D(t,\mu)$

$$D(t,\mu) = \frac{1}{2}\left[\frac{H(t-2T) - H\big(t - T(1-\mu)\big)}{1+\mu} + \frac{H\big(t - T(1-\mu)\big) - H(t)}{1-\mu}\right]. \tag{1.85}$$

Finally, the perturbation of the photon round-trip time for a gravitational wave can be expressed as

$$\delta T_{\mathrm{rt}}(t,\hat{\boldsymbol{n}}) = \hat{a}^i \hat{a}^j \int_{-\infty}^{\infty} D(t-t', \hat{\boldsymbol{a}}\cdot\hat{\boldsymbol{n}}) h_{ij}(t') dt'. \tag{1.86}$$

The function D has the following symmetry property:

$$D(2T-t,\mu) = D(t,-\mu). \tag{1.87}$$

This symmetry will also appear in the output signal. If the input gravitational wave is even relative to the moment of time t_0,

$$h_{ij}(2t_0-t) = \pm h_{ij}(t), \tag{1.88}$$

then two signals from identical sources, but coming from opposite directions will be even relative to the moment of time t_0+T:

$$\delta T_{\mathrm{rt}}(2(t_0+T)-t,\hat{\boldsymbol{n}}) = \delta T_{\mathrm{rt}}(t,-\hat{\boldsymbol{n}}). \tag{1.89}$$

This symmetry property predicts an overall shift of the detected signal by T with additional deviations, that have different sign for opposite directions to the source.

The impulse response D changes at the moments of time $T(1-\mu)$ mark. To explain the origin of this moment, we consider an example in Fig. 1.5. First, the gravitational wave reaches the end mirror, as shown in the left panel. The intersection point between the arm and the gravitational-wavefront propagates faster than the photons. Therefore, the wavefront constantly reaches new photons that propagate in the same direction (co-moving photons), as shown in the middle panel with the blue arrow. The beginning of the arrow marks the position of the first photon that the wavefront encountered, and the end of the arrow corresponds to the new photon. At the same time the wave-front intersects with the photons propagating in the opposite direction (contra-moving photons). When the gravitational wave reaches the beam splitter (right panel), the first co-moving photon that interacted with the wave front traveled distance $L\hat{\boldsymbol{a}}\cdot\hat{\boldsymbol{n}} = L\mu$ from the end mirror, and this photon is the last one in the chain of the co-moving photons. The total length of the co-moving photon chain is $L(1-\mu)$, and the rest of the arm is filled with contra-moving photons. For the next time duration $T(1-\mu)$, the co-moving photons will create the signal. After that, the signal will be created by the contra-moving

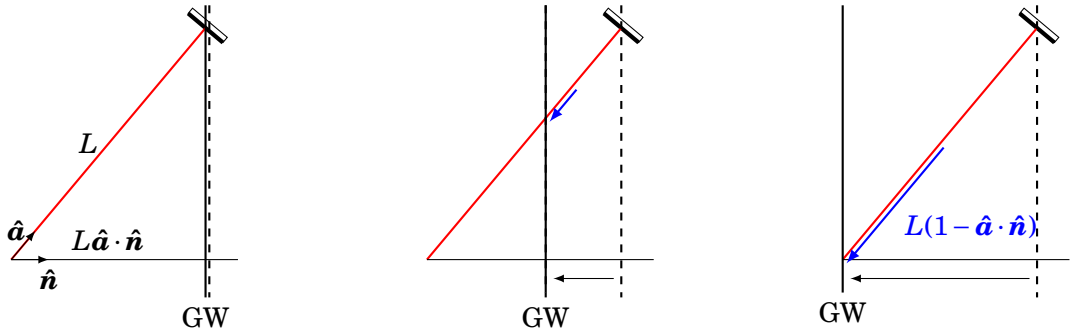

Figure 1.5: Propagation of a gravitational-wave front through an interferometer arm with length L. Blue line marks photons that are moving in the same direction with the gravitational-wave front when it reaches them.

photons during the next $T(1-\mu)$, unless the last photon that interacted with the gravitational wave pulse will reach the beam-splitter. A similar process happens when the gravitational wave hits the beam splitter first. In this case, however, the first signal is created by the contra-moving photons, and the co-moving photons arrive the last.

Bilateral Laplace transform of the impulse response $D(t)$ gives us the interferometer transfer function (1.73). An interferometer response to a unique gravitational-wave frequency Ω will be equal to the transfer function with $s = i\Omega$ [60]:

$$\tilde{D}(i\Omega,\mu) = T\frac{e^{-i\Omega T}}{2}\left[e^{-i\Omega T(1-\mu)/2}\,\mathrm{sinc}(\Omega T(1+\mu)/2) + e^{i\Omega T(1+\mu)/2}\,\mathrm{sinc}(\Omega T(1-\mu)/2)\right], \tag{1.90}$$

where function $\mathrm{sinc}(x) = \sin(x)/x$. Two components of this equation represent the interference between the co-moving and contra-moving photons. Cnsider a train of photons propagating within this interferometer. Its first part will arrive within time $T(1-\mu)$, when the phase of the signal changes by

$$2\varphi_i = \Omega T(1-\mu), \tag{1.91}$$

and for the rest of the photons the phase changes by

$$2\varphi_r = \Omega T(1+\mu). \tag{1.92}$$

We will use these phases to simplify equation (1.90).

Additionally, we want to normalize equation (1.90) to generalize it for any arm length. If we

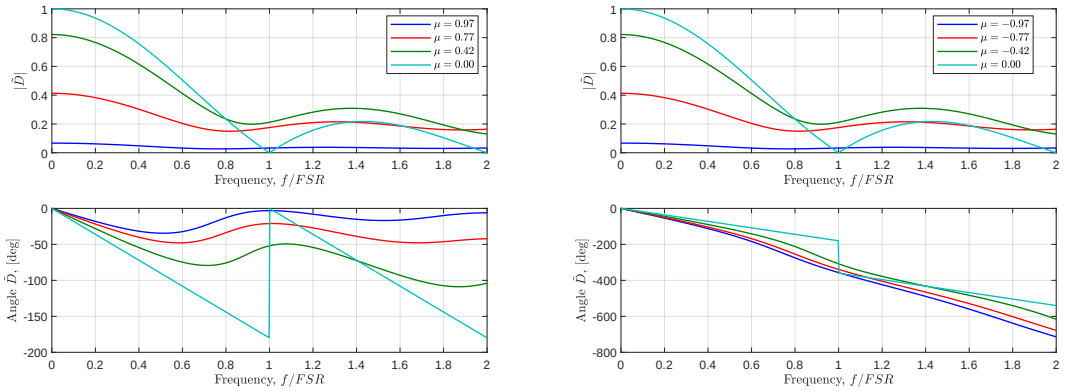

Figure 1.6: Round-trip transfer function response for different angles between the arm and direction to the GW source. For acute angles phase response of the transfer function oscillates between 0° and −90°, while for obtuse angles phase response constantly decreasing.

normalize the photons round-trip time perturbation (1.63) over the one way arm time T, then the transfer function (1.90) will be dimensionless, with the value of the transfer function for zero frequency equal to 1. Additionally, we can normalize the frequency too. The length of the arm impulse response is $2T$. Therefore, its *free spectral range* (FSR) is $f_{\mathrm{rt}} = 1/(2T)$. From now on, we will assume the normalized impulse response $D(t)$ and the transfer function $\tilde{D}(\Omega)$:

$$\tilde{D}(i\Omega T, \mu) = \frac{e^{-i\Omega T}}{2}\left[e^{-i\varphi_i}\,\mathrm{sinc}(\varphi_r) + e^{i\varphi_r}\,\mathrm{sinc}(\varphi_i)\right]. \tag{1.93}$$

The magnitude of the normalized transfer function and its phase response are shown in Fig. 1.6.

The symmetry property of the impulse response (1.87) is also manifested in the transfer function. By taking the Fourier transform of this equation, we find that the amplitude of the transfer function is even relative to the μ:

$$|\tilde{D}(i\Omega, \mu)| = |\tilde{D}(i\Omega, -mu)|. \tag{1.94}$$

At the same time the phase of the transfer function is odd relative to the point $-\Omega T$:

$$\arg(\tilde{D}(i\Omega, \mu)) = -2\Omega T - \arg(\tilde{D}(i\Omega, -\mu)). \tag{1.95}$$

Another property of the transfer function is related to its imaginary part. After some algebraic

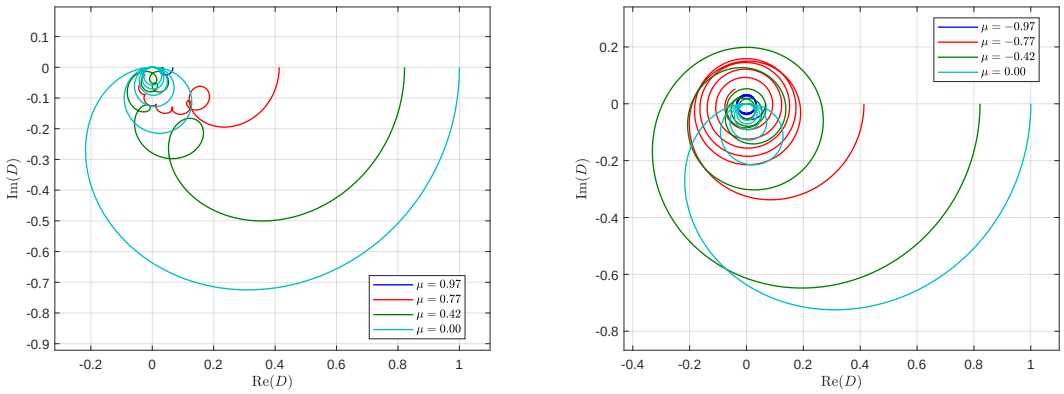

Figure 1.7: Round-trip transfer function response on the complex plane.

transformations we obtain

$$\mathrm{Im}\{\tilde{D}(i\Omega T)\} = -\frac{1}{2\Omega T}\frac{1+\mu-2\mu\cos(2\varphi_i)-(1-\mu)\cos(2\Omega T)}{1-\mu^2}. \tag{1.96}$$

The numerator of this equation is bound from below:

$$1+\mu-2\mu\cos(2\varphi_i)-(1-\mu)\cos(2\Omega T) \geq 2(\mu-|\mu|). \tag{1.97}$$

Therefore, for positive μ the imaginary part of the transfer function is not greater than zero

$$\mathrm{Im}\{\tilde{D}(i\Omega T)\} \leq 0. \tag{1.98}$$

For positive values of μ, the transfer function lies below the real axis, and the phase of the transfer function is within the interval $[-180°, 0]$. For negative values of μ, the transfer function encircles the point $(0,0)$ slowly approaching it. In this case, the phase of the transfer function monotonically decreases with frequency. The behavior of the transfer function on the complex plane is shown in Fig. 1.7.

1.6 Michelson interferometer

The layout of the Michelson interferometer is similar to the layout of the one-arm detector. However, now arm b has the same length as arm a. A schematic layout of the Michelson interferometer is

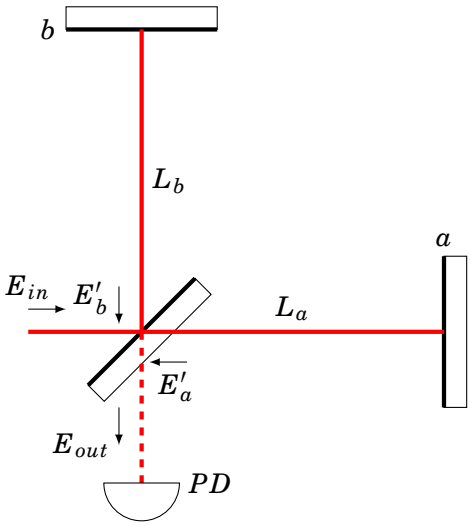

Figure 1.8: Laser beam in a Michelson interferometer.

shown in Fig. 1.8. In this configuration the electromagnetic field is perturbed in both arms, and these perturbations interfere at the beam splitter, producing the signal in the output port of the interferometer.

$$E_{out}(t) = \frac{1}{\sqrt{2}}(E'_b(t) - E'_a(t)), \tag{1.99}$$

where the fields in each arm are

$$E'_a(t) = \frac{E_{in}}{\sqrt{2}} \exp(-i\varphi_a)\left(1 + i\delta\varphi_a(t)\right), \tag{1.100}$$

$$E'_b(t) = \frac{E_{in}}{\sqrt{2}} \exp(-i\varphi_b)\left(1 + i\delta\varphi_b(t)\right). \tag{1.101}$$

The phase perturbations $\delta\varphi_a(t)$ and $\delta\varphi_b(t)$ are described by equation (1.64), with unitary arm vectors $\hat{\boldsymbol{a}}$ and $\hat{\boldsymbol{b}}$. Phases $\varphi_a = 2\omega L_a/c$ and $\varphi_b = 2\omega L_b/c$ are the unperturbed phases of round-trip photons in both arms. The interferometer output field is

$$\begin{aligned} E_{out}(t) = -i\frac{E_{in}}{2} \exp\left(i\frac{\varphi_b + \varphi_a}{2}\right)\Bigg[2\sin\left(\frac{\varphi_b - \varphi_a}{2}\right) - \cos\left(\frac{\varphi_b - \varphi_a}{2}\right)(\delta\varphi_b(t) - \delta\varphi_a(t)) \\ + i\sin\left(\frac{\varphi_b - \varphi_a}{2}\right)(\delta\varphi_b(t) + \delta\varphi_a(t))\Bigg]. \end{aligned} \tag{1.102}$$

The signal from the photodetector, up to the first order of $\delta\varphi$, will be

$$I_{PD} = S|E_{in}|^2 \sin\left(\frac{\varphi_b - \varphi_a}{2}\right)\left[\sin\left(\frac{\varphi_b - \varphi_a}{2}\right) - \cos\left(\frac{\varphi_b - \varphi_a}{2}\right)(\delta\varphi_b(t) - \delta\varphi_a(t)).\right]. \tag{1.103}$$

This result is similar to the equation (1.81) for the one-arm detector. However, now the signal is proportional to the difference in the perturbations of fields in two arms. Usually the interferometer arms are equal to each other, with small detuning on the order of the laser wavelength to produce the homodyne output. This allows us to normalize the impulse response and the transfer function of both arms over one-way time T and use the normalized transfer functions from the previous section. After subtraction of the DC component, the photodiode signal becomes

$$\delta I_{PD} = G\left(\delta T_{\mathrm{rt}}(t,\hat{\boldsymbol{b}}) - \delta T_{\mathrm{rt}}(t,\hat{\boldsymbol{a}})\right), \tag{1.104}$$

where the gain is given by

$$G = \frac{S|E_{in}|^2\omega T}{2}\sin(\varphi_b - \varphi_a). \tag{1.105}$$

The impulse response of the photodetector in Michelson interferometer can be derived from equation (1.104) by substituting the corresponding responses for round-trip time (1.83). However, now we need to consider both + and × polarizations of the gravitational wave. For Michelson interferometer, we cannot rotate gravitational wave coordinate frame in such a way that vector $\hat{\boldsymbol{q}}$ is perpendicular to both arms for an arbitrary source. Therefore, we need to provide impulse response for + and × polarized impulses:

$$h_+^{ij} = h_0(\hat{p}^i\hat{p}^j - \hat{q}^i\hat{q}^j)\delta(t-t_0), \tag{1.106}$$

$$h_\times^{ij} = h_0(\hat{p}^i\hat{q}^j + \hat{q}^i\hat{p}^j)\delta(t-t_0). \tag{1.107}$$

The impulse response will be

$$\delta I_{PD+} = h_0 G(F_+(\hat{\boldsymbol{b}},\hat{\boldsymbol{n}})D(t,\hat{\boldsymbol{b}}\cdot\hat{\boldsymbol{n}}) - F_+(\hat{\boldsymbol{a}},\hat{\boldsymbol{n}})D(t,\hat{\boldsymbol{a}}\cdot\hat{\boldsymbol{n}})), \tag{1.108}$$

$$\delta I_{PD\times} = h_0 G(F_\times(\hat{\boldsymbol{b}},\hat{\boldsymbol{n}})D(t,\hat{\boldsymbol{b}}\cdot\hat{\boldsymbol{n}}) - F_\times(\hat{\boldsymbol{a}},\hat{\boldsymbol{n}})D(t,\hat{\boldsymbol{a}}\cdot\hat{\boldsymbol{n}})), \tag{1.109}$$

where polarization sensitivity coefficients F_+ and $F_\times$ are defined in (1.76) and (1.77), and $D(t,\mu)$ is the one-arm detector impulse response. In addition to $\mu = \hat{\boldsymbol{a}}\cdot\hat{\boldsymbol{n}}$, we introduce another coefficient

$\nu = \hat{\boldsymbol{b}} \cdot \hat{\boldsymbol{n}}$. Using these notations, we can introduce two Michelson interferometer impulse responses:

$$M_+(t,\mu,\nu) = \frac{1}{2}\left(F_+(\hat{\boldsymbol{b}},\hat{\boldsymbol{n}})D(t,\nu) - F_+(\hat{\boldsymbol{a}},\hat{\boldsymbol{n}})D(t,\mu)\right), \tag{1.110}$$

$$M_\times(t,\mu,\nu) = \frac{1}{2}\left(F_\times(\hat{\boldsymbol{b}},\hat{\boldsymbol{n}})D(t,\nu) - F_\times(\hat{\boldsymbol{a}},\hat{\boldsymbol{n}})D(t,\mu)\right). \tag{1.111}$$

The Michelson transfer functions have the symmetry property similar to that of the one-arm detector (1.87). The arm sensitivities have symmetry for source direction flip:

$$F_+(\hat{\boldsymbol{a}},\hat{\boldsymbol{n}}) = F_+(\hat{\boldsymbol{a}},-\hat{\boldsymbol{n}}), \tag{1.112}$$

$$F_\times(\hat{\boldsymbol{a}},\hat{\boldsymbol{n}}) = -F_\times(\hat{\boldsymbol{a}},-\hat{\boldsymbol{n}}). \tag{1.113}$$

Therefore, if the source direction changes sign, then the Michelson impulse response is reflected relative to time T:

$$M_+(2T-t,\mu,\nu) = M_+(t,-\mu,-\nu), \tag{1.114}$$

$$M_\times(2T-t,\mu,\nu) = -M_\times(t,-\mu,-\nu). \tag{1.115}$$

To see how the response changes with the source location, we need to introduce a suitable coordinate system. A Michelson interferometer has one additional degree of freedom, which is the angle between interferometer arms α. In this analysis we assume that this angle can be arbitrary taking values from 0° to 180° but excluding the boundaries. Based on two arm vectors $\hat{\boldsymbol{a}}$ and $\hat{\boldsymbol{b}}$, we can introduce the coordinate system by placing the arms in the equatorial plane and setting the angle between $\hat{\boldsymbol{a}}$ and $\hat{\boldsymbol{x}}$ equal to the angle between $\hat{\boldsymbol{b}}$ and $\hat{\boldsymbol{y}}$, as shown in Fig. 1.9. In this coordinate system every unit vector can be defined in terms of the source azimuth ϕ, elevation θ, and gravitational wave coordinate frame angle ψ.

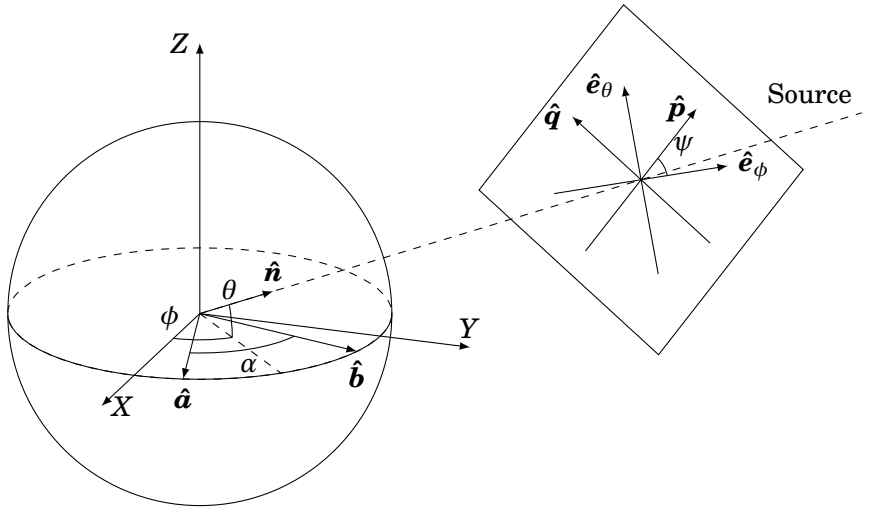

Figure 1.9: Coordinate system introduced for a Michelson interferometer with arm directions $\hat{\boldsymbol{a}}$ and $\hat{\boldsymbol{b}}$. Orthogonal axes $\hat{\boldsymbol{x}}$ and $\hat{\boldsymbol{y}}$ share the same bisector with the vectors $\hat{\boldsymbol{a}}$ and $\hat{\boldsymbol{b}}$. Azimuth angle ϕ and elevation angle θ set direction towards the source $\hat{\boldsymbol{n}}$. Vectors $\hat{\boldsymbol{p}}$ and $\hat{\boldsymbol{q}}$ are two polarization vectors of an incoming gravitational wave.

$$\hat{\boldsymbol{a}} = \cos(\pi/4 - \alpha/2)\hat{\boldsymbol{x}} + \sin(\pi/4 - \alpha/2)\hat{\boldsymbol{y}}, \tag{1.116}$$

$$\hat{\boldsymbol{b}} = \sin(\pi/4 - \alpha/2)\hat{\boldsymbol{x}} + \cos(\pi/4 - \alpha/2)\hat{\boldsymbol{y}}, \tag{1.117}$$

$$\hat{\boldsymbol{n}} = \cos(\theta)\cos(\phi)\hat{\boldsymbol{x}} + \cos(\theta)\sin(\phi)\hat{\boldsymbol{y}} + \sin(\theta)\hat{\boldsymbol{z}}, \tag{1.118}$$

$$\hat{\boldsymbol{e}}_\phi = -\sin(\phi)\hat{\boldsymbol{x}} + \cos(\phi)\hat{\boldsymbol{y}}, \tag{1.119}$$

$$\hat{\boldsymbol{e}}_\theta = -\cos(\phi)\sin(\theta)\hat{\boldsymbol{x}} - \sin(\phi)\sin(\theta)\hat{\boldsymbol{y}} + \cos(\theta)\hat{\boldsymbol{z}}, \tag{1.120}$$

$$\hat{\boldsymbol{p}} = \cos(\psi)\hat{\boldsymbol{e}}_\phi + \sin(\psi)\hat{\boldsymbol{e}}_\theta, \tag{1.121}$$

$$\hat{\boldsymbol{q}} = -\sin(\psi)\hat{\boldsymbol{e}}_\phi + \cos(\psi)\hat{\boldsymbol{e}}_\theta. \tag{1.122}$$

The response to the δ-function will look like the sum of two responses, similar to the response shown in Fig. 1.4. The result will consist of three steps within the round-trip time $2T$. The amplitudes of these steps depend on the location of the gravitational wave source. The expressions for the round-trip response can be quite long, so we just plot some characteristic examples in Fig. 1.10 for + polarization and in Fig. 1.11 for × polarization. It is important to note that the coordinate system defined above is suitable for a single detector. In this case, it is convenient to set $\psi = 0$. However, for a network of detectors we will need a new coordinate system, with different detectors having different

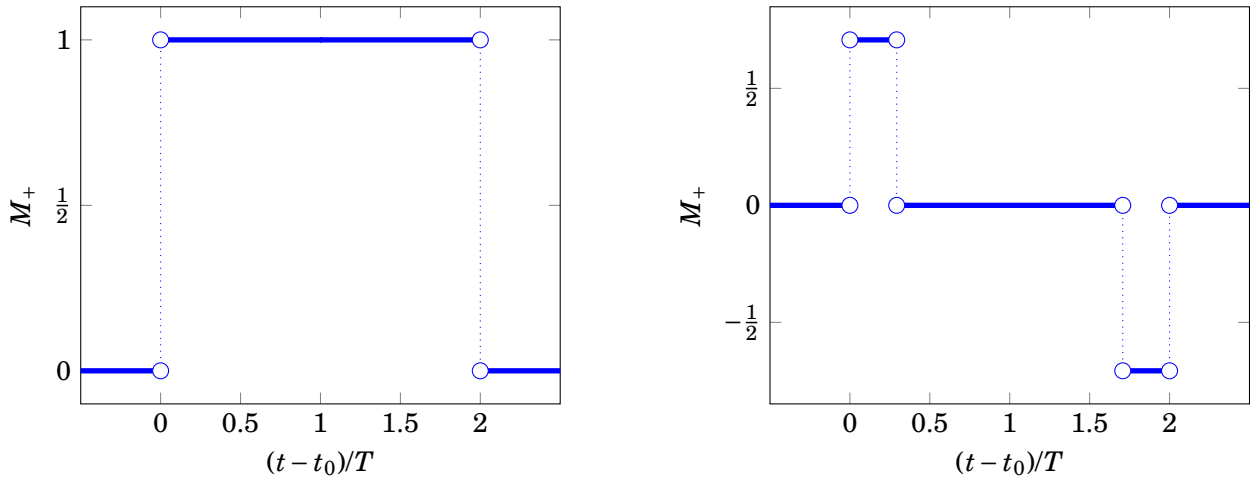

Figure 1.10: Michelson interferometer response to + polarization δ function. Left: source with optimal orientation $\phi = 0°$, $\theta = 90°$. Right: source with orientation $\phi = 135°$, $\theta = 0°$.

locations $\boldsymbol{r}_0$ and different arm directions. In this case angle ψ will be unique for each detector, and the corresponding vectors will be rotated according to the new detector position.

When the direction to the gravitational wave source is perpendicular to the plane formed by the interferometer arms ($\theta = \pm 90°$), the response to the δ-function looks like a square wave shown in the left panel of Fig. 1.10. In this regime the output of the interferometer is proportional to the gravitational wave signal averaged over time interval $2T$. Therefore, the response becomes zero only for harmonic signals with period $2T/i$, $i \epsilon \mathbb{N}$.

When the source of the gravitational wave has azimuth 45° or 225° (gravitational wave passes right in the middle between two arms), the response to the + polarization is zero. For these source directions, the photon round-trip time perturbations in both arms are the same, so they cancel in the output signal.

Another special case is when azimuth to the source is 135° or 315°, or $\mu = -\nu$. In this case the round-trip response of the arm a transforms to the round-trip response of the arm b relative to the time moment T. The arm sensitivities are the same for + polarization $F_+(\hat{\boldsymbol{a}}) = F_+(\hat{\boldsymbol{b}})$. Subtraction of these two responses results to the response with first and last step having the same amplitudes and opposite signs, while the middle step is zero as shown in the right panel of Fig. 1.10. This response corresponds to the derivative of the input gravitational wave signal. The distance between the points that are taken for the derivative calculation, as well as the averaging intervals for these points depend on the elevation angle of the source and the angle between arms. The width of the

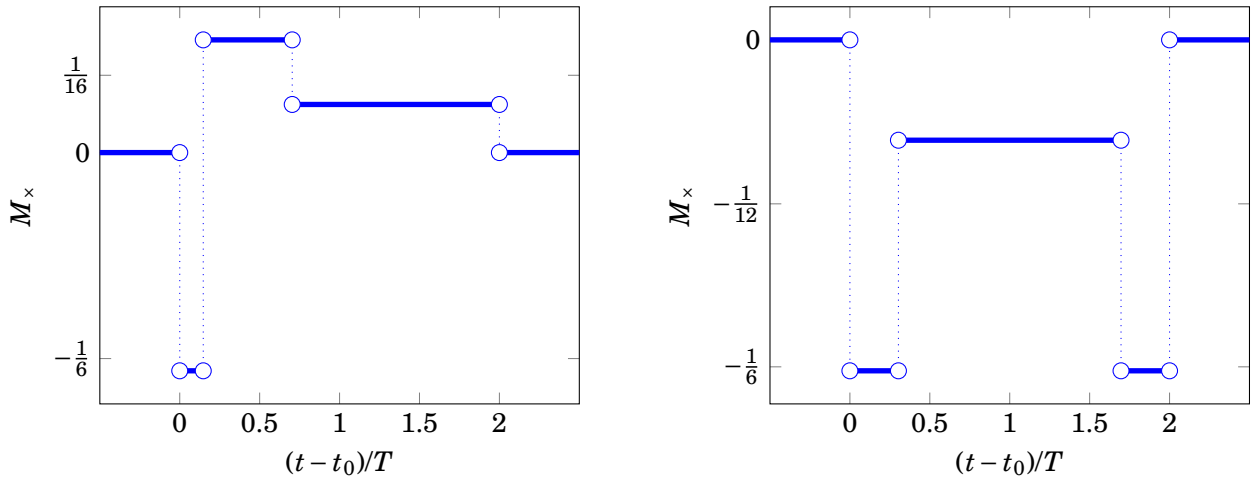

Figure 1.11: Michelson round-trip response to × polarization δ function. Left: source located at $\phi = 5°$, $\theta = 30°$, angle between interferometer arms $\alpha = 60°$. Right: source located at $\phi = 135°$, $\theta = 10°$, angle between interferometer arms $\alpha = 90°$.

first and the last steps are $\cos(\theta)\sin(\alpha/2)$.

The response to × polarization does not have this differential feature. The reason for that is the change of the sign for arm sensitivity: $F_\times(\hat{\boldsymbol{a}}) = -F_\times(\hat{\boldsymbol{b}})$. As a result, for × polarization the impulse response at angles 135° and 315° represents three steps, with the first and last having the same amplitude, as shown in the right panel of Fig. 1.11.

By taking Laplace transform we can derive the Michelson interferometer transfer function:

$$\begin{aligned}\tilde{M}_+(s,\mu,\nu) &= \frac{1}{2}\left(F_+(\hat{\boldsymbol{b}},\hat{\boldsymbol{n}})\tilde{D}(s,\nu) - F_+(\hat{\boldsymbol{a}},\hat{\boldsymbol{n}})\tilde{D}(s,\mu)\right)\\ \tilde{M}_\times(s,\mu,\nu) &= \frac{1}{2}\left(F_\times(\hat{\boldsymbol{b}},\hat{\boldsymbol{n}})\tilde{D}(s,\nu) - F_\times(\hat{\boldsymbol{a}},\hat{\boldsymbol{n}})\tilde{D}(s,\mu)\right).\end{aligned} \tag{1.123}$$

The response of the Michelson interferometer to a particular gravitational-wave frequency follows from the normalized transfer functions:

$$\tilde{M}_+(i\Omega T,\mu,\nu) = \frac{1}{2}\left(F_+(\hat{\boldsymbol{b}},\hat{\boldsymbol{n}})\tilde{D}(i\Omega T,\nu) - F_+(\hat{\boldsymbol{a}},\hat{\boldsymbol{n}})\tilde{D}(i\Omega T,\mu)\right) \tag{1.124}$$

$$\tilde{M}_\times(i\Omega T,\mu,\nu) = \frac{1}{2}\left(F_\times(\hat{\boldsymbol{b}},\hat{\boldsymbol{n}})\tilde{D}(i\Omega T,\nu) - F_\times(\hat{\boldsymbol{a}},\hat{\boldsymbol{n}})\tilde{D}(i\Omega T,\mu)\right). \tag{1.125}$$

1.7 Detection prospects of CCSNe gravitational-wave signals

Core-collapse supernovae are of great interest for the astrophysical community. These explosions give insight into the origin of neutron stars and black holes, processes of nucleosynthesis of heavy elements, as well as particle interactions under extreme pressure, gravity, and density. Observation of neutrino and gravitational waves from the explosion can provide early signs that a supernova occurred somewhere in the universe. Moreover, these messengers carry signatures of processes happening in the core of a proto-neutron star, that are often hidden from electromagnetic observation by the outer shell of the star. Thus far, there has been no direct observation of gravitational waves from CCSN. Research points towards more sensitive future detectors capable of detecting galactic CCSNe [34, 56]. This will open a new window for observations of CCSNe which can improve our understanding of the processes happening in a PNS during the core collapse and explosion. However, even with the future interferometers, detection of a gravitational wave from core collapse would not be easy. The main difficulty in detection of a CCSN gravitational wave is the stochastic nature of the core collapse and the existence of many factors that could drastically change the waveform morphology. Currently, numerous numerical simulations of CCSN have been conducted [37, 38, 40, 41, 43, 44, 46, 48–50, 54, 63–68], and many of them show similar features attributed to different types of explosions [39].

A modern approach to detect CCSN gravitational waves is by using BayesWave [69] or cWB [70] algorithms. BayesWave uses Morlet-Gabor (sine-Gaussian) wavelets for signal reconstruction, while cWB uses Meyer wavelets. Although these wavelet-based methods are a good fit for detection of bounce and early post-bounce parts of SN waveform, they are not suitable for long tails of later parts of the signal [71]. A better approach for detailed triggered surveys is Principal Component Analysis (PCA), where a set of orthogonal functions is created from many simulated supernova waveforms [34, 72–74]. In the work by Logue [72] it is shown how different mechanisms of explosions produce different SN waveforms with very distinct principal components. Detection of these waveforms is performed by minimizing the difference between the waveform and the set of principal components, which can be reduced to matched filtering.

Distortions of CCSN gravitational-wave waveforms due to geometrical orientation of the source or errors in calibration of the detector may result in decreased detection probability and wrong estima-

tion of the explosion parameters. Changes of the width of the bounce signal envelope, the frequency shift or even the phase shift could result in wrong estimation of the rotational parameters. Time and frequency shifts of the SASI component could also lead to wrong conclusions about the radius of the shock wave and its duration. Errors in the measurement of frequency evolution of p- and g-modes could lead to incorrect estimation of the core size and mass. Moreover, such distortions could introduce a mismatch between the waveform and principal components used during PCA, as well as reduce cross-correlation between different detectors in the network.

CHAPTER 2

GRAVITATIONAL WAVE DETECTOR GROUP DELAY

When multiple gravitational-wave detectors operate simultaneously, they detect a gravitational wave each in its own moment of time. The time difference between detection arises from different locations of the detectors on Earth. This time difference allows to triangulate the source of the gravitational wave as a point in the sky. Therefore, precise measurement of the signal arrival is important for source localization [75]. In the course of this work we have found that there is additional time delay that originates from the group delay within each interferometer. In this chapter we will explore this *intrinsic delay*. We will consider a quasimonochromatic signal: a signal with Sine-Gaussian envelope and constant carrier frequency. The group delay of such signals depends on the carrier frequency and properties of the transfer function [76]. For gravitational wave interferometers the group delay will also depend on the source location and the polarization of the incoming gravitational wave.

2.1 Complex phase of transfer function

To introduce the main concepts of this chapter it would be helpful to consider first the electromagnetic analogy. In electromagnetic theory a wave $f(t,z)$ traveling from the left ($z<0$) is incident on a slab of dispersive medium at $z \geq 0$. Let its free-space Fourier spectrum be

$$\tilde{E}(\omega) = \int_{-\infty}^{\infty} E(t,0) e^{-i\omega t} dt. \tag{2.1}$$

Then the EM wave in the medium will be described by

$$E(t,z) = \int_{-\infty}^{\infty} \tilde{E}(\omega) e^{i\omega t} e^{-ik(\omega)z} \frac{d\omega}{2\pi}, \tag{2.2}$$

where $k(\omega) = k_0\sqrt{\epsilon(\omega)}$ and $k_0 = \omega/c$ is the free-space wavenumber. In general $\epsilon(\omega)$ is a complex number and therefore $k = \alpha + i\beta$ allowing possible absorption in the medium. Then

$$E(t,z) = \int_{-\infty}^{\infty} \tilde{E}(\omega) e^{i\omega t} e^{-i\alpha(\omega)z} e^{-\beta(\omega)z} \frac{d\omega}{2\pi}. \tag{2.3}$$

Here $\alpha(\omega)$ is known as the propagation factor and $\beta(\omega)$ is the attenuation factor. The first is responsible for the advancement of the phase and the second is for the gradual decay of the amplitude within the medium.

It is our intention to follow this picture as much as possible even though the circumstances can be very different. In case of gravitational wave $h(t)$ producing output $y(t)$ in an one-arm detector we have

$$y(t) = \int_{-\infty}^{\infty} \tilde{D}(\omega)\tilde{h}(\omega) e^{i\omega t} \frac{d\omega}{2\pi}, \tag{2.4}$$

where $\tilde{D}(\omega)$ is the one-arm detector transfer function (1.93). Thus, it is tempting to introduce the notation

$$\tilde{D}(\omega) = e^{-ik(\omega)}, \tag{2.5}$$

even though $k(\omega)$ is not a wavenumber and has the dimensions of radians instead of inverse meters. We can think of $k(\omega)$ as complex phase, whose real part $\alpha(\omega)$ is responsible for phase retardation and imaginary part $\beta(\omega)$ for amplitude attenuation:

$$k(\omega) = \alpha(\omega) + i\beta(\omega). \tag{2.6}$$

Note that both $\alpha(\omega)$ and $\beta(\omega)$ are real functions of ω.

In what follows we will use primes to denote differentiation with respect to frequency:

$$\tilde{D}'(\omega) = \frac{d\tilde{D}}{d\omega}. \tag{2.7}$$

We shall also use the following formulas:

$$\alpha = \frac{i}{2}\ln\left(\frac{\tilde{D}}{\tilde{D}^*}\right), \tag{2.8}$$

$$\beta = \frac{1}{2}\ln\left(\tilde{D}\tilde{D}^*\right), \tag{2.9}$$

and consequently

$$\alpha' = -\mathrm{Im}\left(\frac{D'}{D}\right), \tag{2.10}$$

$$\beta' = \mathrm{Re}\left(\frac{D'}{D}\right), \tag{2.11}$$

where prime denotes differentiation with respect to ω.

Consider now a quasi-monochromatic signal which is obtained from purely monochromatic signal at frequency ω_0 by introducing modulation:

$$h(t) = A(t)e^{i\omega_0 t}, \tag{2.12}$$

where $A(t)$ is the slowly-varying amplitude. By allowing $A(t)$ to be complex function of time we can account for both amplitude and phase modulation.

We assume that the signal is of narrow band and all of its energy is concentrated within the band $\omega \in [-\Delta\omega, \Delta\omega]$. For such a signal, Fourier spectrum $\tilde{A}(\omega)$ becomes negligible for frequencies outside the band. The usual condition for narrow-band signals: $\delta\omega \ll \omega_0$ will be augmented here by another somewhat more stringent condition below.

Fourier transformation of $h(t)$ leads to

$$\tilde{h}(\omega) = \tilde{A}(\omega - \omega_0). \tag{2.13}$$

Consequently, $\tilde{h}(\omega)$ becomes negligible outside the interval $|\omega - \omega_0| < \Delta\omega$. In this case we need to know the transfer function only in the vicinity of ω_0. Then we can approximate:

$$k(\omega) = k(\omega_0) + k'(\omega_0)(\omega - \omega_0). \tag{2.14}$$

Then

$$\tilde{y}(\omega) = D_0 e^{-ik'_0(\omega-\omega_0)}\tilde{A}(\omega-\omega_0), \tag{2.15}$$

where $k'_0 = k'(\omega_0)$ and $D_0 = \tilde{D}(\omega_0)$. This expression allows us to calculate the output signal in time domain:

$$y(t) = D_0 A(t-k'_0)e^{i\omega_0 t}, \tag{2.16}$$

or somewhat more explicitly

$$y(t) = |D_0|A(t-\alpha'_0 - i\beta'_0)e^{i(\omega_0 t-\alpha_0)}. \tag{2.17}$$

Here we recognize the gain $|D_0|$ and the phase shift α_0 that correspond to the carrier frequency ω_0 but that is all. We see that the slowly-varying envelope $A(t)$ is shifted by the *complex* time lapse: $\alpha'_0 + i\beta'_0$. To better understand this result we consider some examples.

2.1.1 Sine-Gaussian signal

Take for example, a slowly-varying amplitude

$$A(t) = e^{-\frac{1}{2}a(t-t_p)^2}, \qquad a \geq 0, \tag{2.18}$$

which results in a sinusoidal signal with Gaussian envelop that is peaked at $t = t_p$ and has a width of $1/\sqrt{a}$.

The spectrum of the amplitude in Fourier domain is also Gaussian

$$\tilde{A}(\omega) = \left(\frac{2\pi}{a}\right)^{\frac{1}{2}} e^{-i\omega t_p} e^{-\frac{\omega^2}{2a}}, \tag{2.19}$$

with the width of the peak given by

$$\Delta\omega = \sqrt{a}. \tag{2.20}$$

Then from equation (2.16) we obtain the filtered signal

$$y(t) = |D_0|e^{-\frac{1}{2}a(t-\bar{t}_p)^2} e^{ia\beta'_0(t-\bar{t}_p)} e^{\frac{1}{2}a\beta'^2_0} e^{i(\omega_0 t-\alpha_0)}, \tag{2.21}$$

where $\bar{t}_p$ is given by

$$\bar{t}_p = t_p + \alpha'_0, \tag{2.22}$$

and indicates the time when the slowly-varying amplitude reaches the maximum.

The resulting wave is still sine-Gaussian but the peak of the amplitude is shifted in time by α'_0 and its carrier frequency is no longer ω_0. Rather, it is given by

$$\bar{\omega}_0 = \omega_0 + a\beta'_0. \tag{2.23}$$

This result can also be seen in Fourier domain. Namely, the spectrum $|\tilde{y}(\omega)|$ has a peak at $\bar{\omega}_0$ and not ω_0. In other words, β'_0 affects the peak frequency of the signal. This is the first example of the signal deformation that is brought by the behavior of the transfer function in the vicinity of the carrier frequency.

There is also a correction to the signal by a factor of $e^{\frac{1}{2}a\beta'^2_0}$ which makes the amplitude slightly bigger. Since it is a constant factor it does not contribute to signal distortions or the time shifts.

2.1.2 Chirp signal

We have seen that the peak of the slowly-varying amplitude becomes shifted in time by α'_0 and that the carrier frequency is shifted by the quantity proportional to β'_0. However, to fully understand the role of parameter β'_0 in the filtering process we have to take a somewhat more complicated waveform. We now consider the signal with linear frequency chirp:

$$\omega(t) = \omega_0 + b(t - t_p). \tag{2.24}$$

It is well known that with chirp signals the reference frequency ω_0 loses its meaning and can be set an arbitrary value by shifting time. To fix ω_0 we can choose it to be the frequency at which the spectral amplitude reaches its maximum. This is the reason for t_p (amplitude peak time) in equation (2.24).

To generate such a signal we take the slowly-varying amplitude in the form:

$$A(t) = e^{-\frac{1}{2}(a-ib)(t-t_p)^2}. \tag{2.25}$$

Combined with the phase factor $e^{i\omega_0 t}$ it will give us the desired chirp signal. Note that the spectrum of the signal is still given by the Gaussian curve. Namely,

$$\tilde{A}(\omega) = \left(\frac{2\pi}{a - ib}\right)^{\frac{1}{2}} e^{-i\omega t_p} e^{-\frac{\omega^2}{2(a-ib)}}. \tag{2.26}$$

From this formula we can find that the width of the peak is given by

$$\Delta\omega = \left(a + \frac{b^2}{a}\right)^{\frac{1}{2}}. \tag{2.27}$$

Then the output of the filter, according to equation (2.16), will yield

$$y(t) = D_0 A(t - k_0')e^{i\omega_0 t}. \tag{2.28}$$

We have thus to consider the following quantity that enters the slowly-varying envelop:

$$W = (a - ib)(t - t_p - k_0')^2, \tag{2.29}$$

which has both real and imaginary parts: $W = U - iV$. Then

$$y(t) = |D_0| e^{i(\omega_0 t - \alpha_0)} e^{-\frac{1}{2}(U - iV)}. \tag{2.30}$$

By separating the real and imaginary parts of W we find that

$$U = a\left(t - t_0 - \alpha_0' - \frac{b}{a}\beta_0'\right)^2 - \left(a + \frac{b^2}{a}\right)\beta_0'^2, \tag{2.31}$$

$$V = b\left(t - t_0 - \alpha_0' + \frac{a}{b}\beta_0'\right)^2 - \left(b + \frac{a^2}{b}\right)\beta_0'^2, \tag{2.32}$$

Note that the last two terms in U and V represent the constant gain and phase shift. It is worthwhile to combine them into r_0:

$$r_0 = \frac{1}{2}\left(a + \frac{b^2}{a}\right)\beta_0'^2 - i\frac{1}{2}\left(b + \frac{a^2}{b}\right)\beta_0'^2. \tag{2.33}$$

Therefore, the output signal can be presented as

$$y(t) = |D_0| e^{i(\omega_0 t - \alpha_0)} e^{-\frac{1}{2}a(t-\bar{t}_p)^2} e^{\frac{1}{2}ib(t-\bar{t}_c)^2} e^{r_0}. \tag{2.34}$$

where the two characteristic times are given by

$$\bar{t}_p = t_p + \alpha_0' + \frac{b}{a}\beta_0', \tag{2.35}$$

$$\bar{t}_c = t_p + \alpha_0' - \frac{a}{b}\beta_0'. \tag{2.36}$$

As a result the instantaneous frequency of this signal is also a linear chirp:

$$\omega(t) = \omega_0 + b\left(t - \bar{t}_c\right). \tag{2.37}$$

Note that it matches the original carrier frequency ω_0 at $t = \bar{t}_c$.

If we consider the slowly-varying amplitude of $y(t)$ we will find that it reaches maximum at $t = \bar{t}_p$. At this time the instantaneous frequency of the signal is not equal to ω_0. This situation is quite different from that of the input signal for which the peak of the amplitude corresponds to the nominal frequency ω_0.

We observe two effects here. Both $\bar{t}_p$ and $\bar{t}_c$ are delayed with respect to their original value t_p by α_0'. Second, one of them is advanced and the other is further delayed in time by quantities proportional β_0'. Therefore, the parameter β_0' is responsible for the separation of $\bar{t}_p$ and $\bar{t}_c$. In particular,

$$\bar{t}_p - \bar{t}_c = \left(\frac{a}{b} + \frac{b}{a}\right)\beta_0'. \tag{2.38}$$

from which it follows immediately that

$$|\bar{t}_p - \bar{t}_c| \geq 2|\beta_0'|. \tag{2.39}$$

Note that this condition does not depend on particular values of parameters a and b.

It can be shown that the maximum of the spectrum of $|\tilde{y}(\omega)|$ takes place at

$$\omega_p = \omega_0 + b\beta_0' + \frac{b^2}{a}\beta_0'. \tag{2.40}$$

This value coincides with $\omega(t)$ at $t = \bar{t}_p$ and is the new carrier frequency. Thus the carrier frequency (ω_p) of the filtered signal is necessarily offset from the carrier frequency (ω_0) of the input signal. Moreover, from equation (2.39) we obtain that

$$|\omega_p - \omega_0| \geq 2|b\beta_0'|. \tag{2.41}$$

Another restriction on the possible values of $\bar{t}_p$ and $\bar{t}_c$ can be obtained as follows. First, take equations (2.31) and (2.32), square them and add

$$(\bar{t}_p - t_p - \alpha_0')^2 + (\bar{t}_c - t_p - \alpha_0')^2 = \left(\frac{a^2}{b^2} + \frac{b^2}{a^2}\right)\beta_0'^2, \tag{2.42}$$

from which it follows that

$$(\bar{t}_c - t_p - \alpha_0')^2 + (\bar{t}_c - t_p - \alpha_0')^2 \geq 2\beta_0'^2. \tag{2.43}$$

Note that this condition does not depend on particular values of the parameters a and b. The inequalities equation (2.41) and equation (2.43) becomes equalities for input signals with $b = \pm a$.

We can conclude that α' is the group delay that affects both the peak of the amplitude and the chirp, while β' is the time shift that offsets the peak from the center of the chirp. In what follows we will call α' *group delay* and β' *chirp delay* and use the following notations for them:

$$\tau = \frac{d\alpha}{d\omega} \quad \text{and} \quad \gamma = \frac{d\beta}{d\omega}. \tag{2.44}$$

The group delay and chirp delay of a more complex system can be expressed through the corresponding delays of the individual components. However, as we can see the delays are not additive quanties and their combined effect is not linear. For example, Michelson interferometer transfer functions (1.124) and (1.125) are the sums of one-arm transfer functions. Therefore, the derivative of the Michelson interferometer transfer functions complex phases k'_{M+} and $k'_{M\times}$ can be derived from

the one-arm detector transfer function complex phase k'_{rt}:

$$k'_{M+}(\omega,\mu,\nu) = f_+(\nu)k'_{\mathrm{rt}}(\nu) - f_+(\mu)k'_{\mathrm{rt}}(\mu), \tag{2.45}$$

$$k'_{M\times}(\omega,\mu,\nu) = f_\times(\nu)k'_{\mathrm{rt}}(\nu) - f_\times(\mu)k'_{\mathrm{rt}}(\mu), \tag{2.46}$$

where

$$f_+(\nu) = \frac{F_+(\hat{\boldsymbol{b}},\hat{\boldsymbol{n}})\tilde{D}(\omega,\nu)}{F_+(\hat{\boldsymbol{b}},\hat{\boldsymbol{n}})\tilde{D}(\omega,\nu) - F_+(\hat{\boldsymbol{a}},\hat{\boldsymbol{n}})\tilde{D}(\omega,\mu)}, \tag{2.47}$$

$$f_+(\mu) = -\frac{F_+(\hat{\boldsymbol{a}},\hat{\boldsymbol{n}})\tilde{D}(\omega,\mu)}{F_+(\hat{\boldsymbol{b}},\hat{\boldsymbol{n}})\tilde{D}(\omega,\nu) - F_+(\hat{\boldsymbol{a}},\hat{\boldsymbol{n}})\tilde{D}(\omega,\mu)}, \tag{2.48}$$

$$f_\times(\nu) = \frac{F_\times(\hat{\boldsymbol{b}},\hat{\boldsymbol{n}})\tilde{D}(\omega,\nu)}{F_\times(\hat{\boldsymbol{b}},\hat{\boldsymbol{n}})\tilde{D}(\omega,\nu) - F_\times(\hat{\boldsymbol{a}},\hat{\boldsymbol{n}})\tilde{D}(\omega,\mu)}, \tag{2.49}$$

$$f_\times(\mu) = -\frac{F_\times(\hat{\boldsymbol{a}},\hat{\boldsymbol{n}})\tilde{D}(\omega,\mu)}{F_\times(\hat{\boldsymbol{b}},\hat{\boldsymbol{n}})\tilde{D}(\omega,\nu) - F_\times(\hat{\boldsymbol{a}},\hat{\boldsymbol{n}})\tilde{D}(\omega,\mu)}, \tag{2.50}$$

These equations allow us to concentrate on properties of the one-arm detector transfer function (1.93). We will use this analysis later to characterize the group delay of Michelson interferometer.

2.2 Numerical estimation of signal parameters

For numerical calculations we developed a method to measure the group delay and visualize it. To determine the delay we need a strict mathematical definition for the signal arrival time. For this purpose we will use the so-called center of the mass of the signal which is defined in a way very similar to the center of mass of a distributed object. However, the center of mass does not reflect all additional distortions of a signal. We are also interested in measurement of the signal instantaneous magnitude and frequency. In general, this is very difficult problem. To achieve these measurements starting from the time series of a real signal we resort to Hilbert transform.

2.2.1 Definition for signal arrival time

The signal arrival time is important for source localization [75] and waveform reconstruction with a network of detectors. Each interferometer in a network of detectors has its own transfer function and dispersion which means that the detected signals will be slightly different. One of the distortions is represented by the time of arrival of the signal and occurs when the detected arrival time is

different from the time of arrival of the gravitational wave. Further exploration of this effect requires mathematical definition of what exactly constitutes the time delay that can be measured.

One of the ways to define the delay between two signals is to find maximum of the cross-correlation function and find from it the corresponding time shift. However, this method would not work in case of a gravitational-wave packet with carrier frequency. The reason is that dispersion of the detector can make the phase of the carrier change independently of the delay of the wave packet.

The question of how to define the time of arrival of the signal is widely discussed in the theory of wave propagation in dispersive media [77–79]. A convenient way to define the signal velocity, and with it, its arrival time, was developed by Smith [78]. He defines the signal arrival time from the center of mass of the signal $E(t)$,

$$t_c = \int_{-\infty}^{\infty} tE^2(t)dt \Big/ \int_{-\infty}^{\infty} E^2(t)dt\,. \tag{2.51}$$

2.2.2 Instantaneous amplitude and frequency of a signal

It is possible to find the instantaneous parameters of a signal first by introducing its Hilbert transform [80]

$$y(t) = \frac{1}{\pi}\mathscr{P}\int_{-\infty}^{\infty}\frac{x(t')}{t'-t}dt', \tag{2.52}$$

where $\mathscr{P}$ denotes the principal value of the integral, x is the original signal and y is its Hilbert transform. Using these two parameters it is possible to build the complex version of the signal

$$z = x + iy. \tag{2.53}$$

For modulated signals with frequency components lying far away from 0, the spectrum of z can be found by truncating the Fourier image of signal x after Nyquist frequency. From this complex version it is possible to find the envelope of the signal and phase

$$A(t) = |z(t)|, \tag{2.54}$$

$$\phi(t) = \arg(z). \tag{2.55}$$

The instantaneous frequency $\omega(t)$ can then be found by taking numerical derivative of ϕ.

These transformations work well only for noise-free signals. For signals with noise the envelope and instantaneous frequency can be estimated from either the spectrogram, or wavelet transform, or synchrosqueezed transform [81], but all these methods are less accurate than the one we used. For the purpose of this work we will consider noise-free signals and use Hilbert transform to analyze them.

2.3 Group delay analysis

The values of τ and γ can be calculated analytically for a one-arm detector transfer function:

$$\tau(\omega,\mu) = T\left(1-\mu\frac{\operatorname{sinc}^2(\varphi_i)+\operatorname{sinc}^2(\varphi_r)}{\operatorname{sinc}^2(\varphi_i)+\operatorname{sinc}^2(\varphi_r)+2\operatorname{sinc}(\varphi_i)\operatorname{sinc}(\varphi_r)\cos(\omega T)}\right), \tag{2.56}$$

$$\gamma = -\frac{1}{\omega}\left(1-2\frac{(\operatorname{sinc}(\varphi_r)\cos(\varphi_i)+\operatorname{sinc}(\varphi_i)\cos(\varphi_r))\cos(\omega T)}{\operatorname{sinc}^2(\varphi_i)+\operatorname{sinc}^2(\varphi_r)+2\operatorname{sinc}(\varphi_i)\operatorname{sinc}(\varphi_r)\cos(\omega T)}\right). \tag{2.57}$$

Next, we analyze several remarkable limits of these equations also show them in Fig. 2.1:

- For $\mu = 0$, $\tau = T$, $\gamma = -T(\operatorname{sinc}(\omega T) - \cos(\omega T))/\sin(\omega T)$
- For $f = 0$, $\tau = T(1-u/2)$, $\gamma = 0$
- For $f/f_{\mathrm{rt}} = 1/2$, $\tau = T(1-u)$, $\gamma = -2T/\pi$. It is the limiting frequency after which group delay can be negative
- For $f/f_{\mathrm{rt}} = 1$, $\tau = T(1-(1+u^2)/2u)$,

$$\gamma = -\frac{T}{\pi}\left(1-\frac{\pi^2(1-u^2)}{4}\frac{\operatorname{sinc}(u\pi/2)}{\cos(u\pi/2)}\right).$$

Similar behavior of τ and γ can be observed for even higher frequencies, as shown in Fig. 2.2. When the frequency increases, the group delay and chirp delay maintain their symmetry property and acquire additional oscillations. The divergence of the group delay for higher frequencies is demonstrated in Fig. 2.3. For a source perpendicular to the arm, the chirp delay tends to infinity for frequency equal to multiple of FSR. Similar behavior can be observed for other source locations.

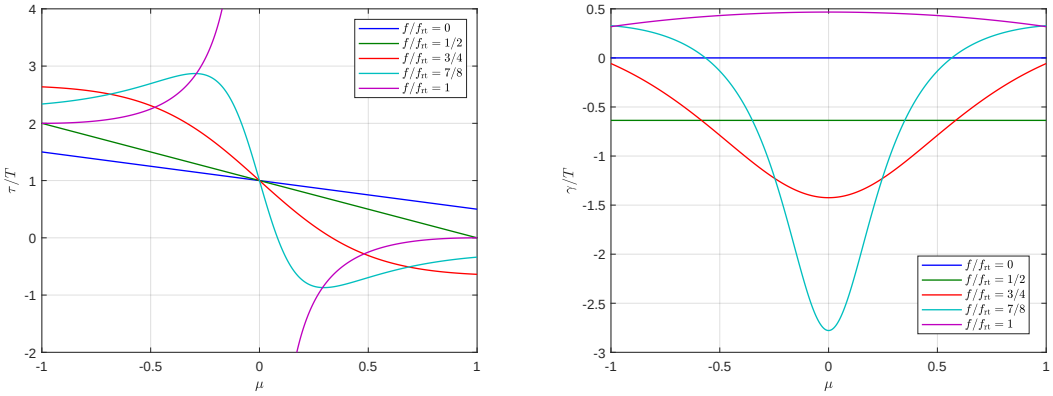

Figure 2.1: Group delay and chirp delay dependence as a function of source location. Frequencies of the gravitational signals are normalized over FSR. These graphs show antisymmetric property of the group delay (left): when μ changes sign, group delay flips relative to time T. At the same time chirp delay (right) has symmetric property.

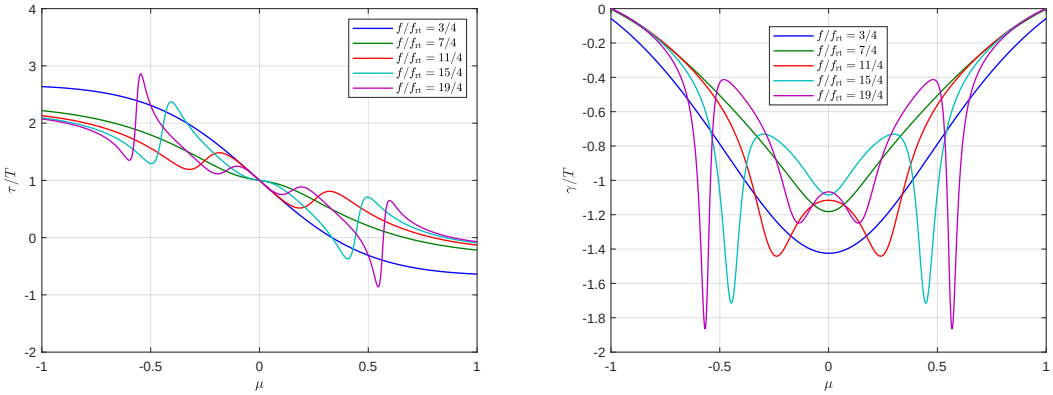

Figure 2.2: Group delay and chirp delay for different source location and high source frequencies. Group and chirp delays have more variance when frequency increases.

For example, the source located at an angle 60° relative to the arm has chirp delay with an unbound value around the frequency equal to 4 FSR.

The equations for group delay and chirp delay are not bound when frequency of the source is multiple of the FSR and $\mu = 0$. We will call such a point the *critical point*. In the vicinity of the critical point the delays can be expressed in terms of small deviations δ and ϵ, where $\mu = \delta$ and $f/FSR = 1 + \epsilon$:

$$\tau = T\left(1 - \frac{2\delta}{\epsilon^2\pi^2 + 4\delta^2}\right), \tag{2.58}$$

$$\gamma = T\left(\frac{\pi^2 - 1}{4\pi} + \frac{\pi\epsilon}{\pi^2\epsilon^2 + 4\delta^2}\right). \tag{2.59}$$

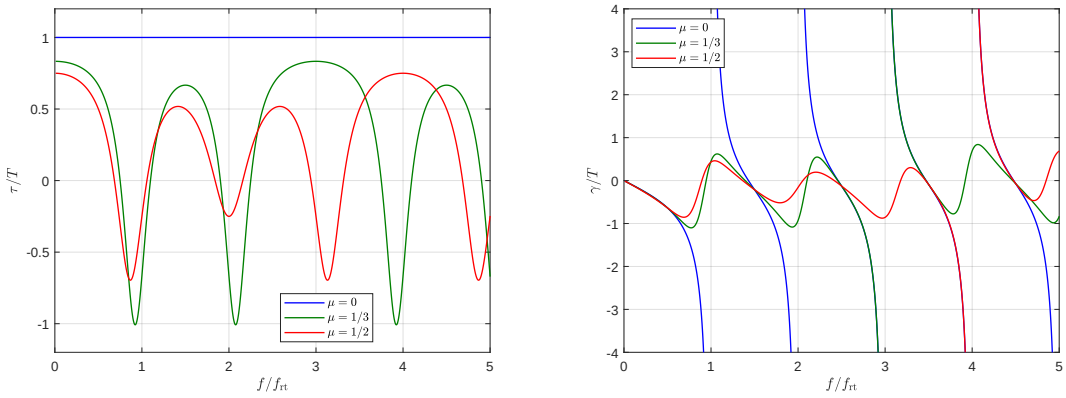

Figure 2.3: Frequency dependence of group delay and chirp delay for different source locations. When amplitude of the transfer function approaches zero, chirp delay of the interferometer becomes inversely proportional to the frequency.

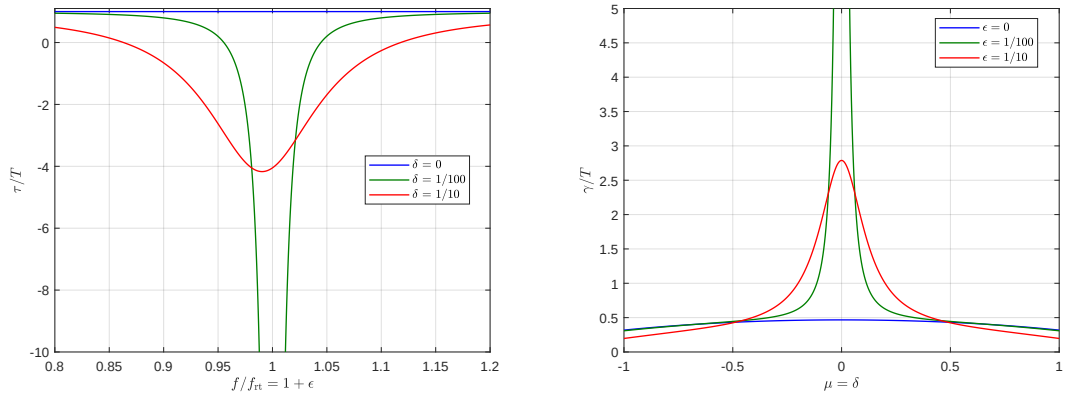

Figure 2.4: Behavior of functions τ and γ next to critical points. The group delay drastically changes with small change of source location. The chirp delay drastically changes with small change of source frequency.

These equations show that $k'(\omega)$ is not well-defined for the critical points. The limit of these expressions depends on the way we take ϵ and δ to zero and the results can be different.

For example, if we set δ to zero first, the group delay will be equal to T and will not depend on ϵ. At the same time, the chirp delay will diverge to infinity. However, if we set ϵ equal to zero first, then the chirp delay will be constant, and the group delay will diverge when δ approaches zero. Illustration of this dependence is in Fig. 2.4.

This asymptotic behavior, which is also shown in Fig. 2.1, indicates that the group delay can be *negative*. Moreover, it can be arbitrarily big if the signal frequency approaches a critical point. In this case the signal will experience significant distortion as shown in Fig. 2.5. The actual shift of the

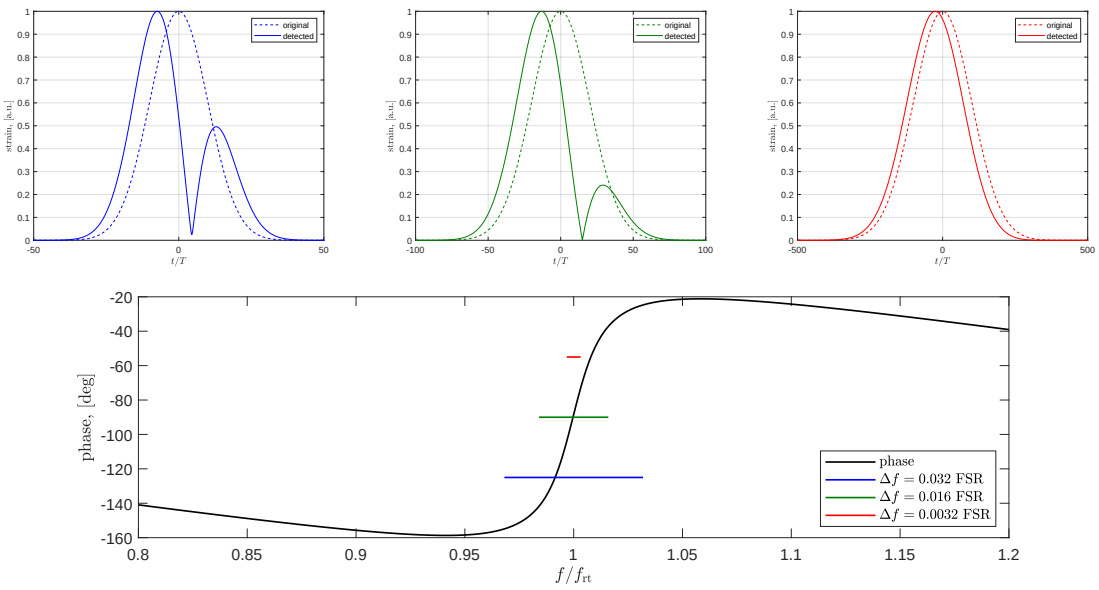

Figure 2.5: Distortion of a signal at carrier frequency 1 FSR by one-arm detector. Source location is at 89°. Derivative of phase of the interferometer transfer function is 27.7 T.

signal approaches the group delay only when the width of the signal increases and bandwidth of the signal decreases. However, in this case the delay of the signal is small in comparison with the signal width. To explain this effect we need to keep in mind that our derivation of the group delay is valid only when the second order terms in Taylor series of the function $k(\omega)$ are small compared to the first order terms. From this observation we obtain the condition when our equations for group and chirp delay can be applicable:

$$\Delta\omega \ll \left| \frac{k'(\omega_0)}{k''(\omega_0)} \right|. \tag{2.60}$$

The negative group delay rises a question about causality of gravitational wave detection. Is it possible to detect a gravitational wave before it reaches the interferometer? Similar questions were considered in the analysis of short EM pulses propagating in the media with dispersion. This topic is very important in the field of superlumenal light propagation [77–79, 82] in which EM pulses with speeds faster than light were observed and reported. A review of these studies is given in a recent book by Oughstun [83]. The author calls the superluminal pulse propagation "just an illusion" arising from the definition of the pulse velocity from the centroid group delay, that does not describe well all the details of the propagation of EM pulses.

The effect of negative group delay was reproduced and measured with a tuned amplified circuits

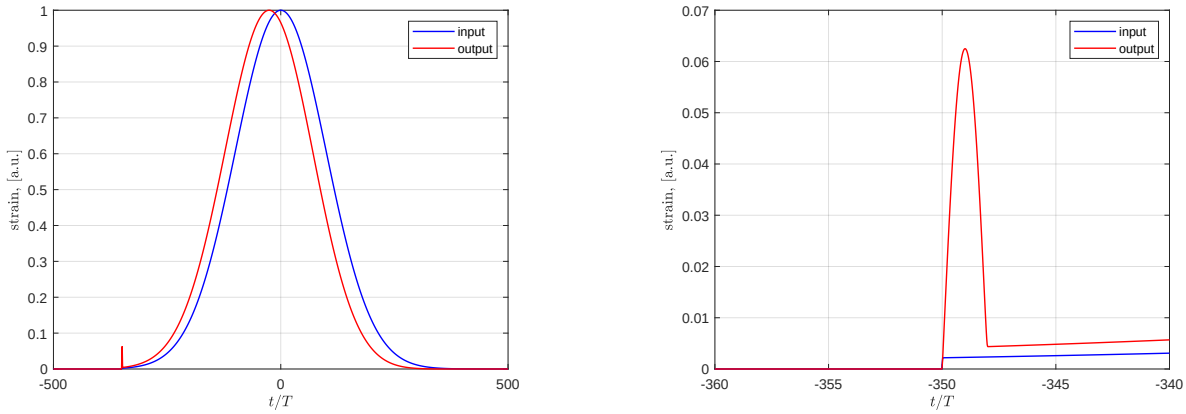

Figure 2.6: Detection of a gravitational wave signal with abrupt start. Input corresponds to the gravitational wave signal, output corresponds to the interferometer output. Right panel shows the moment when gravitational wave starts.

[84–87]. However, the experiments with real systems show that such behavior is not a violation of causality but the consequence of Bode's law for causal systems. Further discussion of this paradox can be found in the work of Garrison [88]. For example, in these experiments the waveform was abruptly turned off during the transmission of the pulse through an electrical circuit. The circuit was tuned to produce negative group delay for these pulses. It was shown that the moment when the output pulse shuts down always happens after the corresponding moment for the input pulse. These effects happen not only for signals with Gaussian-shaped envelope, but also for signals of more a complicated nature [89].

To demonstrate similar effects for a gravitational-wave signal, we conducted numerical simulation of a gravitational-wave detection and the results are shown in Fig. 2.6. The peak of the output signal confirms the negative group delay and appears before the peak of the input signal. However, the output signal starts at the same moment of time as the input signal. In real systems, the output signal is mixed with noise which is why it makes sense to define arrival of the signal at the moment of time when amplitude reaches its maximum. Therefore, we come to the conclusion that the output signal arrived before the input. Thus, the negative delay.

It must be noted that in the ideal system (without noise) we can redefine the time of arrival for signal as the moment of time when the detector output first acquires a non-zero value. In this case, our simulation shows that input and output signals arrive at the same time.

The question about causality comes from the assumption that the peak of the input signal (or

signal center of mass) is the cause of the peak in the output signal. A closer investigation shows that this assumption is not correct. During the detection of an analytical signal the position of the peak can be predicted by observing how the signal changes at the start. This prediction is inadvertently made by the detector and it does not matter if the input signal ever reaches the peak. The predictability of the signal allows the detector to shift it by any time within the signal duration.

Instead of the time delay of the analytic signal the special points of the signal are connected with causality. In these special points the signal is not analytic anymore. Examples of such points are represented by sudden jumps in the signal amplitude or phase [88]. These jumps usually broaden the spectrum of the signal and the validity condition (2.60) is no longer satisfied. As a result, the group delay can not be applied to such signals.

2.4 Michelson interferometer group delay sky maps

The group delay for a Michelson interferometer can be calculated from the group delay and chirp delay of the one-way interferometer by substituting equations (2.56) and (2.57) into equations (2.45) and (2.46). The outcome of the analytical calculations are shown in the bottom two panels of Fig. 2.7. As can be seen from the figure our results agree well with numerical simulations.

To conduct the numerical simulations we applied the interferometer transfer function to the Fourier image of the input signal. We used Hilbert transform to find the envelope of the signal and equation (2.51) to define moment of the signal arrival. These calculations were made for the signal with carrier frequency equal to 0.8 FSR. This frequency is far from the frequency of the nearest critical point located at 1 FSR. However, we still can observe regions with negative group delay; they are shown by graphs with blue color in Fig. 2.7.

We can describe four regions in the sky with different properties. The first region covers azimuth angles $0° < \phi < 90°$ and lies between the two arms of the Michelson interferometer. Most sky locations in this region have negative group delay. This can be explained if we look at the behavior of the round-trip group delay for $mu > 0$, which is shown in Fig. 2.1. In this region both interferometer arms are set in the general direction to the source. As a result, both arms have negative group delay. The opposite region with $180° < \phi < 270°$ has only positive group delays. In this region both interferometer arms make obtuse angles with the direction to the source. This situation corresponds

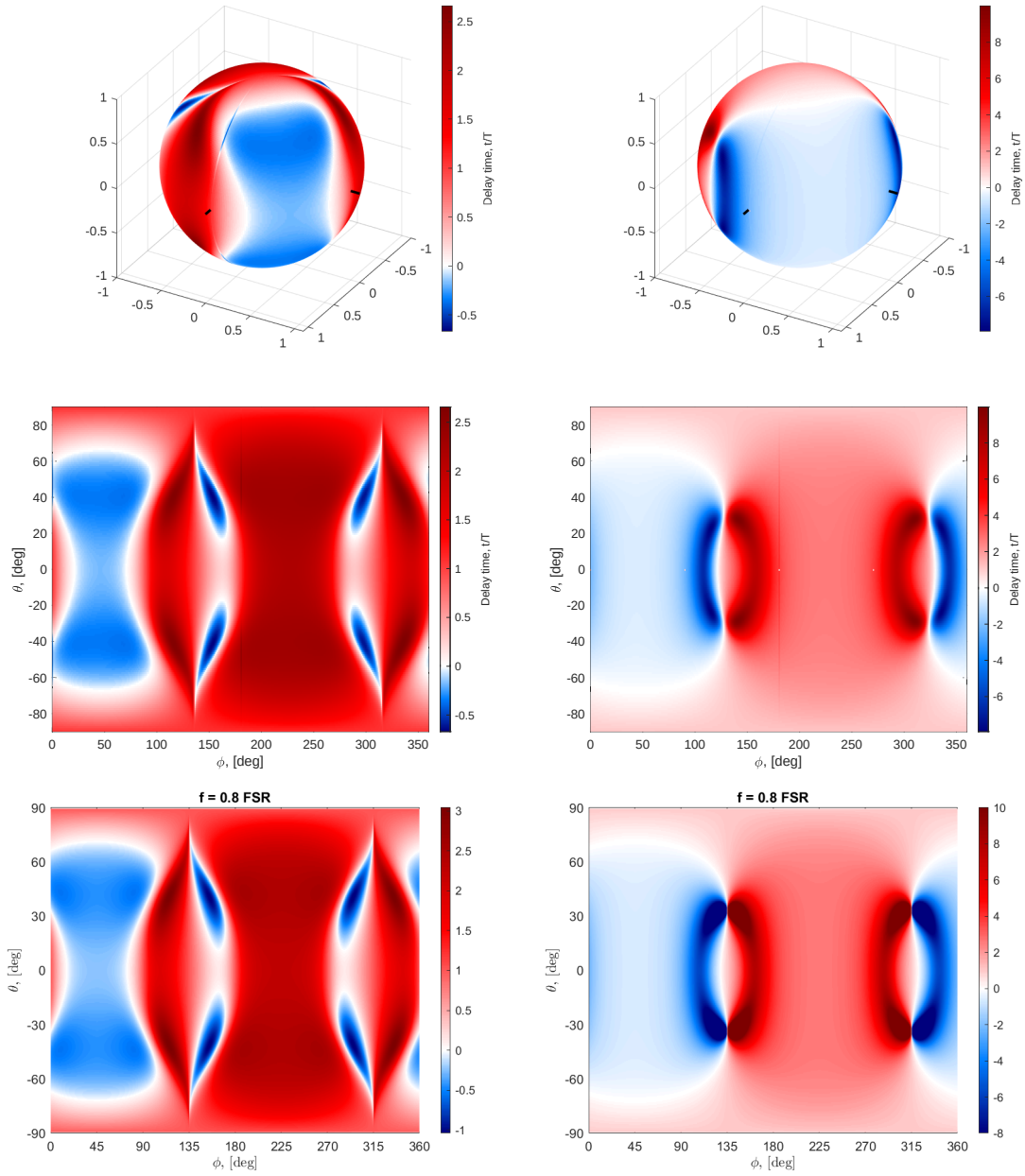

Figure 2.7: Group delay for a Gaussian packet with center frequency 0.8 FSR for Michelson interferometer. Top row: measured group delay of a signal plotted on a sphere. Middle row: measured group delay in cylindrical projection. Bottom row: analytical calculation of the group delay. Left panels show the group delay for + polarization and right panels show the group delay for × polarization. White line on the graph corresponds to the location of the source with zero group delay.

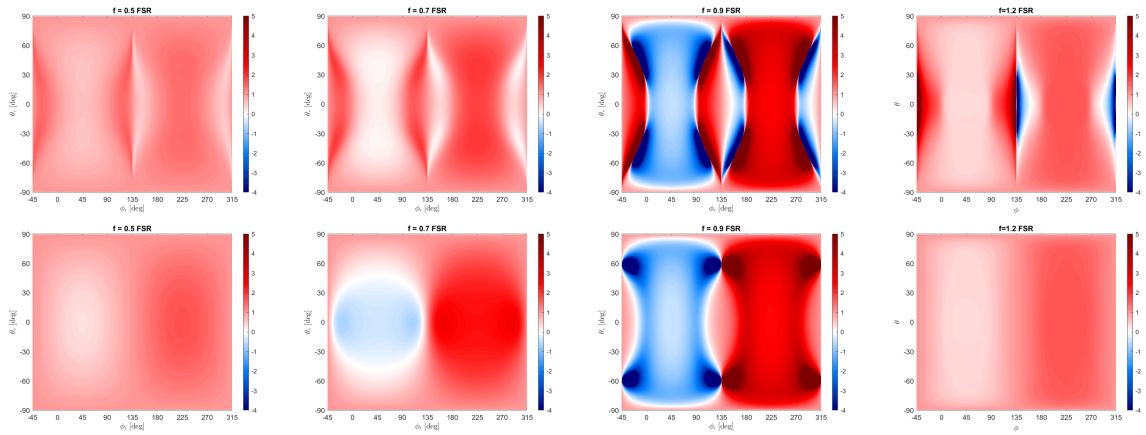

Figure 2.8: Group delay for different frequencies and polarizations. Top panels show group delay for + polarization. Bottom panels show group delay for × polarization. From left to right the signal frequency is 0.5, 0.7, 0.9, and 1.2 FSR.

to the part of the graph 2.1 with $\mu < 0$. In this region both arms have positive group delay. Finally, there are two regions on the sky with $90° < \phi < 180°$ and $270° < \phi < 360°$. In these regions time delay in each arm is different and the resulting time delay depends on the amplitudes of the coefficients (2.47)-(2.50).

To show how the sky map of group delay changes as a function of the signal frequency we carried out analytical calculations of the time delay shown in Fig. 2.8. The negative time delay first appears for × polarization for signal frequency around 0.7 FSR. The region with negative delay grows with frequency when it approaches the FSR. After this critical frequency, the negative delay region shrinks, disappearing at frequency around 1.2 FSR. During this process the pattern on the sky formed by the group delay remains symmetrical. However, the planes of the symmetry do not go through the arms of the interferometer. Instead, they are related to the bisector of the arms. The first plane splits the sky on azimuth $\phi = 45°$. The group delay is symmetric with respect to this plane:

$$\tau(\theta, 45° + \phi) = \tau(\theta, 45° - \phi). \tag{2.61}$$

To highlight this symmetry we plotted the sky maps in Fig. 2.8 for azimuth angle starting from 45° instead of 0°.

The second plane with azimuth $\phi = 135$ splits the sky on two regions that looks antisymmetric relative to each other. However, this symmetry is not perfect: $\tau(\theta, 135°) \neq 0$ which is noticeable in Fig.

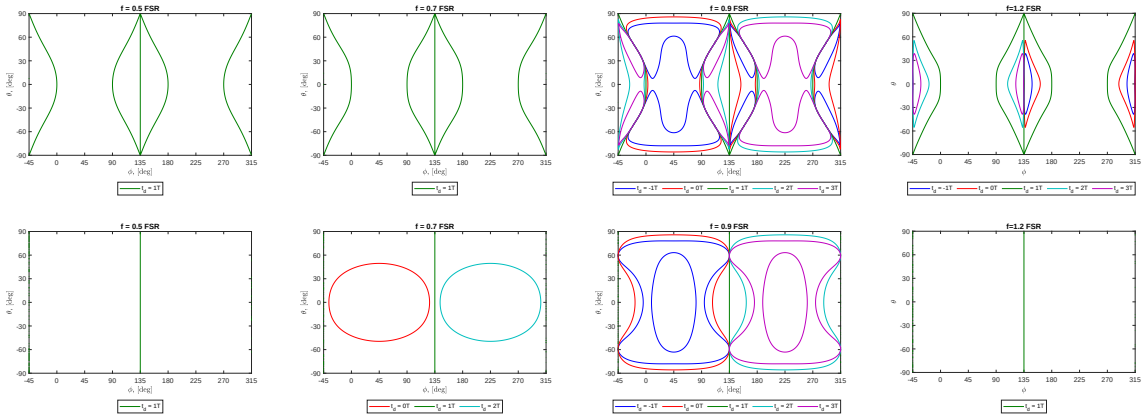

Figure 2.9: Contour plot of the group delay for different frequencies and polarizations. Top panels show group delay for + polarization. Bottom panels show group delay for × polarization. From left to right the signal frequency is 0.5, 0.7, 0.9, and 1.2 FSR.

2.8 for the signal frequency at 0.9 FSR (third column). To understand the antisymmetric property of the time delay we found the contour lines for the sky-maps in Fig. 2.8. In Fig. 2.9 we show the contour plots, and the main contour in this figure is marked with green line. This contour line corresponds to the group delay $\tau = T$, and it can be found on the contour map for any frequency. Moreover, this contour exhibits almost no change for different frequencies. In the equatorial plane, the group delay for + polarization is equal to 1 for azimuth angles 0°, 90°, 180°, 270°. These points on the sky correspond to the arm directions. For the × polarization, $\tau = T$ lines goes along $\phi = 135°$. It means that the group delay is antisymmetric relative to $\phi = 135°$ and time T:

$$\tau(\theta, 135° + \phi) = 2T - \tau(\theta, 135° - \phi). \tag{2.62}$$

This symmetry comes from the one-arm detector impulse response symmetry described by equations (1.87), (1.114), and (1.115).

CHAPTER 3

DISTORTIONS OF CCSN GRAVITATIONAL-WAVE SIGNALS

3.1 Second order approximation of the transfer function complex phase

In previous chapter we showed how first order approximation of the complex phase of transfer function (2.14) gives analytical equations for group delay (2.22) and frequency shift (2.23). Here we will extend this approximation to the second order:

$$k(\omega) = k(\omega_0) + k'(\omega_0)(\omega - \omega_0) + \frac{1}{2}k''(\omega_0)(\omega - \omega_0)^2. \tag{3.1}$$

With this approximation, a quasimonochromatic gravitational wave with envelope (2.25) will be detected as

$$y(t) = D_0\sqrt{\frac{1}{1 + ik_0''(a - ib)}}\exp\left(-\frac{(a - ib)(t - k_0')^2}{2(1 + ik''(a - ib))}\right)e^{i\omega_0 t}. \tag{3.2}$$

If $k_0'' = 0$, our equation will agree with (2.28). In a more complicated situation the real and imaginary parts of k_0' and k_0'' will have somewhat different effect on the detected signal. We will introduce the following notations

$$\begin{aligned} \mathrm{Re}\{k_0'\} &= \tau, \\ \mathrm{Im}\{k_0'\} &= \gamma, \\ \mathrm{Re}\{k_0''\} &= \rho, \\ \mathrm{Im}\{k_0''\} &= \epsilon. \end{aligned} \tag{3.3}$$

With these definitions the time dependence of the envelope function in (3.2) becomes

$$-\frac{(a + ib)(t - k_0')^2}{2(1 + ik_0''(a + ib))} = -\bar{a}(t - \bar{t}_e)^2/2 - i\bar{b}(t - \bar{t}_c)^2/2 + \bar{r} + i\bar{\phi}, \tag{3.4}$$

with

$$\begin{aligned}
\bar{a} &= \frac{(a_n-\epsilon)}{(a_n-\epsilon)^2+(b_n-\rho)^2},\\
\bar{b} &= \frac{(b_n-\rho)}{(a_n-\epsilon)^2+(b_n-\rho)^2},\\
\bar{t}_e &= \tau - \frac{b_n-\rho}{a_n-\epsilon}\gamma,\\
\bar{t}_c &= \tau + \frac{a_n-\epsilon}{b_n-\rho}\gamma,\\
\bar{r} &= \frac{\gamma^2}{2(a_n-\epsilon)},\\
\bar{\varphi} &= \frac{\gamma^2}{2(b_n-\rho)},
\end{aligned} \tag{3.5}$$

where $\bar{a}$ describes the new envelope width, $\bar{b}$ corresponds to the new envelope chirp, $\bar{t}_e$ is the time shift of the envelope, $\bar{t}_c$ is the time shift of the chirp, $\bar{r}$ corresponds to amplitude change due to the slope of the magnitude of a transfer function, and $\bar{\phi}$ corresponds to the additional phase due to the slope of the magnitude of a transfer function, $a_n = a/(a^2+b^2)$ and $b_n = b/(a^2+b^2)$ are renormalized parameters.

Equation 3.5 describes the effect of the real and imaginary parts of derivatives on the output signal. It can be summarized as follows. First, the derivative coefficients are responsible for the time shift of the envelope with imaginary part γ showing how much the signal envelope and signal instant frequency are shifted relative to each other. Second, the second derivative of k is necessary in order to properly describe signal broadening or focusing and chirp change. These derivatives can be ignored when $|\epsilon| \ll a_n$ and $|\rho| \ll |b_n|$.

A special case occurs when the chirp of the original signal is equal to zero. The signal at the output of the detector nonetheless will acquire a chirp from the dispersion effect and the magnitude of the chirp will depend on its carrier frequency and bandwidth. This observation can be important for data analysis. Also it could affect detection of signals if they are based on matched filter approach. To consider this case we assume that the chirp change is negligible when change of the frequency within the signal time span $\Delta t \approx 1/\sqrt{a}$ is much less than signal bandwidth $\Delta f \approx \sqrt{a}$:

$$\bar{b}\Delta t \ll \Delta f, \tag{3.6}$$

or when $a|\rho| \ll (a-\epsilon)^2+\rho^2$. This condition holds true in most cases except when ϵ is on the order of

a. In this case the envelope width will change considerably. Thus, in case of a signal with zero chirp we can neglect second derivatives when $\epsilon \ll a$ or $|\rho| \ll a$.

3.2 Sources of distortions

As can be mentioned in the previous chapter, the reason for signal distortion is variability of the interferometer transfer function. To cancel out this variability, the interferometer calibration and signal whitening is performed [62]. This calibration is performed by passing the raw signal through a filter with transfer function corresponding to the estimation of the interferometer transfer function. The transfer function is estimated by measuring response of the interferometer to the motion of the end test masses. This measurement corresponds to response of the detector to low frequency gravitational wave coming from a direction perpendicular to the interferometer arms. However, this measurement does not take on account possible changes of the transfer function for sources with other locations on the sky [90]. Moreover, this estimation is not precise, and it can also introduce slight distortions of the signal. For example, during interferometer calibration Fabry-Pérot cavity pole frequency $\bar{p}$ is measured. To flatten the response, raw signal from the photo-detector is passed through a notch filter with the zero equal to the measured pole. However, if the actual frequency of the cavity pole p slightly deviates from the estimate the result is that the signal is distorted by a notch filter with the transfer function

$$F(\omega) = \frac{1 - i\omega/\bar{p}}{1 - i\omega/p}. \tag{3.7}$$

Therefore, there are two mechanisms for distortions. In the first mechanism the distortions are due to the position of the source relative to the interferometer; they depend on the source location and the interferometer arm length. These distortions are typically small for low-frequency signals, and increase when the frequencies approach FSR. Even though they make detection of the signal with a network of detectors more complicated, they carry some information about the source location. In the second mechanism the distortions come from the error in calibration of the interferometer sensitivity or in the features of interferometer sensitivity not accounted during the calibration. They will be unique for each detector, and the knowledge of these distortions can be used to improve the calibration procedure. Our approach allows us to treat both of these mechanisms under one formalism which is built on the transfer function from the original GW signal to the final signal after

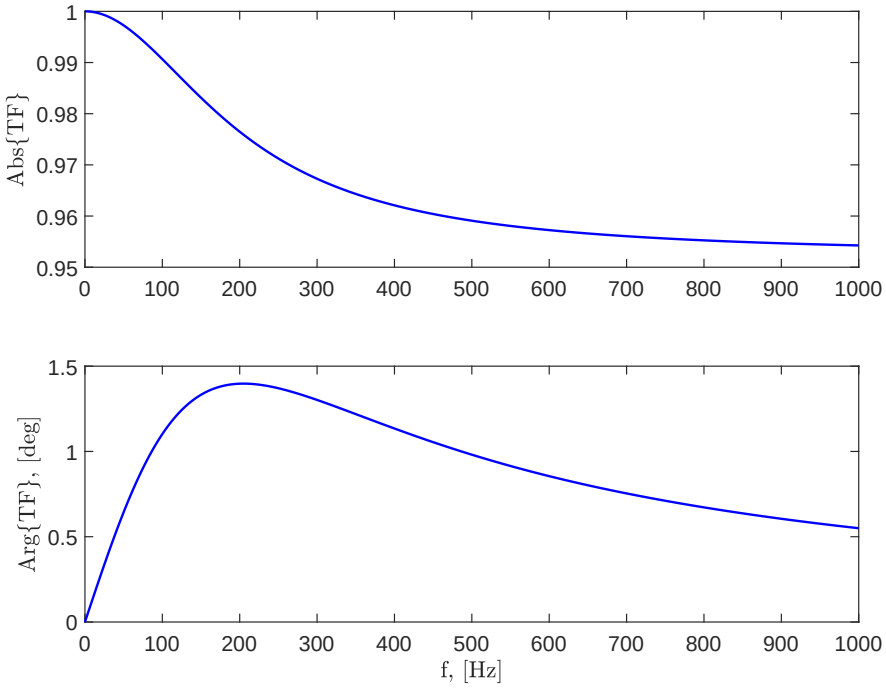

Figure 3.1: Example of a filter that signal passes through when pole of the transfer function is determined during the calibration with 5% error. Top: amplitude transfer function, bottom: phase transfer function.

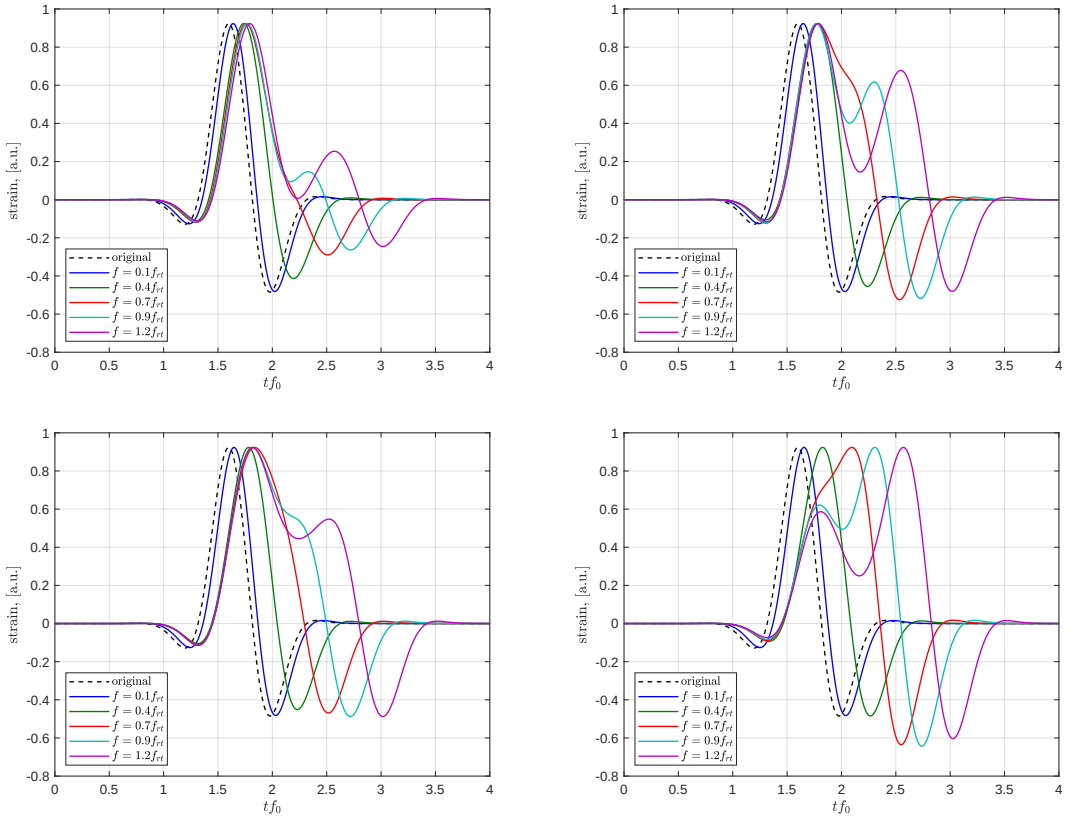

Figure 3.2: Examples of distortion of a pulse by a Michelson interferometer for different frequencies and different source locations. The interferometer response was normalized to have the same amplitude for the largest peak. The azimuth and elevation of the source: top left (30°, 60°), top right (120°, 60°), bottom left (0°, 90°), bottom right (210°, 60°).

the calibration.

3.3 Distortion of a short pulse

When we use the term *short pulse* we will mean a signal with only a few oscillations inside its envelope. An example of this kind of signals is the bounce core oscillations [37, 43, 44]. Examples of the core bounce signals are in Fig. 1.1.

When the center frequency of the pulse f_0 is small compared to the detector FSR, the signal shape does not change, as shown in Fig. 3.2. Even though this signal is not monochromatic [76, 91], it still has small bandwidth compared to the interferometer bandwidth and the first-order approximation for k is good enough. Thus, the only parameters that change are the signal amplitude and the signal delay.

For signals with the center frequency higher than FSR/2, the first order approximation is not sufficient, and the second order effects become significant: the envelope broadening and the appearance of chirp. The envelope broadening leads to increased width of the signal and the additional chirp, usually negative, makes the output signal less symmetric with the distance between its zero crossings increasing with time.

When the center frequency of a signal approaches 1 FSR, the transfer function can not be approximated with Taylor series anymore. If the amplitude of the transfer function tends to zero the imaginary part of k tends to negative infinity. In this regime the envelope broadening can take extreme forms with additional oscillations appearing at the top of the envelope peak or at the tail of the signal. When the bandwidth of the signal is broad the response of the interferometer is not defined by properties of the transfer function in the vicinity of the center frequency. Then the output of the detector can be analyzed with its impulse response. If center frequencies are higher than the FSR the output signal is wider than the input signal with width of the output signal approaching 1/FSR.

The pulse deformations also depend on the source location in the sky. This dependence can be understood from the fact that photons propagating in the fiel of a gravitational wave acquire different phase shifts depending on the propagation direction.

Consider the case when the direction to the source makes an acute angle with the interferometer arm. At first,the photons that hit the beam-splitter propagate in the same general direction as the gravitational wave. They acquire bigger phase shifts and result in bigger amplitude of the signal. Following these photons, the beam-splitter receives the photons which were propagating in the general direction opposite to that of gravitational wave. These photons result in smaller amplitude signal but with longer duration, as shown in Fig. 3.2 top left.

Consider now the case when the direction to the source makes an obtuse angle with the arm. In this case the situation is reversed. At first, the photons that hit the beam-splitter propagate in the general direction opposite of that of gravitational wave, producing smaller but longer signal followed by the bigger and shorter signal, as shown in Fig. 3.2 bottom right. This effect makes the time delay shorter and pulse distortions smaller, with an interferometer response having less dependence on the angle change. A gravitational wave source at an obtuse angle produces signals that are more delayed with stronger dependence of distortions on the source angle. The biggest distortions happen when the direction to the source makes an acute angle with one arm and an obtuse angle with another

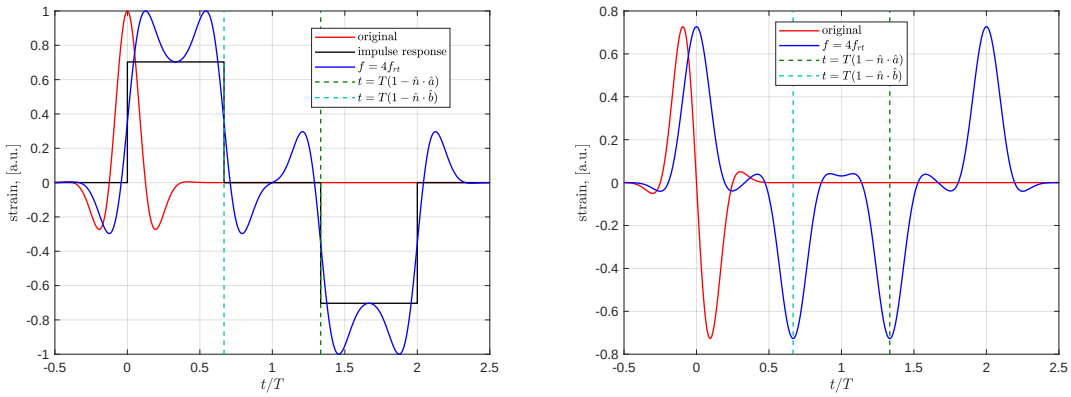

Figure 3.3: Distortion of a symmetric (left) and an asymmetric (right) pulses by a single arm interferometer for pulse frequency equal to 4 FSR and source azimuth 135° and elevation 62°. On the left panel response is overlapped with the interferometer impulse response. Dash-dotted lines on the pictures show moments of arrival of the photons bounced from the end mirrors when signal passed through these mirrors.

arm, as shown in Fig. 3.2 top right. In this case additional peaks appear.

Fig. 3.2 shows that the distortions increase with the pulse frequency. High frequency pulses can be so short that the width of the pulse is smaller than the photon round-trip time. The interferometer response to these pulses carry more information about the interferometer itself than the pulse signal. For example, a pulse can appear copied multiple times, as shown in Fig. 3.3 left. For a pulse of such a high frequency most photons in the arms propagate during full lifetime of the pulse. Thus, the total phase shift of these photons correspond to the integral of the pulse over time. Only the photons that were approaching the beam-splitter or leaving it by the moment when the signal arrived have phase shifts that differ from other photons in the arm. Therefore, interferometer will produce two signals, one at the moment of original pulse arrival, and another one when the photons that left the beam-splitter will finish the round trip. These signals will have phase shifts equal to $\pi/2$ relative to the original signal. The interferometer output between those echoes depend on the constant part of the signal. It equals to zero for an antisymmetric pulse, or nonzero constant value for a symmetric pulse.

Note that other echoes can appear between these two echoes, which are shifted by the photon round-trip time. The additional echoes can appear at $T(1-\hat{\mathbf{n}}\cdot\hat{\mathbf{a}})$ and $T(1-\hat{\mathbf{n}}\cdot\hat{\mathbf{b}})$, as shown in Fig. 3.3. These additional echoes are produced by the photons reflected by the end test mass at the moment of the signal arrival. The phase shifts acquired by these photons depend on the direction of propagation

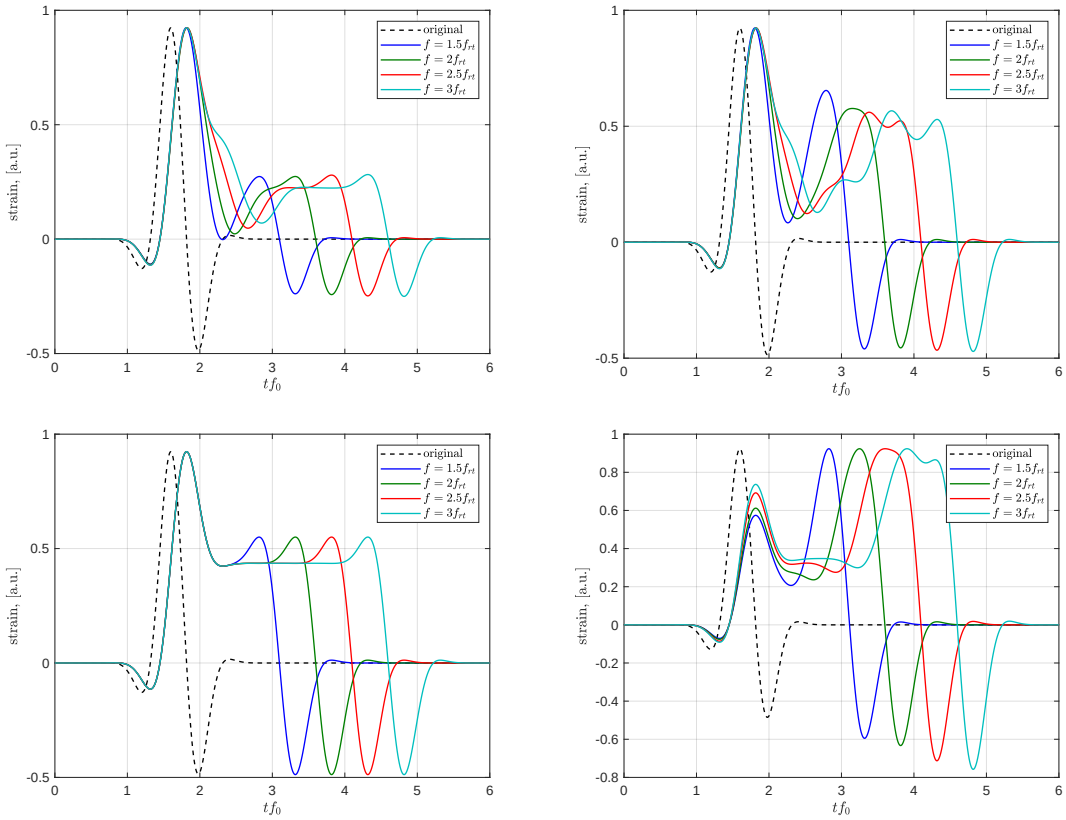

Figure 3.4: Examples of distortion of a pulse by Michelson interferometer for different frequencies and different source locations. Here the frequencies are much higher than the FSR. The interferometer response was normalized to have the same maximum value as the original signal. Azimuth and elevation of the source: top left (30°, 60°), top right (120°, 60°), bottom left (0°, 90°), bottom right (210°, 60°).

		(ϕ, θ)			
		$(30°, 30°)$	$(120°, 30°)$	$(0°, 0°)$	$(210°, 30°)$
$f/f_{\rm rt}$	0.1	43%	21%	98%	43%
	0.4	32%	14%	73%	32%
	0.7	18%	8%	38%	18%
	0.9	14%	7%	20%	14%
	1.2	12%	5%	15%	12%

Table 3.1: Cross-correlation of the signals from Fig. 3.2 with original signals.

of these photons. Moreover, these echoes can appear when the signal propagates at either acute or obtuse angle relative to the arm.

The cross-correlation of the original signal and the detected signal plays an important role in the algorithms for detection of gravitational waves. This cross-correlation changes over the sky, as shown in table 3.1. It is important to note that the cross-correlation is not maximal for source located directly above the interferometer. In fact, the most sensitive direction can take place at an angle relative to the $\hat{\boldsymbol{z}}$ axis.

Another interesting property of the interferometer is the symmetry of its response function. For the sources directly above or below the interferometer, the symmetry of the response function corresponds to the symmetry of the signal. This is not true for gravitational waves coming from sources at other angles. Nevertheless, the response function still has some symmetry properties. The response for the sources with opposite azimuth (e.g. 30° and 210°) can be very different, but the cross-correlation coefficient for these angles is the same. The reason for these similarities comes from the symmetry of the impulse response for these angles. It is possible to show that the one-arm detector transfer function has property

$$\tilde{M}(\omega, \phi, \theta) = e^{-2i\omega T} \tilde{M}^*(\omega, \phi + 180°, \theta), \tag{3.8}$$

where T is one way photon travel time. Since the interferometer impulse response is the inverse Fourier transform of the transfer function the impulse response for adjacent angles are related:

$$M(t, \phi, \theta) = M(2T - t, \phi + 180°, \theta). \tag{3.9}$$

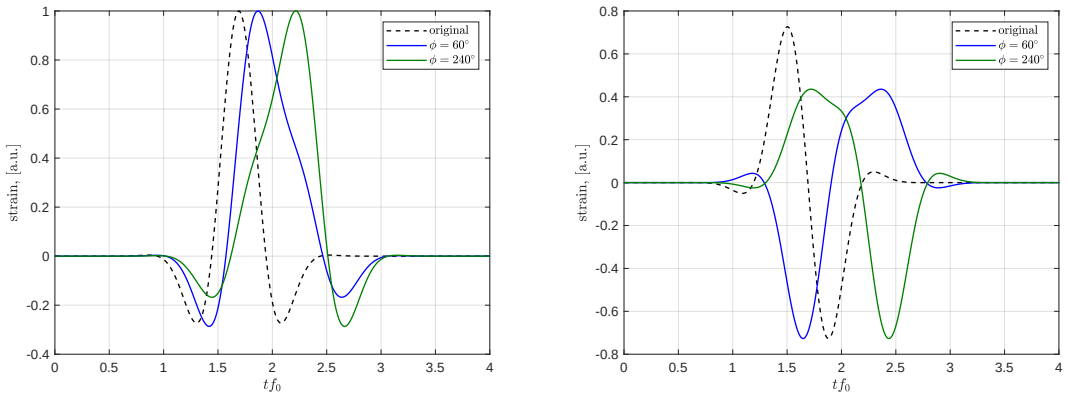

Figure 3.5: Interferometer normalized response to symmetric and asymmetric signals with center frequency $f = 0.7 f_{\rm rt}$. On the left: original signal is symmetric, so response of the arm has symmetric property relative to the moment of time $t = 2.3T$. On the right original signal is antisymmetric, so response has antisymmetric property relative to the same moment of time.

The interferometer response to a signal $s(t)$ will be

$$x(\mu, t) = \int_{-\infty}^{\infty} M(\mu, t-\tau) s(\tau) d\tau. \tag{3.10}$$

Now lets assume that our signal has a symmetry property such that there is a moment in time t_0 for which

$$s(t_0 + t) = s(t_0 - t). \tag{3.11}$$

By substituting this equation and the relation for the impulse response (3.9) into (3.10) we can find

$$x(t, \phi, \theta) = x(2T + 2t_0 - t, \phi + 180^\circ, \theta), \tag{3.12}$$

or

$$x(T + t_0 + t, \phi, \theta) = x(T + t_0 - t, \phi + 180^\circ, \theta). \tag{3.13}$$

This symmetry property is illustrated in Fig. 3.5.

3.4 Distortion of a Sine-Gaussian wave packet

We characterize a Sine-Gaussian signal by the center frequency f_0, the envelope width σ_t, the bandwidth $\sigma_\omega = 1/\sigma_t$, and the chirp parameter b that shows how the instantaneous frequency changes

with time: $f(t) = f_0 + bt$. This kind of signals can approximate well SASI mode of CCSN gravitational-wave signal. Example of this mode can be found in the left panel of Fig. 1.2.

We assume that the Sine-Gaussian signal bandwidth is much smaller than the interferometer FSR, so that the response of the interferometer to such signals depends on the behavior of its transfer function in the vicinity of the signal center frequency. To analyze the process of detection, we expand the complex phase function $k(\omega) = i \ln \tilde{D}(\omega)$ into Taylor series near the center frequency. The zeroth order term corresponds to signal attenuation and signal phase shift, which do not change the envelope shape or its frequency dependence. The first order term, which has the order $O(T/\sigma_t)$ is responsible for the envelope time shift τ and the frequency shift Δf of the signal. The second order term, which has the order $O((T/\sigma_t)^2)$, is responsible for the envelope width change $\Delta\sigma_t$ and chirp factor b. These distortions depend not only on the signal center frequency and the interferometer FSR, but also on the signal bandwidth. Fortunately, we can introduce the normalization constant that removes this dependence. Later on we will provide a stricter mathematical derivation of the normalization parameters. Here we will use simple dimensional and physical arguments.

The transfer function is a function of the dimensionless argument ωT, which makes natural the normalization of signal frequency with the interferometer FSR:

$$\omega T = \pi \frac{f_0}{f_{rt}}. \tag{3.14}$$

Other time-based parameters of the Sine-Gaussian signal (envelope time shift and envelope width change) can be normalized over its envelope width σ_t, while the frequency parameters (frequency change and chirp) can be normalized over the signal bandwidth σ_f. Thus, the envelope time shift as the first order distortion,

$$\frac{\tau}{\sigma_t} = O\left(\frac{T}{\sigma_t}\right) \tag{3.15}$$

can be normalized into

$$\frac{\tau}{T} = O(1). \tag{3.16}$$

The frequency shift

$$\frac{\Delta\omega}{\sigma_\omega} = O\left(\frac{T}{\sigma_t}\right) \tag{3.17}$$

can be normalized into

$$\frac{\Delta\omega}{T\sigma_\omega^2} = O(1). \tag{3.18}$$

The envelope width

$$\frac{\Delta\sigma}{\sigma_t} = O\left(\left(\frac{T}{\sigma_t}\right)^2\right) \tag{3.19}$$

can be normalized into

$$\frac{\Delta\sigma\sigma_t}{T^2} = O(1). \tag{3.20}$$

To treat the chirp parameter similarly we can consider the frequency change within the signal envelope $b\sigma_t$ normalized over signal bandwidth σ_ω

$$\frac{b\sigma_t}{\sigma_\omega} = O\left(\left(\frac{T}{\sigma_t}\right)^2\right), \tag{3.21}$$

with the corresponding normalization

$$\frac{b}{T^2\sigma_\omega^4} = O(1). \tag{3.22}$$

Additionally, we will define the quality factor $Q = \omega_0/\sigma_\omega = 2\pi f_0\sigma_t$ which describes the number of signal oscillations within its width. For a quasimonochromatic signal $Q^{-1} \ll 1$.

3.4.1 First order distortions: time shift and frequency shift

For a Sine-Gaussian signal

$$h(t) = h_0 \exp\left(-\frac{t^2}{2\sigma_t^2}\right)\exp(i\omega_0 t) \tag{3.23}$$

we can expand the transfer function near the center frequency ω_0,

$$\tilde{D}(\omega) \approx \exp\left[ik_0 + ik_0'(\omega-\omega_0)\right] \tag{3.24}$$

with the response

$$x(t) = x_0 \exp\left(-\frac{(t-k_0'(\omega_0))^2}{2\sigma_t^2}\right)\exp(i\omega_0 t). \tag{3.25}$$

First derivative of k has the order of magnitude T except for some special frequencies where the amplitude of the transfer function approaches 0.

Let $k_0' = \tau + i\gamma$. Then we can rewrite x as

$$x(t) = x_0' \exp\left(-\frac{(t-\tau)^2}{2\sigma_t^2}\right)\exp(i(\omega+\gamma/\sigma_t^2)t). \tag{3.26}$$

From this equation it follows that the envelope of the signal will be delayed by

$$\tau = \mathrm{Re}\{k_0'(\omega_0)\} = O(T) \tag{3.27}$$

and the frequency of the signal will change by

$$\Delta f = \frac{\gamma}{2\pi\sigma_t^2} = O(T/\sigma_t^2). \tag{3.28}$$

We will use these approximate values for normalization: T for the time shift of the signal and $T\sigma_f^2$ for the frequency shift.

The slope of the phase of the transfer function corresponds to the signal group delay giving rise to the phenomenon of a signal time shift. By signal time shift we will understand shift of the envelope position in time relative to the envelope of the original signal. This shift corresponds to the difference of arrival times defined by equation (2.51).

The time shift has order of magnitude comparable to the round-trip time. The delay is much less than the signal width for a quasi-monochromatic signal with high quality factor, as shown in Fig. 3.6. When the phase response of the transfer function has positive slope it results in negative time shift, shown by turquoise line on the right pane of Fig. 3.6. This effect does not break causality [88] and same effect happens during the pulse propagation in dispersive media [77–79] or electronics [86, 92–94].

Big deviations of the time delay from the photon one-way transit time happens only around critical frequencies when the signal frequency is equal to multiple of FSR, as shown in Fig. 3.7. The group delay for some cases can become negative when signal frequency approaches the multiple of FSR. Numerical simulations of the group delay in the interferometer agree with analytical calculations of the interferometer transfer function based on the Taylor expansion, as shown in Fig. 3.8.

If the phase part of the interferometer transfer function changes the signal delay, the amplitude part affects the center frequency of the signal. The interferometer can be viewed as a linear filter that

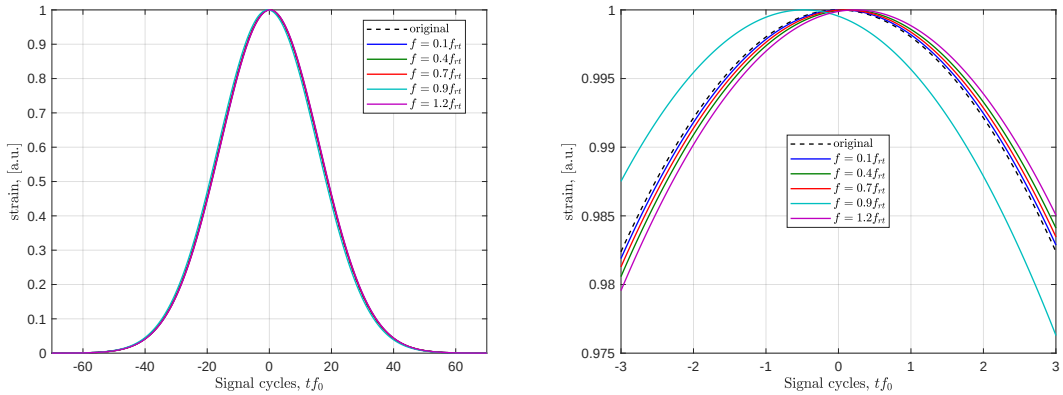

Figure 3.6: The envelope of the response of a Michelson detector to Sine-Gaussian signal coming from a source with azimuth 30° and elevaton 60°. Left: full envelope, right: zoom to the top part of the envelope

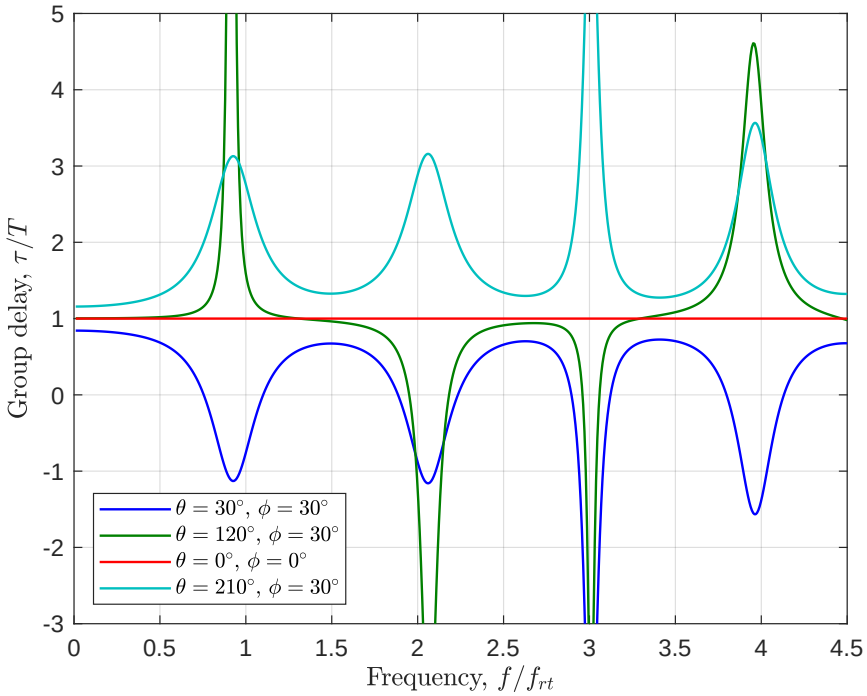

Figure 3.7: The dependence of the interferometer group delay with frequency. The group delay is normalized over the photon one-way transit time.

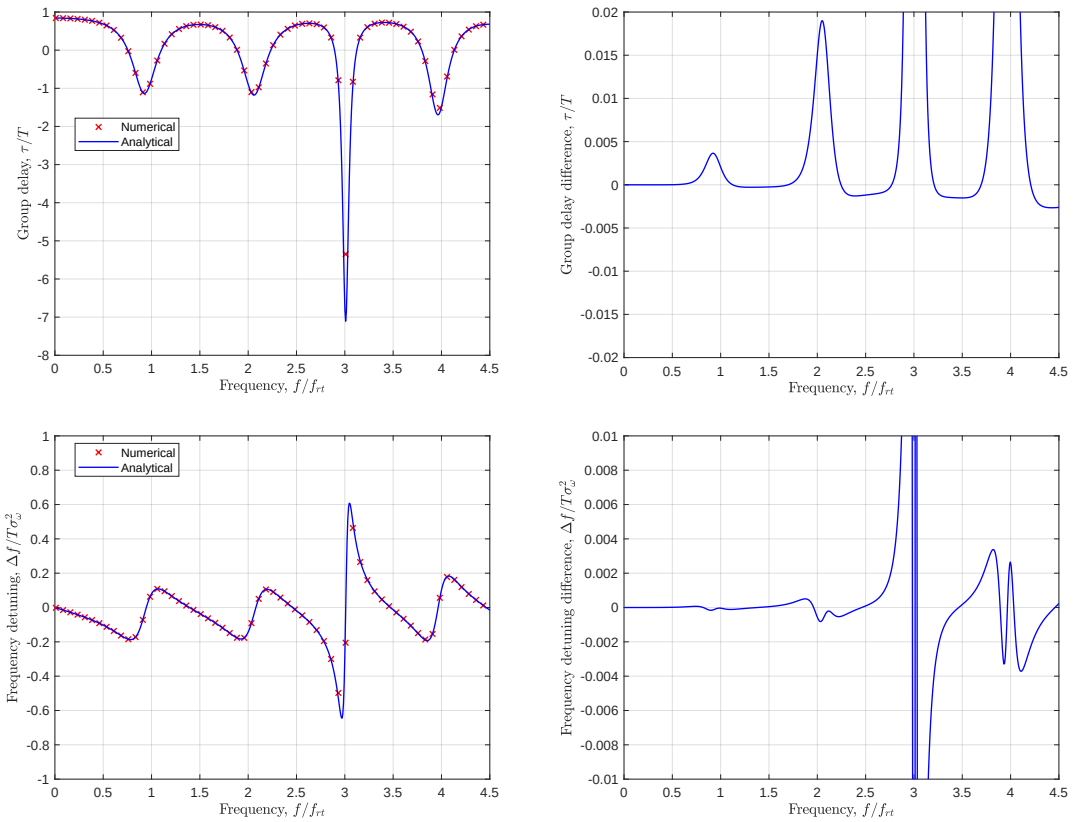

Figure 3.8: The difference between the numerical simulation and analytical calculation of the group delay (top) and the frequency detuning (bottom). The calculations were made for the source located at (30°, 60°). The analytical calculations of the group delay show good agreement with the numerical simulations for all frequencies, while the analytical calculations of the frequency detuning have drastic difference with numerical simulations for the signal with frequency close to 3 FSR.

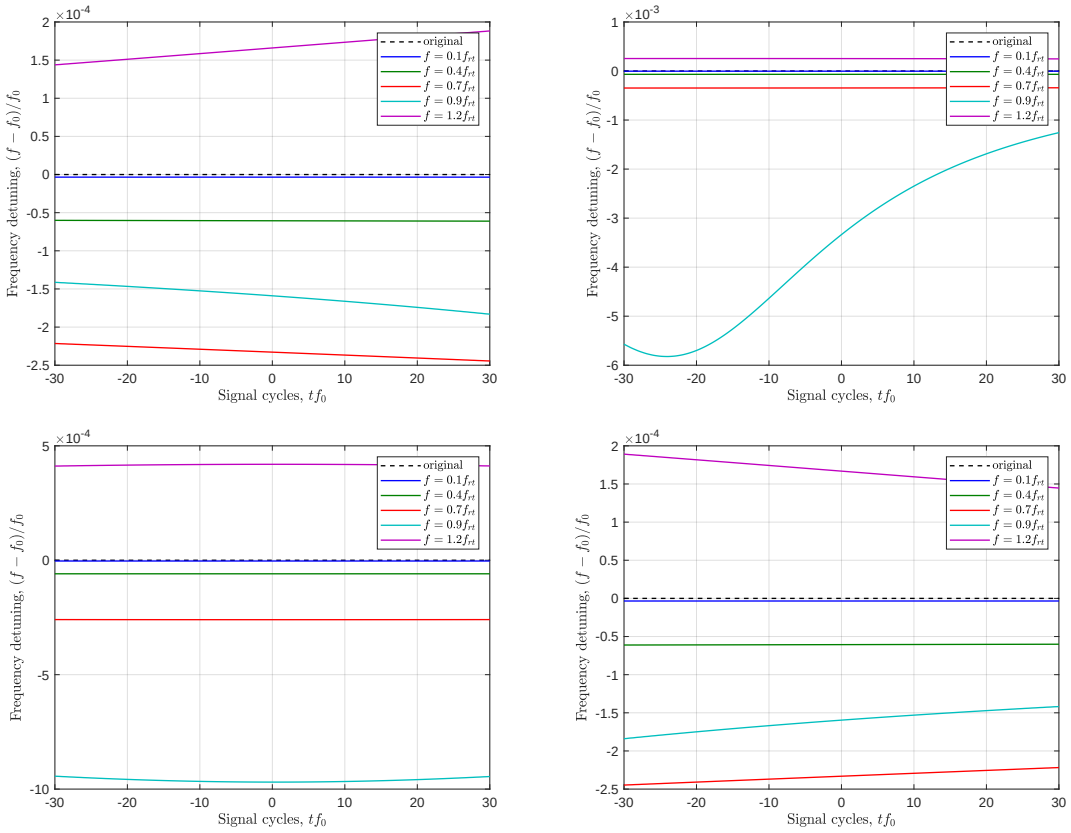

Figure 3.9: Instantaneous frequency detuning produced by a Michelson interferometer for different source location. Azimuth and elevation of the source: top left (30°, 60°), top right (120°, 60°), bottom left (0°, 90°), bottom right (210°, 60°). These pictures demonstrate deviation of the instantanious frequency from the original signal, as well as small chirpness of the output signal.

amplifies some frequencies in the signal while it attenuates the others. The instantaneous frequency of the signal restored with the Hilbert transform is shown in Fig. 3.9. Note that the input signal with constant frequency can acquire the frequency shift and the slope. To pinpoint the exact value of center frequency we measure it at the center of the signal envelope. The slope of the instantaneous frequency as a function of time at this point corresponds to the chirp parameter.

The resulting normalized frequency detuning is shown in Fig. 3.10. Because of the high quality factor for quasi-monochromatic signals, the actual frequency detuning is a couple orders of magnitude less than the signal bandwidth, except at some special points when the carrier frequency is equal to multiple of FSR.

The estimations of the group delay and the frequency detuning from numerical simulations agree well with equations (3.27) and (3.28) that can be derived from the interferometer transfer function,

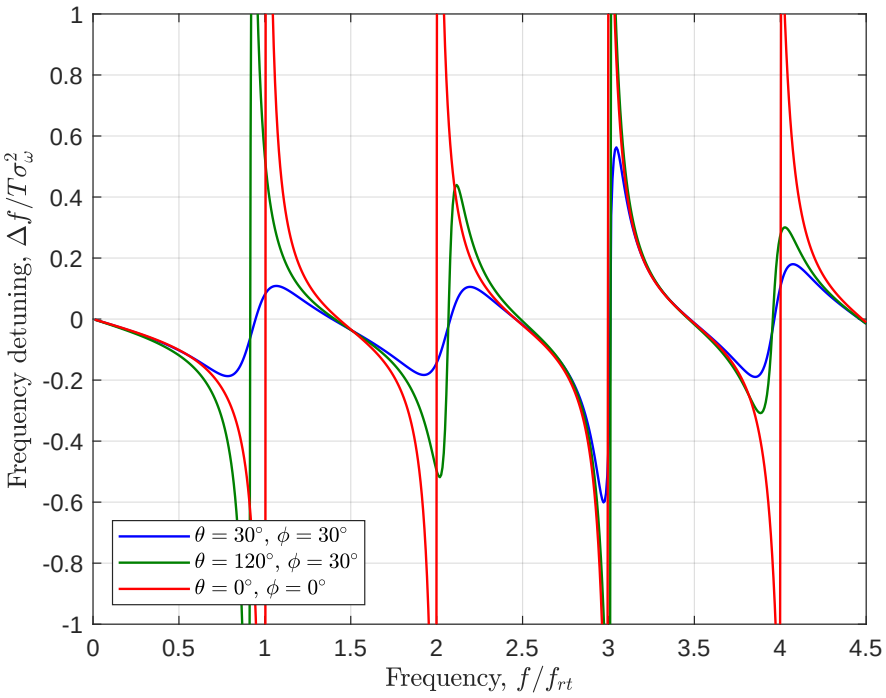

Figure 3.10: The frequency detuning of a single arm detector normalized over $T\sigma_f^2$. The lines for sources with opposite azimuths and same elevation (e.g. 30° and 210°) match each other because the amplitude of the transfer function has the same dependence on frequency for such locations.

as shown in Fig. 3.8. The only time when the frequency detuning does not agree with the equation is when the frequency of the signal corresponds to a critical point of the interferometer, i.e. when the amplitude of the transfer function is zero.

3.4.2 Second order distortions

Similarly to the first order distortions, we can represent the real and imaginary parts of the second derivative of the transfer function as $k_0'' = \rho + i\epsilon$, with $\rho = O(T^2)$ and $\epsilon = O(T^2)$. In this case the new values of the envelope width will be

$$\sigma_t' = \sqrt{\sigma_t^2 - \epsilon + \frac{\rho^2}{\sigma_t^2 - \epsilon}}. \tag{3.29}$$

If we keep only the terms of second order in T/σ_t we obtain

$$\sigma_t' = \sigma_t - \frac{1}{2}\frac{\epsilon}{\sigma_t}, \tag{3.30}$$

with the approximate value of pulse broadening

$$\Delta\sigma_t = -\frac{1}{2}\frac{\epsilon}{\sigma_t} = O\left(\frac{T^2}{\sigma_t}\right). \tag{3.31}$$

It is important to note that this approach is valid only when $\epsilon < \sigma_t^2$. Otherwise, the amplitude of the transfer function increases faster than the spectrum of the signal decreases, which requires to take into account higher order derivatives of k to make sure that the integral in (2.4) converges.

The value of the acquired chirp is

$$b = \frac{\rho}{(\sigma_t^2 - \epsilon)^2 + \rho^2}, \tag{3.32}$$

and if we keep only the second order terms

$$b = \frac{\rho}{\sigma_t^4} = O\left(\frac{T^2}{\sigma_t^4}\right). \tag{3.33}$$

We will use O-values for normalization of $\Delta\sigma_t$ and b.

We can estimate the envelope width in the same way as we estimated the envelope center. From the analytic signal we can find the envelope A and estimate its width:

$$\sigma_e = \sqrt{2\frac{\int_{-\infty}^{\infty}(t-t_e)^2 A^2(t)dt}{\int_{-\infty}^{\infty}A^2(t)dt}}. \tag{3.34}$$

The chirp can be found from the phase of the analytic signal. The derivative of the phase gives us the frequency for different moments of the time, and the slope of the frequency for moment t_e is estimation of the signal chirp factor.

Usually the slope of the interferometer transfer function $|\tilde{D}(\omega)|$ decreases and the amplitude of the transfer function looks like a parabola with its branches pointing down. Therefore, when we multiply the signal spectrum by this transfer function the central part of the signal spectrum is amplified relative to the edge parts. As the result, the bandwidth of the signal decreases, which makes envelope of the signal broader. However, the slope of the interferometer transfer function increases in the vicinity of the critical frequency and the opposite effect will take place: the signal envelope will become narrower, as shown in Fig. 3.11. This effect is also referred as pulse focusing in [76].

When the slope of the phase of the transfer function changes with frequency, different frequency components of the signal will have different group delays. This will result to the shift of different frequencies relative to each other, resulting to the chirp of the output signal. This effect is shown in Fig. 3.12.

The numerical calculations of the second order distortions agrees well with the analytical equations (3.31) and (3.33), which is illustrated in Fig. 3.13. The with the biggest mismatch between analytical equations and numerical simulations happen for frequencies equal to the multiple FSR.

3.5 Distortions of signals with changing frequency

In this section we will consider the distortion of signals from a resonance system with changing parameters. One example of such a system is core oscillations during CCSN which produces a gravitational wave signal. This type of signal contains different oscillation modes, that carry important information about the explosion process [53, 95]. These modes can last quite long, hundreds of milliseconds, with frequency of the signal changing in the wide range (from hundreds to thousands

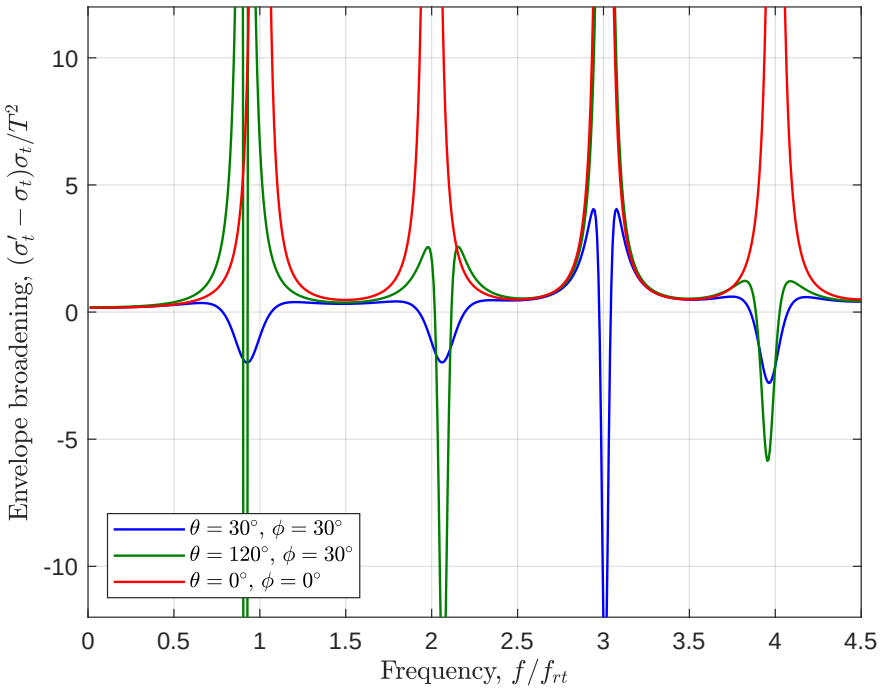

Figure 3.11: Change of a signal envelope width with frequency. Envelope width is normalized over T^2/σ_t. Lines from opposite azimuths (e.g. 30° and 210°) match each other because they have matching amplitudes of the transfer function for those angles.

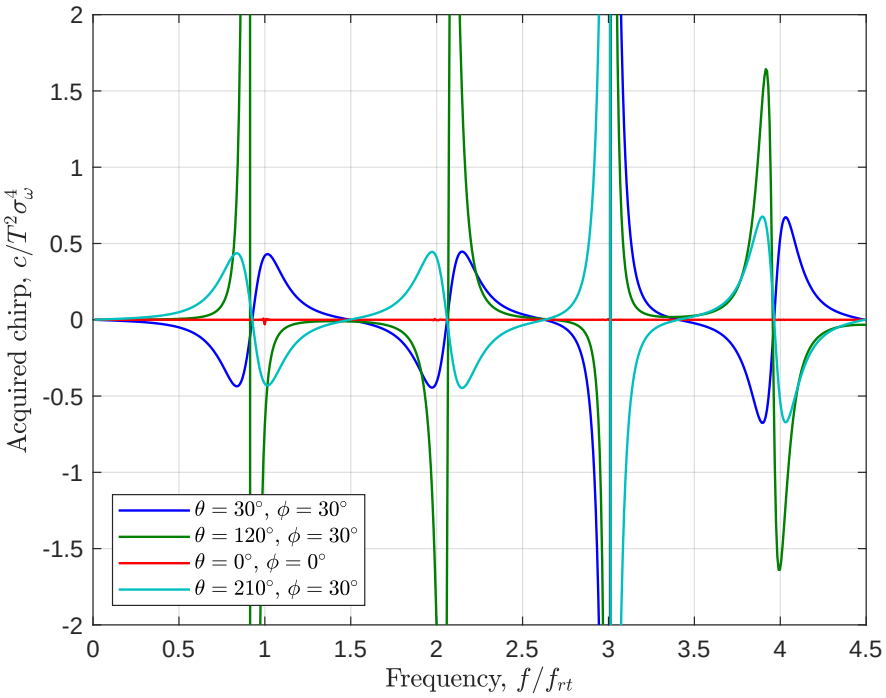

Figure 3.12: The chirp acquired by a signal after the interferometer normalized over $T^2\sigma_f^2$.

of hertz). These modes are shown in the bottom right panel of Fig. 1.1, as well as right panel of Fig. 1.1. The frequency sweep, attributed to these signals, shows that this type of signals is not quasi-monochromatic. This makes the problem of distortion characterization more complicated. To simplify it, we will consider only the distortion of the phase component of the signal, because it carries the main information about the explosion process. In addition, we assume that the change of the parameters happens in the adiabatic regime, which means that the change of the frequency within one period of oscillation is small, or

$$b \ll f^2. \tag{3.35}$$

In this case we assume that the frequency shift at each moment of time is described by equation (3.28). To take on account changing frequency we calculate the interferometer parameters for the instantaneous frequency, instead of the carrier frequency:

$$\Delta f(t) = \frac{1}{2\pi}(\tau(\omega(t))b(t) + \gamma(\omega(t))/\sigma_t^2), \tag{3.36}$$

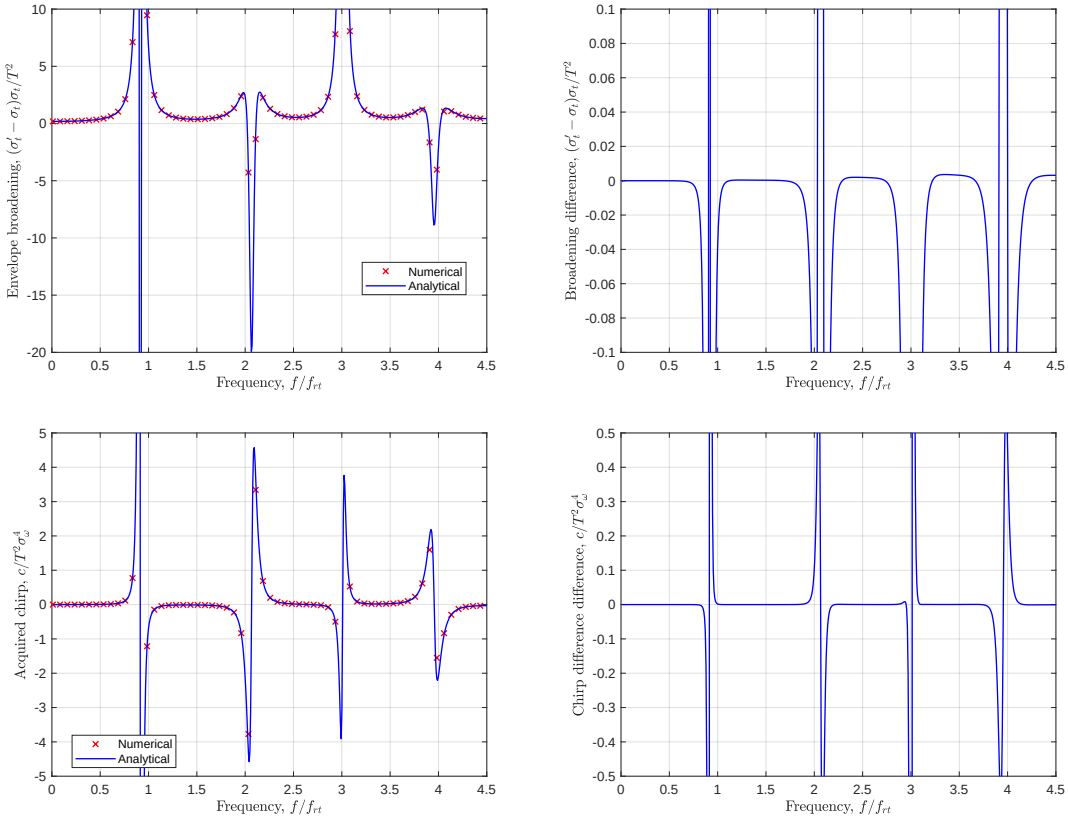

Figure 3.13: The difference between the numerical simulations and analytical calculations for signal broadening (top) and acquired chirp (bottom). The calculations were made for source azimuth 120° and elevation 60°. Discrepancy between the numerical simulation and analytical calculation appear at frequencies when the transfer function approaches zero.

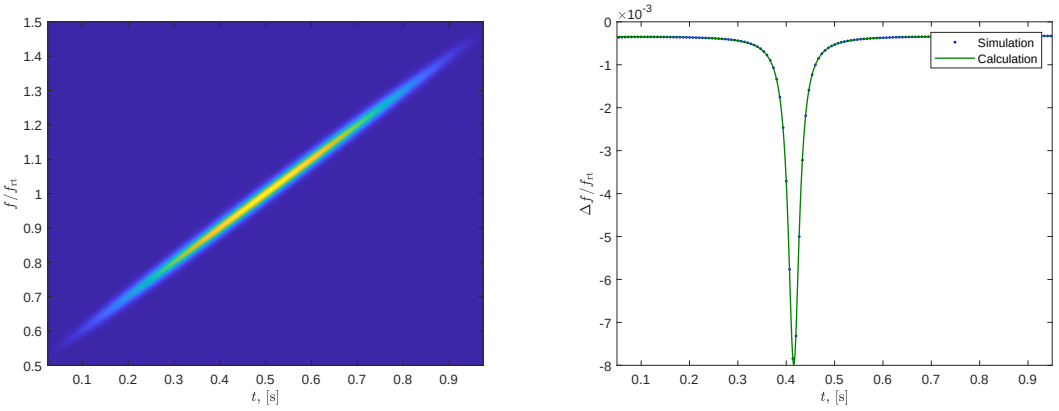

Figure 3.14: Example signal 1. Original GW signal has constant chirp. Left: GW spectrogram. Right: frequency shift between the original signal and detected signal.

where $b = \frac{d\omega(t)}{dt}$ is the chirp of the original signal and $\tau(\omega)$ is the signal time delay for corresponding frequency. For the signals discussed in this section $b \gg 1/\sigma_t^2$, giving us the frequency shift

$$\Delta f(t) = \frac{\tau(\omega(t))c(t)}{2\pi}. \tag{3.37}$$

This frequency shift is proportional to the τ parameter which is unbound next to critical frequencies. Therefore, the frequency shift also will be unbound when the instantaneous frequency of the signal will approach multiple of FSR. At the same time amplitude of the signal will decrease. Approximately, the frequency shift has the same order of magnitude as the change of the signal frequency within one round-trip time of the interferometer.

To measure how well the actual frequency agrees with the theoretical approximation described above, we run numerical simulations for different signals. We use the interferometer with 100 km arm length ($f_{\rm rt}$ = 1.5 kHz) and signal length of 1 second. We vary the frequency in the signal from 0.5 FSR to 1.5 FSR during the test. We took the source at an angle 89° relative to the arm, which is close to the critical angle at 1 FSR.

We performed numerical calculations of a gravitational wave signal by applying the interferometer transfer function to the signal in frequency domain, followed by the inverse Fourier transform. We then apply Hilbert transform to build the analytical version of the detected signal, and find the phase and the frequency as functions of time from the Hilbert transform. The resulting predictions are shown in Figs. 3.14 and 3.15.

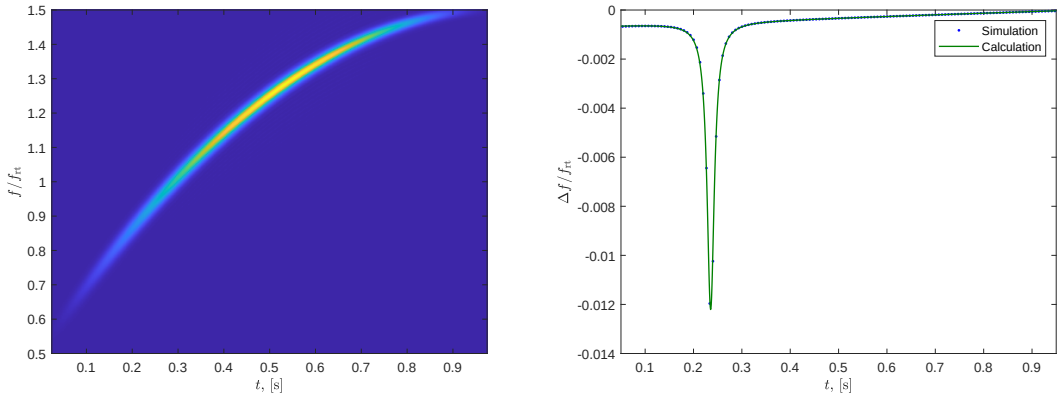

Figure 3.15: Example signal 2. Original GW has quadratic chirp. Left: GW spectrogram. Right: frequency shift between the original signal and detected signal.

CHAPTER 4

ZEROS OF INTERFEROMETER TRANSFER FUNCTION

For the purpose of the following analysis we treat the gravitational-wave detector is a linear dynamic system. If we take the one-arm detector, this linear system has the transfer function defined by equation (1.73). In the theory of linear dynamic systems one of the most important characteristics of the system are the poles and zeros of its transfer function [96]. The transfer functions of the one-arm and Michelson interferometer do not have poles. However, they have countable infinite number of zeros. To find these zeros we need to solve the transcendental equation in the complex plane. This seems to be a very difficult task.

To simplify this problem, we find the relationship between the real and imaginary parts of the zeros of the one-arm detector transfer function and use it to reduce the problem to one-dimensional transcendental equation. To find the solution of this transcendental equation numerically, we identify the regions where only one root of this equation is present. This semi-analytical approach allows us to find all roots of the one-arm detector transfer function using the method of bisections.

The Michelson interferometer has two transfer functions, one for plus and one for cross polarizations of the gravitational wave. The final response of the interferometer depends on the polarization of the gravitational wave which effectively combines + and × transfer functions into one quantity. This operation changes the zeros of the interferometer response transfer function. However, we found regions in the sky where transfer functions for both polarization share the same zeros. These points are based on the solution for zeros for the one-arm detector transfer function that we found before.

In addition to the zeros we define critical points for the transfer functions. These critical points correspond to the locations on the sky and source frequencies at which the interferometer has zero

sensitivity. In terms of the transfer function zeros, the critical points are imaginary zeros. We show that the critical points of the Michelson interferometer form a grid in the sky. The exact locations of the critical points for Michelson interferometer will be defined by critical points of the one-arm detector.

4.1 One-arm detector

For a one-arm detector the pole corresponds to the value of s for which the denominator in (1.73) turns to 0. This gives us a single pole at $s = 0$. However, for $s = 0$ the numerator also turns to 0. Therefore, the apparent pole at $s = 0$ is canceled by the matching zero.

All other values of s for which the transfer function turns to zero can be described by the transcendental equation

$$(1+\mu)\exp(sT) - 2\mu\exp(sT\mu) - (1-\mu)\exp(-sT) = 0. \tag{4.1}$$

We introduce the normalized parameter $\sigma = sT$ with real and imaginary parts $\sigma = \gamma + i\eta$. With the help of this notation, we can write two separate equations for the real and imaginary parts

$$\begin{aligned} (1+\mu)e^{\gamma}\cos(\eta) - 2\mu e^{\gamma\mu}\cos(\eta\mu) - (1-\mu)e^{-\gamma}\cos(\eta) = 0, \\ (1+\mu)e^{\gamma}\sin(\eta) - 2\mu e^{\gamma\mu}\sin(\eta\mu) + (1-\mu)e^{-\gamma}\sin(\eta) = 0. \end{aligned} \tag{4.2}$$

Next, we can multiply the first equation by $\sin(\eta)$ and the second equation by $\cos(\eta)$. Then add and subtract the resulting equations. These steps will lead to the new system of equations:

$$\begin{cases} (1+\mu)e^{\gamma}\sin(2\eta) = 2\mu e^{\gamma\mu}\sin(\eta(1+\mu)), \\ (1-\mu)e^{-\gamma}\sin(2\eta) = -2\mu e^{\gamma\mu}\sin(\eta(1-\mu)). \end{cases} \tag{4.3}$$

These equations may have solutions only when the left and right hand sides have the same sign. This sign depends also on μ. For simplicity, we will consider first positive values of μ and then

negative values. This condition gives us the system of inequalities for η:

$$\left[\begin{array}{l} \left\{\begin{array}{l} \sin(2\eta) > 0, \\ \sin(\eta(1+\mu)) > 0, \\ \sin(\eta(1-\mu)) < 0. \end{array}\right. \\ \left\{\begin{array}{l} \sin(2\eta) < 0, \\ \sin(\eta(1+\mu)) < 0, \\ \sin(\eta(1-\mu)) > 0. \end{array}\right. \end{array}\right. \tag{4.4}$$

Here, the square brackets mean that one of the conditions (inside the brackets) must be true, whereas the curly brackets mean that all of the conditions (inside the brackets) must be true.

From the system (4.4) we can find the intervals for η where it can have the solution:

$$\left[\begin{array}{l} \left\{\begin{array}{c} \pi n < \eta < \pi n + \pi/2, \\ \pi\dfrac{2m}{1+\mu} < \eta < \pi\dfrac{2m}{1+\mu} + \pi\dfrac{1}{1+\mu}, \\ \pi\dfrac{2k}{1-\mu} - \pi\dfrac{1}{1-\mu} < \eta < \pi\dfrac{2k}{1-\mu}, \end{array}\right. \\ \left\{\begin{array}{c} \pi n - \pi/2 < \eta < \pi n, \\ \pi\dfrac{2m}{1+\mu} - \pi\dfrac{1}{1+\mu} < \eta < \pi\dfrac{2m}{1+\mu}, \\ \pi\dfrac{2k}{1-\mu} < \eta < \pi\dfrac{2k}{1-\mu} + \pi\dfrac{1}{1-\mu}, \end{array}\right. \end{array}\right. \tag{4.5}$$

where n, m, k are integers. All of these intervals must overlap which gives us the relations for m and k:

$$\left[\begin{array}{l}\left\{\begin{array}{l}\dfrac{1+\mu}{2}n-\dfrac{1}{2}<m<\dfrac{1+\mu}{2}n+\dfrac{1+\mu}{4},\\ \dfrac{1-\mu}{2}n<k<\dfrac{1-\mu}{2}n+\dfrac{3-\mu}{4},\\ \dfrac{1-\mu}{1+\mu}m<k<\dfrac{1-\mu}{1+u}m+\dfrac{1}{1+\mu},\end{array}\right.\\ \left\{\begin{array}{l}\dfrac{1+\mu}{2}n-\dfrac{1+\mu}{4}<m<\dfrac{1+\mu}{2}n+\dfrac{1}{2},\\ \dfrac{1-\mu}{2}n-\dfrac{3-\mu}{4}<k<\dfrac{1-\mu}{2}n,\\ \dfrac{1-\mu}{1+\mu}m-\dfrac{1}{1+\mu}<k<\dfrac{1-\mu}{1+\mu}m.\end{array}\right.\end{array}\right. \tag{4.6}$$

To write the solution of the system (4.5) we introduce new variable $r=\{n(1+\mu)/2\}$, where $\{\cdot\}$ is a fractional part of a number. This allows us to express k and m in terms of n and r from (4.6) and substitute it to (4.5). After considering all possible cases we can simplify it to

$$\begin{cases}\pi n<\eta_n<\pi n+\min\left(\frac{1-2r}{1+\mu},\frac{2r}{1-\mu}\right)\pi & \text{for } 0<r<1/2,\\ \pi n-\min\left(\frac{2r-1}{1+\mu},\frac{2-2r}{1-\mu}\right)\pi<\eta_n<\pi n & \text{for } r>1/2,\end{cases} \tag{4.7}$$

where η_n is imaginary part of the zero that lies in the interval $(\pi n-\pi/2,\pi n+\pi/2)$. For $r=0$ and $r=1/2$ there are no solutions for the system (4.5). The intervals from (4.7) tell us where the equation (4.3) can have solutions. To find them we have to divide one equation by the other and express the real part of the root via its imaginary part:

$$\gamma_n=\frac{1}{2}\ln\left(-\frac{(1-\mu)\sin(\eta_n(1+\mu))}{(1+\mu)\sin(\eta_n(1-\mu))}\right). \tag{4.8}$$

We can also multiply both equations and substitute result for the real part of the root to obtain the transcendental equation for the imaginary part:

$$(1-\mu^2)\sin^2(2\eta)=4\mu^2\left(\frac{1-\mu}{1+\mu}\right)^{\mu}|\sin(\eta(1+\mu))|^{1+\mu}|\sin(\eta(1-\mu))|^{1-\mu}. \tag{4.9}$$

It is important to note that this equation can have only one solution within one of the intervals from (4.7). Within this interval $\sin(2\eta)$ has the same sign and has one extremum. At the same time one of the functions $\sin(\eta(1+\mu))$ or $\sin(\eta(1-\mu))$ becomes zero at one end of the interval, and it can not

have an extremal point within this interval. Thus, in equation (4.9) left and right hand sides have only one extremal point, and the maximum number of roots in this case can be two. However, at one end of the interval, when $\eta = \pi n$, the left side of the equation is zero and the right side is positive. At the other end of the interval the right side becomes zero and left side is positive. In this way, there should be an odd number of roots in this interval which means that there is only one root.

During the transformation of equation (4.2) we multiplied it by $\sin(\eta)$ and $\cos(\eta)$. We want to make sure that we did not add additional roots which may appear when $\sin(\eta) = 0$ or $\cos(\eta) = 0$.

For the case when $\sin(\eta) = 0$ equation (4.3) requires that $\sin\eta(1-\mu) = 0$ and $\sin\eta(1+\mu) = 0$. This happens when the product μn is integer. However, the real part of the zero (4.8) becomes undefined, so we need to find it from equation (4.2). Note that it automatically satisfies the second equation in (4.2). For the first equation, the solution for γ_n depends on parity of $(1+\mu)n$. If $(1+\mu)n$ is even, or $r = 0$, then n and μn have the same parity, all cosines in (4.2) have the same sign, leaving

$$(1+\mu)e^{\gamma} - 2\mu e^{\gamma\mu} - (1-\mu)e^{-\gamma} = 0. \tag{4.10}$$

This equation represents difference between two monotonic functions, therefore it can have only one solution. The solution is trivial: $\gamma = 0$. If $(1+\mu)n$ is odd, or $r = 1/2$, then $\cos\eta_n = -\cos\eta_n\mu$, and the real part of the zero can be found from equation

$$(1+\mu)e^{\gamma} + 2\mu e^{\gamma\mu} - (1-\mu)e^{-\gamma} = 0. \tag{4.11}$$

This equation also has only one solution. However, it is not a trivial one. The value of γ can be found using method of bisections.

Now let us consider the second case when $\cos\eta = 0$. From the first equation of the system in (4.2) it follows that $\cos(\eta\mu) = 0$. Then the second equation does not have solutions at all. Therefore, we did not introduce any new roots when we multiplied equation (4.2) by $\cos\eta_n$.

Special treatment is needed for limits when μ approaches 1 or -1. It requires finding the corre-

sponding limit of equation (3.8), which is

$$\begin{aligned}\tilde{D}(sT,1) &= \frac{1}{4sT}\left(1-e^{-2sT}+2sT\right),\\ \tilde{D}(sT,-1) &= \frac{1}{4sT}\left(1-e^{-2sT}+2sTe^{-2sT}\right).\end{aligned} \tag{4.12}$$

By setting these values to zero and doing some algebraic transformations we can write

$$\begin{cases} e^{1+2\sigma}(1+2\sigma) = e \quad u \to 1,\\ e^{1-2\sigma}(1-2\sigma) = e \quad u \to -1. \end{cases} \tag{4.13}$$

Therefore, a zero with index n can be expressed with n-th branch of the Lambert W function:

$$\begin{cases} \sigma_n = (W_n(e)-1)/2, \quad u \to 1,\\ \sigma_n = (W_{-n}(e)+1)/2, \quad u \to -1, \end{cases} \tag{4.14}$$

where e is Euler number. We set the branch for the Lambert function in the second equation to $-n$ to make sure that the imaginary parts of the zeros are the same for $u \to 1$ and $u \to -1$, and that the zeros do not have discontinuity when we approach $\mu = \pm 1$.

It is obvious that $\tilde{D}(s^*,\mu) = \tilde{D}^*(s,\mu)$. Additionally, using equations (4.7) and (4.3) we can write $\eta_n = -\eta_{-n}$. This gives us the first property of the zeros:

$$\sigma_{-n} = \sigma_n^*. \tag{4.15}$$

The second property comes from equation (4.2). This equation does not change if we replace μ with $-\mu$ and γ with $-\gamma$ which means that $\gamma(\mu)$ is an odd function, and $\eta(\mu)$ is an even function. It gives us the second property of the zeros:

$$\sigma_n(\mu) = -\sigma_n^*(-\mu). \tag{4.16}$$

This equation allows us to find the zeros of the transfer function (3.8) for negative μ.

One more property of the zeros is that the real part is non-negative for negative μ and non-

positive for positive μ:

$$\begin{cases} \gamma_n \geq 0, & \text{for } \mu < 0, \\ \gamma_n \leq 0, & \text{for } \mu > 0. \end{cases} \tag{4.17}$$

To find $\sigma_n(\mu)$ we use the following algorithm,

1. Calculate $\mu_p = |\mu|$
2. Find $r = n(1+\mu)/2$
   - If $r = 0$: Return value of $\sigma = i\pi n$
   - Else if $r = 1/2$: $\eta = \pi n$ and γ can be found from equation (4.11). Return the value of $\sigma = \gamma + i\eta$.
3. Find interval for η from equation (4.7)
4. Find η by searching solution of (4.9) on the interval from the previous step
5. Find γ from equation (4.8)
6. Return $\sigma = \gamma + i\eta$

The dependence of the zeros on μ is shown in Fig. 4.1. The zeros on the imaginary axis are of special interest. Only these zeros repeat for different values of μ. Moreover, these zeros have different dependence for even and odd n around $\mu = 0$. For odd n the real part of the zero changes linearly, thus producing smooth line on the complex plane. For even n the real part of the zero stays constant when μ passes through zero, producing a cusp in the graph.

4.2 Round-trip interferometer critical points

We shall now consider how the properties of the imaginary roots affect the interferometer response and the output signal. There is a number of discrete points $\eta_c = \Omega_c T$ and some particular values of $\mu_{c,j}$ for which $\tilde{D}(i\eta_c, \mu_{c,j}) = 0$. It means that the interferometer can not detect signals with frequencies Ω_n from the corresponding locations in the sky. The combination of these special frequencies and the directions on the sky will be called the critical points. The solutions for the critical points

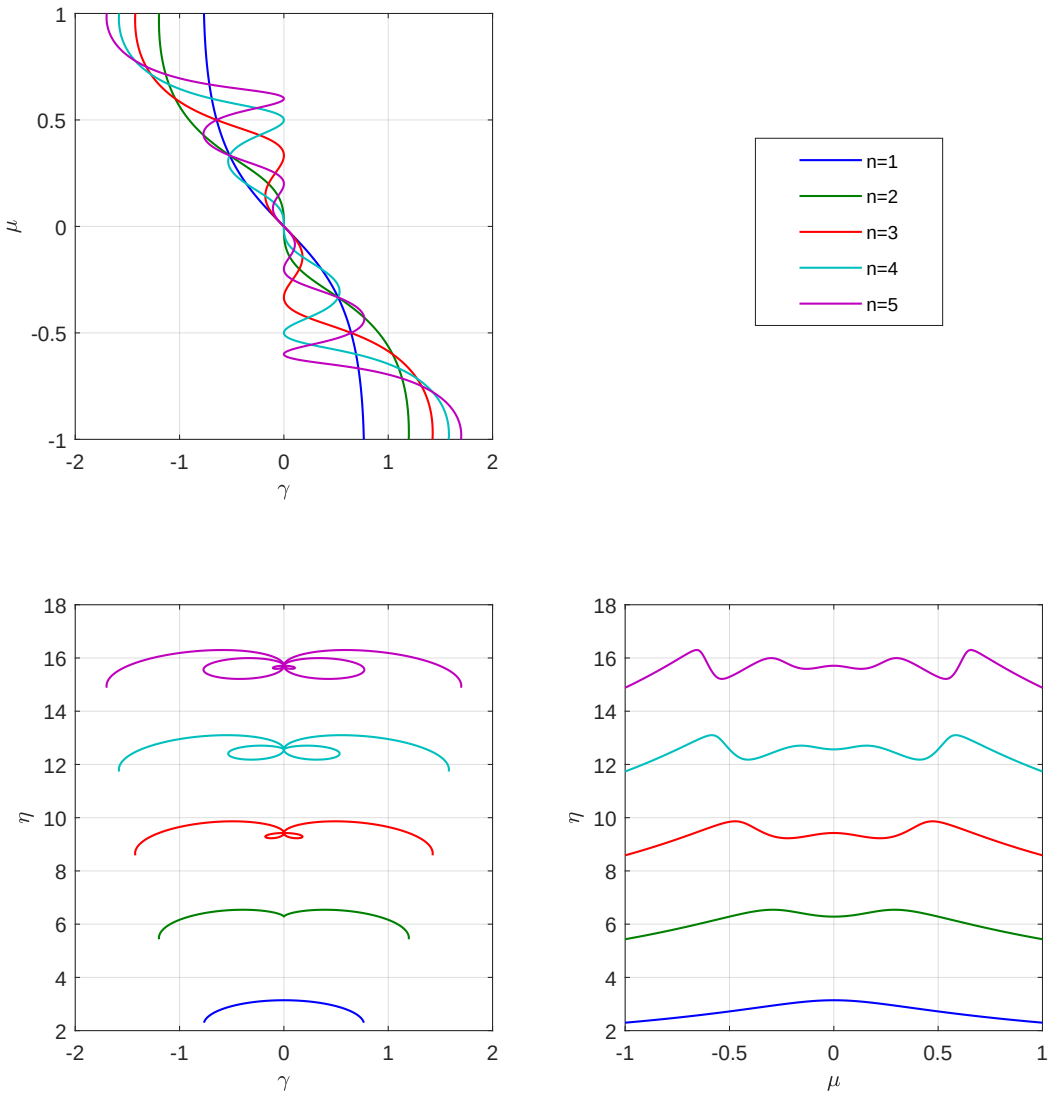

Figure 4.1: Dependence of one-arm detector transfer function zeros from source location. Top left and bottom right graphs represent dependence of real or imaginary part of the zero with direction, while on the bottom left graph shows movement of the zeros on complex plane when direction to the source changes.

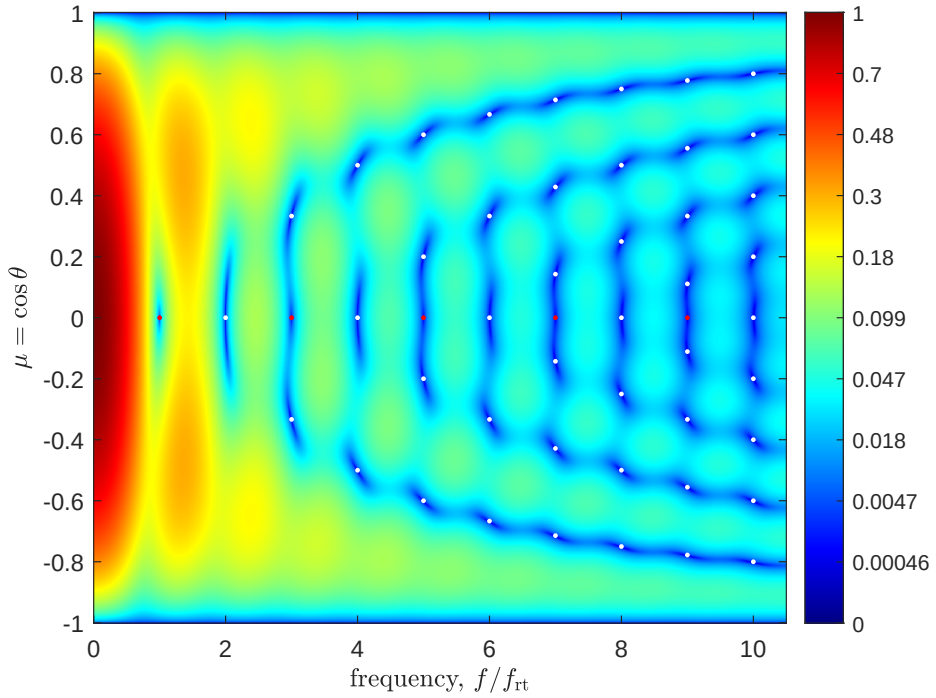

Figure 4.2: The absolute value of the one arm interferometer transfer function for different frequencies and source angles. White dots correspond to the zeros of the first kind and red dots correspond to the zeros of the second kind.

follow from the cases when $\eta = \pi n$ as well as when $\mu = 0$

$$\left[\begin{array}{l} \begin{cases} \eta_c = N \\ \mu_{c,j} = \dfrac{N-2j}{N} \end{cases} \\ \begin{cases} \eta_c = 2N-1 \\ \mu_c = 0 \end{cases} \end{array}\right. , \quad N \in \mathbb{N}, \quad 1 \le j \le N-1 \tag{4.18}$$

Graphical representation of the zeros of $\tilde{D}(i\eta, \mu)$ is shown in Fig. 4.2. There are two types of critical points. The first type corresponds to the signal frequency equal to Nf_{rt} with $N-1$ critical angles. The second type takes place only when N is odd and the direction to the sources is perpendicular to the interferometer arm.

The interferometer can not detect the signal at critical point but it can detect it next to the critical point. In such detection the interferometer transfer function next to these points behaves differently

for different types of critical points. For the first type the transfer function can be approximated as

$$\tilde{D}_1(i\eta,\mu) \approx \frac{1}{\eta_c}(\eta-\eta_c) - \frac{\mu_{c,j}}{1-\mu_{c,j}^2}(\mu-\mu_{c,j}). \tag{4.19}$$

For the second type the transfer function can be approximated as

$$\tilde{D}_2(i\eta,\mu) \approx \frac{1}{\eta_c}(\eta-\eta_c) - \frac{2i}{\eta_c}\mu. \tag{4.20}$$

Both of these transfer functions experience rapid change of phase from $-180°$ to $0°$ when the frequency is changing, but this jump is shifted for the type 1 critical point, and it happens for frequency

$$\eta = \eta_c\left(1+\frac{\mu_{c,j}(\mu-\mu_{c,j})}{1-\mu_{c,j}^2}\right). \tag{4.21}$$

The second type of the critical point experiences the jump exactly at the critical frequency η_c.

4.3 Michelson Interferometer

The signal from the photodetector is a mixture of the responses to + and × polarizations of the gravitational wave. This mixing adds another complex parameter to the interferometer transfer function: gravitational wave polarization. Complex zeros of the transfer function would change with the polarization, which complicates the general conclusion about the interferometer properties. Instead, we are looking for source locations such that the interferometer sensitivity will be zero no matter what kind of polarization the incoming gravitational wave carries. In other words, we are looking for a solution of equation

$$|\tilde{M}_+(s,\mu,\nu)|^2 + |\tilde{M}_\times(s,\mu,\nu)|^2 = 0. \tag{4.22}$$

If we change the gravitational-wave frame angle ψ the responses of Michelson interferometer will transform as a vector under rotation by 2ψ. Thus, if we find the point at which both sensitivities are zero, they will remain zero during the rotation of the vectors $\hat{\boldsymbol{p}}$ and $\hat{\boldsymbol{q}}$. Using this freedom of choice for the GW polarization frame we can set $\hat{\boldsymbol{p}}\cdot\hat{\boldsymbol{b}} = 0$. It is always possible to do so because vector $\hat{\boldsymbol{p}}$ can be anywhere in the plane perpendicular to $\hat{\boldsymbol{n}}$. So we either choose $\hat{\boldsymbol{p}}$ along $\hat{\boldsymbol{b}}\times\hat{\boldsymbol{n}}$ or, in case when

$\hat{\boldsymbol{n}} = \pm\hat{\boldsymbol{b}}$, vector $\hat{\boldsymbol{p}}$ is always perpendicular to $\hat{\boldsymbol{b}}$. In this case the Michelson interferometer response to cross polarization can be equal to 0 when one of these 3 conditions are met:

$$\hat{\boldsymbol{p}} \cdot \hat{\boldsymbol{a}} = 0, \tag{4.23}$$

$$\hat{\boldsymbol{q}} \cdot \hat{\boldsymbol{a}} = 0, \tag{4.24}$$

$$\tilde{D}(s, \mu) = 0. \tag{4.25}$$

For the case (4.23), the polarization vector $\hat{\boldsymbol{p}}$ is perpendicular to the plane of the interferometer, thus the source is in the plane of the interferometer. In this case the difference between arm-to-source angles θ_a and θ_b will be equal to the angle between the arms: $\alpha = |\theta_b - \theta_a|$, where $\mu = \cos\theta_a$ and $\nu = \cos\theta_b$, which can be written as

$$\cos\alpha = \mu\nu - \sqrt{1-\mu^2}\sqrt{1-\nu^2}, \tag{4.26}$$

or

$$\mu^2 + \nu^2 - 2\mu\nu\cos\alpha = \sin^2\alpha. \tag{4.27}$$

Additionally, if vector $\hat{\boldsymbol{p}}$ is perpendicular to $\hat{\boldsymbol{a}}$ and $\hat{\boldsymbol{b}}$, we can easily find that $(\hat{\boldsymbol{n}} \cdot \hat{\boldsymbol{a}})^2 = 1 - \mu^2$, $(\hat{\boldsymbol{n}} \cdot \hat{\boldsymbol{b}})^2 = 1 - \nu^2$. This gives us the following transcendental equation for s:

$$(1-\mu^2)\tilde{D}(s, \mu) - (1-\nu^2)\tilde{D}(s, \nu) = 0, \tag{4.28}$$

which can be transformed to

$$(\mu - \nu)\left(e^{sT} + e^{-sT}\right) - 2\left(\mu e^{sT\mu} - \nu e^{sT\nu}\right) = 0. \tag{4.29}$$

For the case (4.24) we are looking for the directions on the sky when $\hat{\boldsymbol{q}} = \pm\hat{\boldsymbol{a}} \times \hat{\boldsymbol{n}}/\sqrt{1-\mu^2}$ and $\hat{\boldsymbol{p}} = \pm\hat{\boldsymbol{b}} \times \hat{\boldsymbol{n}}/\sqrt{1-\nu^2}$. At the same time we know that $\hat{\boldsymbol{p}} \cdot \hat{\boldsymbol{q}} = 0$, which gives us the condition for the source direction

$$\mu\nu = \cos\alpha. \tag{4.30}$$

For example, if $\alpha = 90°$ then μ or ν should be equal to zero, which corresponds to the source location

at azimuth angles of 0, 90, 180, and 270 degrees.

The transcendental equation for the zeros is

$$\left(1-\mu^2\right)\tilde{D}(s,\mu)+\left(1-\nu^2\right)\tilde{D}(s,\nu)=0, \tag{4.31}$$

or after substitution of one-arm detector transfer function

$$2\left(e^{sT}-e^{-sT}\right)+(\mu+\nu)\left(e^{sT}+e^{-sT}\right)-2\left(\mu e^{sT\mu}+\nu e^{sT\nu}\right)=0. \tag{4.32}$$

Finally, for the last case (4.25) we need to have both $\tilde{D}(s,\mu)=0$ and $\tilde{D}(s,\nu)=0$. In cases when $\mu=\nu$ and the source is right between the interferometer arms the solutions for the zeros are the same as for the one-arm detector. But if $\mu\neq\nu$ then both responses can be zero only when the roots for different μ and ν are equal to each other which is possible only when $\mathrm{Re}\{sT\}=0$, as shown in Fig. 4.1. Therefore, the zeros of Michelson interferometer can exist only in special places on the map.

In summary, all equations that describe the zeros of Michelson interferometer are

$$\left[\begin{array}{l}
\begin{cases}\mu^2+\nu^2-2\mu\nu\cos(\alpha)=\sin^2(\alpha),\\ (\mu-\nu)\left(e^{sT}+e^{-sT}\right)-2\left(\mu e^{sT\mu}-\nu e^{sT\nu}\right)=0.\end{cases}\\
\begin{cases}\mu\nu=\cos(\alpha),\\ 2\left(e^{sT}-e^{-sT}\right)+(\mu+\nu)\left(e^{sT}+e^{-sT}\right)-2\left(\mu e^{sT\mu}+\nu e^{sT\nu}\right)=0.\end{cases}\\
\begin{cases}\tilde{D}(sT,\mu)=0,\\ \tilde{D}(sT,\nu)=0.\end{cases}
\end{array}\right. \tag{4.33}$$

These equations can be conveniently written in terms of μ and ν as coordinates that define the direction to the source on the sky. These coordinates represent $\hat{n}_x$ and $\hat{n}_y$ components when the interferometer arms are perpendicular. We can also derive $\hat{n}_x$ and $\hat{n}_y$ for an arbitrary angle between the arms:

$$\hat{n}_x=\frac{1}{\sin(\alpha)}\left(\mu\cos\left(\frac{\pi}{4}-\frac{\alpha}{2}\right)-\nu\sin\left(\frac{\pi}{4}-\frac{\alpha}{2}\right)\right), \tag{4.34}$$

$$\hat{n}_y=\frac{1}{\sin(\alpha)}\left(\nu\cos\left(\frac{\pi}{4}-\frac{\alpha}{2}\right)-\mu\sin\left(\frac{\pi}{4}-\frac{\alpha}{2}\right)\right). \tag{4.35}$$

4.4 Michelson interferometer critical points

The zeros of Michelson interferometer can exist only for sources located at the following areas in the sky:

- on the equatorial plane,
- between the arms when $\mu = \nu$,
- points where $\mu\nu = \cos(\alpha)$,
- points where transfer function for each arm is 0, so μ and ν satisfy equation (4.18).

Location in the sky where this zero is imaginary, together with the zero itself, corresponds to a critical point. All critical points can be described with this system of equations:

$$\left[\begin{array}{l}
\begin{cases}
\mu^2+\nu^2-2\mu\nu\cos\alpha=\sin^2\alpha,\\
(\mu-\nu)\cos\Omega T-\left(\mu\cos\Omega T\mu-\nu\cos\Omega T\nu\right)=0,\\
\mu\sin\Omega T\mu-\nu\sin\Omega T\nu=0.
\end{cases}\\
\begin{cases}
\mu\nu=\cos\alpha,\\
(\mu+\nu)\cos\Omega T-\mu\cos\Omega T\mu-\nu\cos\Omega T\nu=0,\\
2\sin\Omega T-\mu\sin\Omega T\mu-\nu\sin\Omega T\nu=0.
\end{cases}\\
\begin{cases}
\sin\Omega T-\mu\sin\Omega T\mu=0,\\
\mu\cos\Omega T-\mu\cos\Omega T\mu=0,\\
\sin\Omega T-\nu\sin\Omega T\nu=0,\\
\nu\cos\Omega T-\nu\cos\Omega T\nu=0.
\end{cases}
\end{array}\right. \tag{4.36}$$

There are two source locations in the equatorial plane that we will call type 0 critical points. These points have elevation angle of $\theta = 0°$ and azimuth angles of 45° and 225°. At these points the interferometer response is always zero regardless of the frequency of the gravitational-wave signal. The additional points appear for azimuth angles of 135° and −45°, as shown in Fig. 4.3. The

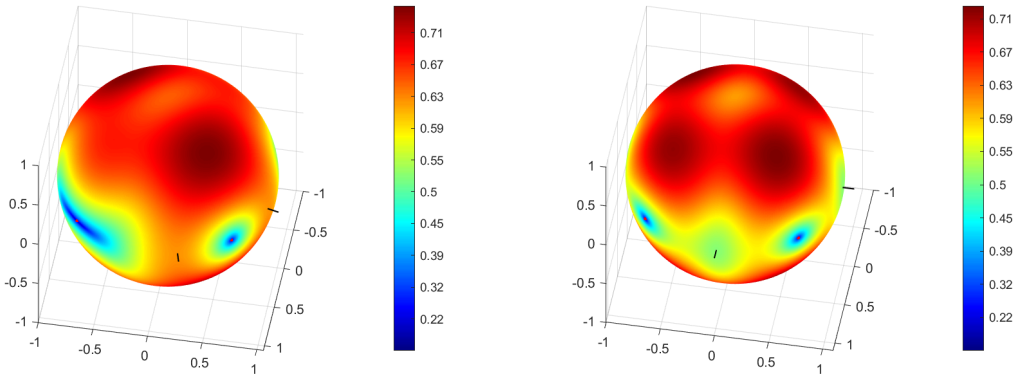

Figure 4.3: Examples of zeros for signal frequencies at non-integer FSR for the case (4.23). the left panel shows additional zero which appears for azimuth angle $-45°$ at frequency $4f_{\rm rt}/3$ for arm angle $60°$. The left panels shows the zero with the same azimuth that appear for signal frequency $4f_{\rm rt}/(2+\sqrt{2})$ and interferometer with angle between arms $90°$.

frequency of the gravitational wave at these critical points is described by the equation

$$\Omega T = \frac{2\pi N}{1 \pm \sin(\alpha/2)}. \tag{4.37}$$

This critical point will be called type 2 critical point. It has the same behavior as type 2 critical point of the one-arm detector: the frequency of the lowest sensitivity shifts with the small change of the source position.

The critical points for the source locations between interferometer arms, or when $\mu = \nu$, are a subset of the one-arm detector critical points. For these source locations $M_+ = 0$ and $M_\times$ turns to zero only when responses of both arms are zero.

For source locations that satisfy condition $\mu\nu = \cos(\alpha)$, the critical points are possible only for $\cos(\alpha) < 0$ and $\mu = \nu$, as show in Fig. 4.4. This solution comes from the solution of the transcendental equation

$$\sin\omega T = \mu \sin(\omega T \mu), \tag{4.38}$$

where $\mu = \sqrt{-\cos(\alpha)}$. This equation follows from (4.32) when we set $\mu = -\nu$. These points, similar to the equatorial critical points, are of type 2.

Finally, the critical points for Michelson interferometer for the case when each arm transfer function is zero are shown in Fig. 4.5. The third system has the solutions that are already described

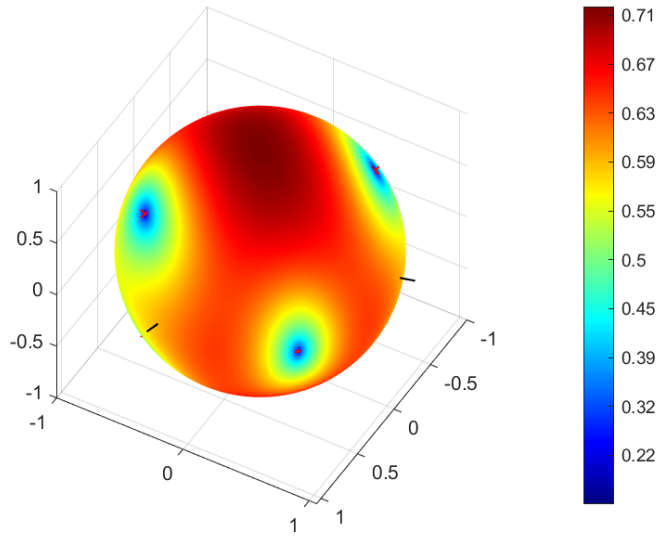

Figure 4.4: Example of the zero for the case in (4.24) that appears at low frequency approximately $0.752 f_{\mathrm{rt}}$ for azimuth 45° and elevation 35.26°. The angle between the arms is 120°. The zeros from the case (4.24) are marked with red cross, while zeros from the case (4.23) are marked with red dot.

in (4.18), and it will form a grid in the sky for frequencies equal to multiple of FSR. If both arms have type 1 critical point then corresponding critical point of the Michelson interferometer also belong to type 1. However, if at least one of the arms has type 2 critical point, then Michelson interferometer critical point is also of type 2. This can happen for sky locations along the directions perpendicular to the interferometer arms. The grid, formed by the critical points has two basis vectors $\hat{\boldsymbol{g}}_a$ and $\hat{\boldsymbol{g}}_b$. These vectors are orthogonal to the arm vectors: $\hat{\boldsymbol{g}}_a \cdot \hat{\boldsymbol{b}} = 0$ and $\hat{\boldsymbol{g}}_b \cdot \hat{\boldsymbol{a}} = 0$. This property has an important implication for critical point symmetry: they will overlap over rotation by the angle between $\hat{\boldsymbol{g}}_a$ and $\hat{\boldsymbol{g}}_b$. For example, for interferometer with arms angle 60°, the critical points will overlap if this interferometer will be rotated by 120°. Even if a point in the grit goes over the unit circle, it still makes a critical point, as demonstrated in the top right panel of Fig. 4.5. On this panel the transfer function approaches zero for source direction next to the interferometer arms, but it never reaches it.

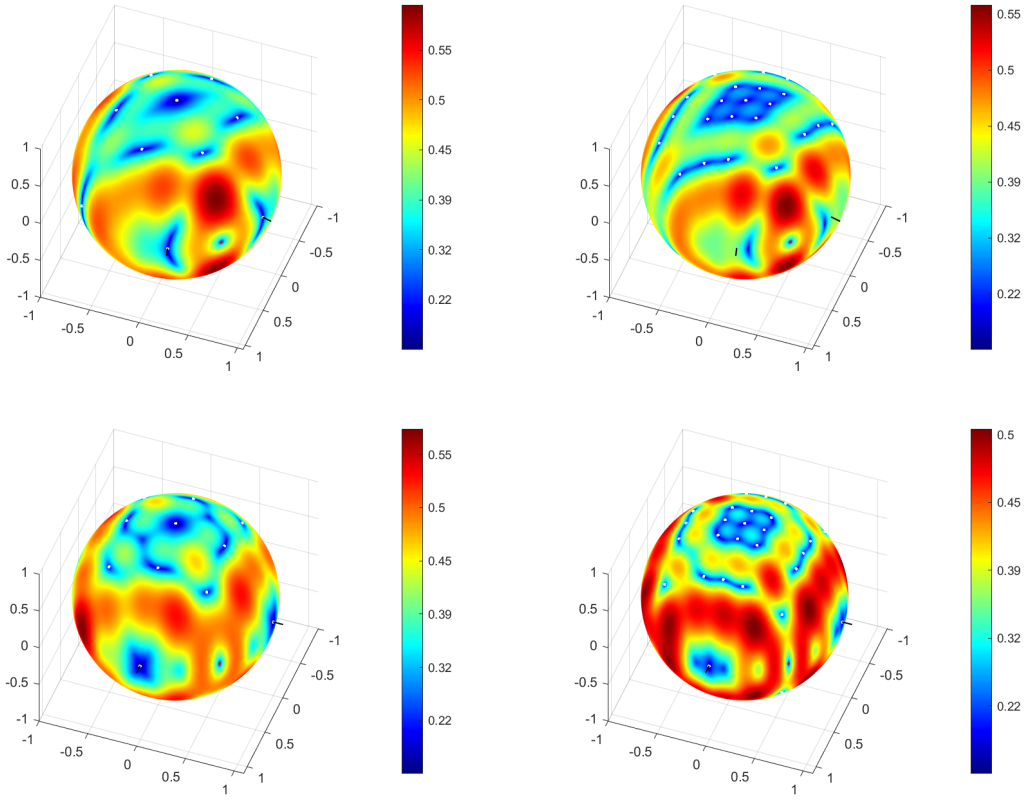

Figure 4.5: Michelson interferometer sensitivity for signal frequency at $4f_{\mathrm{rt}}$ (left) and $5f_{\mathrm{rt}}$ (right). Top plots correspond to the interferometer with 60° angle between arms, bottom plots correspond to the interferometer with 90° angle between arms. Interferometer arms are marked with black lines. The zeros corresponding to the case (4.25) are marked with white dots and zeros corresponding to the case (4.23) are marked with red dots. The red dot corresponds to only one solution when $u = v$.

CHAPTER 5

CONCLUSIONS

Summary of the Main Results

In this work we analyzed the propagation of gravitational-wave signals through laser interferometric detectors. We studied how these signals become distorted by the detectors and developed a mathematical formalism that allows us to calculate these distortions directly from the interferometer transfer function and its impulse response. We showed that the transfer function is completely defined by its zeros in the complex plane. We also derived the relationships between the real and imaginary parts of the zeros that were crucial for the development of effective computation of the zeros on the computer. These analytical equations allowed us to introduce the method of bisections for numerical calculations of the zeros with arbitrarily high precision. Based on these results we were able to identify signal frequencies and source locations that we called critical points. At the critical point the source location corresponds to the zero with a small real part; the critical frequency then equals the imaginary part of the zero. In the vicinity of these critical points the signal distortions are extreme.

In addition to the phase delay the signal has the group delay which is defined by the phase of the interferometer transfer function. We derived the analytical equation for the group delay and analyzed how the group delay depends on the source location and the signal frequency. Moreover, we showed that the group delay can be negative for some source locations on the sky. This can be seen in the appearance of the peak of signal amplitude in the interferometer before the arrival of the corresponding peak of the gravitational wave. We showed that this effect appears only for signals with smooth envelopes and narrow bandwidths. For signals that have abrupt changes of the

amplitude the normal or positive delay takes place.

Other distortions that we derived from the interferometer transfer functions are the frequency shift, frequency chirp, and signal broadening. These distortions are applicable to any quasi-monochromatic signal. The frequency shift distortion causes the peak frequency of the signal to shift within its bandwidth. The frequency chirp distortion adds a linear trend to the frequency evolution of the signal, making it appear as a tilted line on the spectrogram. The signal broadening makes the line appear wider or narrower, changing its time span. Analytical equations are derived for these distortions.

The analysis of signal distortions is applied to study how the interferometer will filter the complicated gravitational-wave signals from Core Collapse Supernovae (CCSN). Here we distinguish three types of CCSN gravitational-wave features and show how they become distorted by the detector. We conducted numerical simulations of gravitational wave detection to estimate the distortions of each of these features. The results of these numerical simulations agree well with the analytical calculations except when the source location and the signal frequency approached the critical points.

The first feature in our analysis is the supernova core bounce. It experiences the biggest distortion during the detection. We described symmetry properties of the distortions on the example of a short pulse. If the pulse originates from a source located in the plane bisecting the detector arms, it experiences a small time shift, has minor distortions, and mostly preserves the amplitude of its first peak. When the direction to the source is making an obtuse angle with both interferometer arms, the first peak becomes attenuated and stretched. Additionally, we observed copies of the signal or echoes that appear for detectors with photon round trip time greater than the pulse length. A detector with a Michelson configuration can produce up to four copies of the signal which appear in the moments defined by the angle between the source and the interferometer arms.

The second feature corresponds to the frequency-changing modes of CCSN gravitational waves such as p- and g-modes. We showed that the signal distortions will not affect the whole feature because the frequencies of these modes change in a wide range within the signal. However, the frequency shift added by the interferometer can be large when the frequency of the signal passes a critical point. In this case the mode splitting occurs at the critical frequency. This splitting can make a single mode appear as two different modes and thus confuse the interpretation of the signal during the data analysis stage.

The third feature is the quasi-monochromatic oscillations that appear in the CCSN gravitational-wave signal and is known as SASI mode. We showed that in addition to the time shift, the mode can change its frequency within its bandwidth, and acquire a chirp which can make it appear as a g-mode. Additionally, this feature can change its length due to the envelope broadening or focusing of the signal in time domain.

Implications for Future Gravitational Waves Searches

The distribution of the critical points in the sky can be used for optimization of a single detector and detector networks. We showed that there are special locations of critical points where the interferometer has low sensitivity for signals with frequencies equal to multiple of the FSR. Therefore, it is advantageous to arrange the network of detectors in such a way that the critical points of individual detectors do not overlap. We also found that future detectors with triangular configuration such as the Einstein Telescope or LISA space mission will have overlapping sets of critical points.

The location of critical points can be considered for optimization of future detectors for searches of CCSN signals. For ground based detectors, the maximum frequencies of the CCSN features will be on the order of the FSR. The most distorted features will be the core bounce and the core oscillation modes. The SASI mode has the lowest frequency. Therefore, we do not expect it to be significantly distorted during if detected by currently operational gravitational-wave detectors. For frequency of the signal near 2 FSR the critical points are located above and below the interferometer and in the plane of the interferometer arms. To optimize the location of the interferometer for known sources, such as the Milky Way galactic center, it is important to place the interferometer so that the source never crosses the critical point. It is possible to do so by choosing the latitude of the interferometer away from the declination of the source, as well as the declination $\pm 90°$. For space based interferometers, the frequencies of the CCSN features will be much higher than the FSR. In this case most of the sky will be filled with critical points. Consequently, precise location of the interferometer becomes less important. However, the signal distortions become more pronounced and their effect becomes more substantial. In this case, the analysis of signal distortions described in this work will be very useful for search algorithms and the subsequent waveform reconstruction.

Another result of this work that can be used for optimization of detector networks is the infor-

mation about the signal delay. This effect must accounted for when a gravitational wave signal from multiple detectors is used to find the source location in the sky. For signals with known frequency our analytical equations allow us to estimate systematic errors in source localization which are crucial for searches of the electromagnetic counterpart of the gravitational-wave source. Time shift can also have an impact on the CCSN waveforms. Different features of the signals have different frequencies. Therefore, they will be shifted by different time lags. This effect needs to be considered during the signal analysis. For example, the changes in the time lags become important when measuring the time between the core bounce and generation of shock instabilities.

The distortions of the bounce signal can affect coherent detection of the gravitational wave by a network of detectors because the bounce signals detected by interferometers with different orientations can have a substantially lower cross-correlation than the ideal signals. If such signals are detected, the source localization will be necessary to restore the original bounce signal. Additionally, the effect of echoes can lead to a wrong conclusion about the processes that happen during binary coalescence or CCSN. Fortunately, the present analysis makes it possible to improve localization of the source by measuring the time when each echo appears.

Precise localization of the source by electromagnetic observations can be aided by our model of the frequency detuning. Knowing the source position we can then remove the distortions of the CCSN modes over a wide range of frequencies including the p- and g-modes. These modes tend to have most of their power at the end of the frequency range. If this frequency is close to the detector FSR additional time-dependent frequency detuning will appear which can affect estimation of explosion parameters and how they change over time. The mathematical formalism developed in this work makes it possible to remove the systematic errors that these distortions introduce to the gravitational-wave signals and obtain precise estimation of the astrophysical properties of the supernova.

REFERENCES

[1] A. Einstein. “Approximative integration of the field equations of gravitation”. In: *The collected papers of Albert Einstein*. Vol. 14. Princeton University Press, 1987, pp. 201–210.

[2] J. H. Taylor and J. M. Weisberg. *A new test of general relativity - Gravitational radiation and the binary pulsar PSR 1913+16*. Feb. 1982. DOI: 10.1086/159690.

[3] R. A. Hulse and J. H. Taylor. “Discovery of a pulsar in a binary system.” In: *ApJ* 195 (Jan. 1975), pp. L51–L53. DOI: 10.1086/181708.

[4] J. Weber. “Observation of the Thermal Fluctuations of a Gravitational-Wave Detector”. In: *Phys. Rev. Lett.* 17.24 (Dec. 1966), pp. 1228–1230. DOI: 10.1103/PhysRevLett.17.1228.

[5] J. Weber. “Evidence for Discovery of Gravitational Radiation”. In: *Phys. Rev. Lett.* 22.24 (June 1969), pp. 1320–1324. DOI: 10.1103/PhysRevLett.22.1320.

[6] M. E. Gerstenshteĭn and V. I. Pustovoĭt. “On the detection of low frequency gravitational waves”. In: *Journal of Experimental and Theoretical Physics* 16.2 (1963), pp. 433–435.

[7] B. P. Abbott et al. “Observation of Gravitational Waves from a Binary Black Hole Merger”. In: *Phys. Rev. Lett.* 116.6 (Feb. 2016), p. 061102. DOI: 10.1103/PhysRevLett.116.061102.

[8] B. P. Abbott et al. “Properties of the Binary Black Hole Merger GW150914”. In: *Phys. Rev. Lett.* 116.24 (June 2016), p. 241102. DOI: 10.1103/PhysRevLett.116.241102.

[9] B. P. Abbott et al. “GW151226: Observation of Gravitational Waves from a 22-Solar-Mass Binary Black Hole Coalescence”. In: *Phys. Rev. Lett.* 116.24 (June 2016), p. 241103. DOI: 10.1103/PhysRevLett.116.241103.

[10] B. P. Abbott et al. “GW170104: Observation of a 50-Solar-Mass Binary Black Hole Coalescence at Redshift 0.2”. In: *Phys. Rev. Lett.* 118.22 (June 2017), p. 221101. DOI: 10.1103/PhysRevLett.118.221101.

[11] B. P. Abbott et al. “GW170608: Observation of a 19 Solar-mass Binary Black Hole Coalescence”. In: *Astrophys. J.* 851.2 (Dec. 2017), p. L35. DOI: 10.3847/2041-8213/aa9f0c.

[12] B. P. Abbott et al. “GW170814: A Three-Detector Observation of Gravitational Waves from a Binary Black Hole Coalescence”. In: *Phys. Rev. Lett.* 119.14 (Oct. 2017), p. 141101. DOI: 10.1103/PhysRevLett.119.141101.

[13] B. P. Abbott et al. “GW170817: Observation of Gravitational Waves from a Binary Neutron Star Inspiral”. In: *Phys. Rev. Lett.* 119.16 (Oct. 2017), p. 161101. DOI: 10.1103/PhysRevLett.119.161101.

[14] B. P. Abbott et al. “GW190425: Observation of a Compact Binary Coalescence with Total Mass $\sim 3.4\ M_{\odot}$”. In: *Astrophys. J.* 892.1 (Mar. 2020), p. L3. DOI: 10.3847/2041-8213/ab75f5.

[15] R. Abbott et al. “GW190412: Observation of a binary-black-hole coalescence with asymmetric masses”. In: *Phys. Rev. D* 102.4 (Aug. 2020), p. 043015. DOI: 10.1103/PhysRevD.102.043015.

[16] R. Abbott et al. “GW190814: Gravitational Waves from the Coalescence of a 23 Solar Mass Black Hole with a 2.6 Solar Mass Compact Object”. In: *Astrophys. J.* 896.2 (June 2020), p. L44. DOI: 10.3847/2041-8213/ab960f.

[17] R. Abbott et al. “GW190521: A Binary Black Hole Merger with a Total Mass of 150 $M_{\odot}$”. In: *Phys. Rev. Lett.* 125.10 (Sept. 2020), p. 101102. DOI: 10.1103/PhysRevLett.125.101102.

[18] B. P. Abbott et al. “GWTC-1: A Gravitational-Wave Transient Catalog of Compact Binary Mergers Observed by LIGO and Virgo during the First and Second Observing Runs”. In: *Phys. Rev. X* 9.3 (Sept. 2019), p. 031040. DOI: 10.1103/PhysRevX.9.031040.

[19] R. Abbott et al. *GWTC-2: Compact Binary Coalescences Observed by LIGO and Virgo During the First Half of the Third Observing Run*. Oct. 2020.

[20] B. P. Abbott et al. “Multi-messenger Observations of a Binary Neutron Star Merger”. In: *Astrophys. J.* 848.2 (Oct. 2017), p. L12. DOI: 10.3847/2041-8213/aa91c9.

[21] D. Pooley, P. Kumar, J. C. Wheeler, and B. Grossan. “GW170817 Most Likely Made a Black Hole”. In: *Astrophys. J.* 859.2 (May 2018), p. L23. DOI: 10.3847/2041-8213/aac3d6.

[22] R. Gill, A. Nathanail, and L. Rezzolla. “When Did the Remnant of GW170817 Collapse to a Black Hole?” In: *Astrophys. J.* 876.2 (May 2019), p. 139. DOI: 10.3847/1538-4357/ab16da.

[23] S. Ai et al. "The Allowed Parameter Space of a Long-lived Neutron Star as the Merger Remnant of GW170817". In: *Astrophys. J.* 860.1 (June 2018), p. 57. DOI: 10.3847/1538-4357/aac2b7.

[24] A. L. Piro, B. Giacomazzo, and R. Perna. "The Fate of Neutron Star Binary Mergers". In: *Astrophys. J.* 844.2 (July 2017), p. L19. DOI: 10.3847/2041-8213/aa7f2f.

[25] B. P. Abbott et al. "Exploring the Sensitivity of Next Generation Gravitational Gave Detectors". In: *Class. Quantum Grav.* 34.4 (Jan. 2017), p. 044001. DOI: 10.1088/1361-6382/aa51f4.

[26] A. Freise et al. "Triple Michelson Interferometer for a Third-Generation Gravitational Wave Detector". In: *Class. Quantum Grav.* 26.8 (Apr. 2009), p. 085012. DOI: 10.1088/0264-9381/26/8/085012.

[27] Karsten Danzmann et al. "LISA: laser interferometer space antenna for gravitational wave measurements". In: *Class. Quantum Grav.* 13.11A (1996), A247. DOI: 10.1088/0264-9381/13/11A/033.

[28] S. L. Larson, W. A. Hiscock, and R. W. Hellings. "Sensitivity curves for spaceborne gravitational wave interferometers". In: *Phys. Rev. D* 62.6 (Aug. 2000), p. 062001. DOI: 10.1103/PhysRevD.62.062001.

[29] N. J. Cornish and S. L. Larson. "Space missions to detect the cosmic gravitational-wave background". In: *Class. Quantum Grav.* 18.17 (2001), p. 3473.

[30] N. J. Cornish and L. J. Rubbo. "LISA response function". In: *Phys. Rev. D* 67.2 (2003), p. 022001.

[31] J. Luo et al. "TianQin: a space-borne gravitational wave detector". In: *Class. Quantum Grav.* 33.3 (Jan. 2016), p. 035010. DOI: 10.1088/0264-9381/33/3/035010.

[32] W.-H. Ruan, Z.-K. Guo, R.-G. Cai, and Y.-Z. Zhang. "Taiji program: Gravitational-wave sources". In: *Int. J. Mod. Phys. A* 35.17 (2020), p. 2050075. DOI: 10.1142/S0217751X2050075X.

[33] V. Srivastava et al. "Detection prospects of core-collapse supernovae with supernova-optimized third-generation gravitational-wave detectors". In: *Phys. Rev. D* 100.4 (Aug. 2019), p. 043026. DOI: 10.1103/PhysRevD.100.043026.

[34] C. Afle and D. A. Brown. "Inferring physical properties of stellar collapse by third-generation gravitational-wave detectors". In: *Phys. Rev. D* 103.2 (Jan. 2021), p. 023005. DOI: 10.1103/PhysRevD.103.023005.

[35] C. W Misner, K. S Thorne, and J. A. Wheeler. *Gravitation*. Macmillan, 1973.

[36] A. W. Alsabti and P. Murdin. *Handbook of Supernovae*. Springer, 2017. DOI: 10.1007/978-3-319-21846-5.

[37] S. Richers, C. D. Ott, E. Abdikamalov, E. O'Connor, and C. Sullivan. "Equation of state effects on gravitational waves from rotating core collapse". In: *Phys. Rev. D* 95.6 (Mar. 2017), p. 063019. DOI: 10.1103/PhysRevD.95.063019.

[38] P. Cerdá-Durán, N. DeBrye, M. A. Aloy, J. A. Font, and M. Obergaulinger. "GRAVITATIONAL WAVE SIGNATURES IN BLACK HOLE FORMING CORE COLLAPSE". In: *Astrophys. J* 779.2 (Dec. 2013), p. L18. DOI: 10.1088/2041-8205/779/2/l18.

[39] E. Abdikamalov, G. Pagliaroli, and D. Radice. *Gravitational Waves from Core-Collapse Supernovae*. 2020.

[40] T. Kuroda, K. Kotake, and T. Takiwaki. "A new gravitational-wave signature from standing accretion shock instability in supernovae". In: *Astrophys. J.* 829.1 (Sept. 2016), p. L14. DOI: 10.3847/2041-8205/829/1/l14.

[41] D. Radice, V. Morozova, A. Burrows, D. Vartanyan, and H. Nagakura. "Characterizing the Gravitational Wave Signal from Core-collapse Supernovae". In: *Astrophys. J* 876.1 (Apr. 2019), p. L9. DOI: 10.3847/2041-8213/ab191a.

[42] K. Kotake. "Multiple physical elements to determine the gravitational-wave signatures of core-collapse supernovae". In: *Comptes Rendus Physique* 14.4 (2013), pp. 318–351. ISSN: 1631-0705. DOI: 10.1016/j.crhy.2013.01.008.

[43] E. Abdikamalov, S. Gossan, A. M. DeMaio, and C. D. Ott. "Measuring the angular momentum distribution in core-collapse supernova progenitors with gravitational waves". In: *Phys. Rev. D* 90.4 (Aug. 2014), p. 044001. DOI: 10.1103/PhysRevD.90.044001.

[44] C. D. Ott. "The gravitational-wave signature of core-collapse supernovae". In: *Class. Quantum Grav.* 26.6 (Feb. 2009), p. 063001. DOI: 10.1088/0264-9381/26/6/063001.

[45] K. Hayama et al. "Determination of the angular momentum distribution of supernovae from gravitational wave observations". In: *Class. Quantum Grav.* 25.18 (Sept. 2008), p. 184022. DOI: 10.1088/0264-9381/25/18/184022.

[46] C. D. Ott et al. “General-relativistic simulation of three-dimensional core-collapse supernovae”. In: *The Astrophysical Journal* 768.2 (Apr. 2013), p. 115. DOI: 10.1088/0004-637x/768/2/115.

[47] J. M. Blondin, A. Mezzacappa, and C. DeMarino. “Stability of Standing Accretion Shocks, with an Eye toward Core-Collapse Supernovae”. In: *The Astrophysical Journal* 584.2 (Feb. 2003), pp. 971–980. DOI: 10.1086/345812.

[48] K. N. Yakunin et al. *Gravitational Wave Signatures of Ab Initio Two-Dimensional Core Collapse Supernova Explosion Models for 12-25 Solar Masses Stars*. 2015.

[49] K. N. Yakunin et al. *Gravitational wave signals from multi-dimensional core-collapse supernova explosion simulations*. 2017.

[50] H. Andresen, B. Müller, E. Müller, and H.-Th. Janka. “Gravitational wave signals from 3D neutrino hydrodynamics simulations of core-collapse supernovae”. In: *Mon. Not. R. Astron. Soc* 468.2 (Mar. 2017), pp. 2032–2051. ISSN: 0035-8711. DOI: 10.1093/mnras/stx618.

[51] A. Mezzacappa et al. “Gravitational-wave signal of a core-collapse supernova explosion of a 15 $M_\odot$ star”. In: *Phys. Rev. D* 102.2 (July 2020), p. 023027. DOI: 10.1103/PhysRevD.102.023027.

[52] J. Powell and B. Müller. “Three-dimensional core-collapse supernova simulations of massive and rotating progenitors”. In: *Mon. Not. R. Astron. Soc.* 494.4 (Apr. 2020), pp. 4665–4675. ISSN: 0035-8711. DOI: 10.1093/mnras/staa1048.

[53] A. Torres-Forné, P. Cerdá-Durán, M. Obergaulinger, B. Müller, and J. A. Font. “Universal Relations for Gravitational-Wave Asteroseismology of Protoneutron Stars”. In: *Phys. Rev. Lett.* 123.5 (July 2019), p. 051102. DOI: 10.1103/PhysRevLett.123.051102.

[54] V. Morozova, D. Radice, A. Burrows, and D. Vartanyan. “The Gravitational Wave Signal from Core-collapse Supernovae”. In: *Astrophys. J* 861.1 (June 2018), p. 10. DOI: 10.3847/1538-4357/aac5f1.

[55] H. Sotani and T. Takiwaki. “Avoided crossing in gravitational wave spectra from protoneutron star”. In: *Mon. Not. R. Astron. Soc.* 498.3 (Aug. 2020), pp. 3503–3512. DOI: 10.1093/mnras/staa2597.

[56] M.-A. Bizouard et al. *Inference of proto-neutron star properties from gravitational-wave data in core-collapse supernovae*. 2020.

[57] M. Rakhmanov. "Response of test masses to gravitational waves in the local Lorentz gauge". In: *Phys. Rev. D* 71.8 (2005), p. 084003.

[58] F. B. Estabrook and H. D. Wahlquist. "Response of Doppler spacecraft tracking to gravitational radiation". In: *Gen. Rel. Grav.* 6.5 (1975), pp. 439–447. DOI: 10.1007/BF00762449.

[59] R. W. Hellings. "Electromagnetically-tracked free-mass gravitational wave antennas". In: *Lecture Notes in Physics, Berlin Springer Verlag*. Vol. 124. 1983, pp. 485–493.

[60] M. Rakhmanov, J. D. Romano, and J. T. Whelan. "High-frequency corrections to the detector response and their effect on searches for gravitational waves". In: *Class. Quantum Grav.* 25.18 (2008), p. 184017. DOI: 10.1088/0264-9381/25/18/184017.

[61] T. T. Fricke et al. "DC readout experiment in Enhanced LIGO". In: *Class. Quantum Grav.* 29.6 (Feb. 2012), p. 065005. DOI: 10.1088/0264-9381/29/6/065005.

[62] A. D. Viets et al. "Reconstructing the calibrated strain signal in the Advanced LIGO detectors". In: *Class. Quantum Grav.* 35.9 (Apr. 2018), p. 095015. DOI: 10.1088/1361-6382/aab658.

[63] H. Andresen et al. "Gravitational waves from 3D core-collapse supernova models: The impact of moderate progenitor rotation". In: *Mon. Not. R. Astron. Soc* 486.2 (Apr. 2019), pp. 2238–2253. ISSN: 0035-8711. DOI: 10.1093/mnras/stz990.

[64] H. Dimmelmeier, C. D. Ott, A. Marek, and H.-Th. Janka. "Gravitational wave burst signal from core collapse of rotating stars". In: *Phys. Rev. D* 78.6 (Sept. 2008), p. 064056. DOI: 10.1103/PhysRevD.78.064056.

[65] Müller, E., Janka, H.-Th., and Wongwathanarat, A. "Parametrized 3D models of neutrino-driven supernova explosions - Neutrino emission asymmetries and gravitational-wave signals". In: *Astron. Astrophys* 537 (2012), A63. DOI: 10.1051/0004-6361/201117611.

[66] E. P. O'Connor and S. M. Couch. "Exploring Fundamentally Three-dimensional Phenomena in High-fidelity Simulations of Core-collapse Supernovae". In: *Astrophys. J* 865.2 (Sept. 2018), p. 81. DOI: 10.3847/1538-4357/aadcf7.

[67] J. Powell and B. Müller. "Gravitational wave emission from 3D explosion models of core-collapse supernovae with low and normal explosion energies". In: *Mon. Not. R. Astron. Soc* 487.1 (May 2019), pp. 1178–1190. ISSN: 0035-8711. DOI: 10.1093/mnras/stz1304.

[68] S. Scheidegger, R. Käppeli, S. C. Whitehouse, T. Fischer, and M. Liebendörfer. "The influence of model parameters on the prediction of gravitational wave signals from stellar core collapse". In: *Astron. Astrophys* 514 (2010), A51. DOI: 10.1051/0004-6361/200913220.

[69] N. J. Cornish and T. B. Littenberg. "Bayeswave: Bayesian inference for gravitational wave bursts and instrument glitches". In: *Class. Quantum Grav.* 32.13 (June 2015), p. 135012. DOI: 10.1088/0264-9381/32/13/135012.

[70] S. Klimenko, I. Yakushin, A. Mercer, and G. Mitselmakher. "A coherent method for detection of gravitational wave bursts". In: *Class. Quantum Grav.* 25.11 (May 2008), p. 114029. DOI: 10.1088/0264-9381/25/11/114029.

[71] J. McIver. "The impact of terrestrial noise on the detectability and reconstruction of gravitational wave signals from core-collapse supernovae". PhD thesis. University of Massachusetts at Amherst, 2015.

[72] J. Logue, C. D. Ott, I. S. Heng, P. Kalmus, and J. H. C. Scargill. "Inferring core-collapse supernova physics with gravitational waves". In: *Phys. Rev. D* 86.4 (Aug. 2012), p. 044023. DOI: 10.1103/PhysRevD.86.044023.

[73] J. Powell, S. E. Gossan, J. Logue, and I. S. Heng. "Inferring the core-collapse supernova explosion mechanism with gravitational waves". In: *Phys. Rev. D* 94.12 (Dec. 2016), p. 123012. DOI: 10.1103/PhysRevD.94.123012.

[74] S. Suvorova, J. Powell, and A. Melatos. "Reconstructing gravitational wave core-collapse supernova signals with dynamic time warping". In: *Phys. Rev. D* 99.12 (June 2019), p. 123012. DOI: 10.1103/PhysRevD.99.123012.

[75] R. Essick, S. Vitale, and M. Evans. "Frequency-dependent responses in third generation gravitational-wave detectors". In: *Phys. Rev. D* 96.8 (2017), p. 084004.

[76] L. A. Vaĭnshteĭn. "Propagation of pulses". In: *Sov. Phys. Uspekhi* 19.2 (1976), p. 189.

[77] L. Brillouin. *Wave propagation and group velocity*. Academic Press, 1960.

[78] R. L. Smith. “The velocities of light”. In: *Am. J. Phys.* 38.8 (1970), pp. 978–984.

[79] J. Peatross, S. A. Glasgow, and M. Ware. “Average Energy Flow of Optical Pulses in Dispersive Media”. In: *Phys. Rev. Lett.* 84.11 (Mar. 2000), pp. 2370–2373. DOI: 10.1103/PhysRevLett.84.2370.

[80] L. Cohen. *Time-frequency analysis*. Vol. 778. Prentice hall, 1995.

[81] J. B. Tary, R. H. Herrera, and M. van der Baan. “Analysis of time-varying signals using continuous wavelet and synchrosqueezed transforms”. In: *Philos. Trans. R. Soc. A* 376.2126 (2018), p. 20170254. DOI: 10.1098/rsta.2017.0254.

[82] C. G. B. Garrett and D. E. McCumber. “Propagation of a Gaussian light pulse through an anomalous dispersion medium”. In: *Phys. Rev. A* 1.2 (1970), p. 305.

[83] K. E. Oughstun. *Electromagnetic and Optical Pulse Propagation*. Vol. 2. Springer, 2019.

[84] R. Y. Chiao, E. L. Bolda, J. Bowie, J. Boyce, and M. W. Mitchell. “Superluminality and amplifiers”. In: *Progress in Crystal Growth and Characterization of Materials* 33.1 (1996), pp. 319–325. ISSN: 0960-8974. DOI: https://doi.org/10.1016/0960-8974(96)83663-1.

[85] W. Mitchell and R. Y. Chiao. “Negative group delay and “fronts” in a causal system: An experiment with very low frequency bandpass amplifiers”. In: *Physics Letters A* 230.3 (1997), pp. 133–138.

[86] T. Nakanishi, K. Sugiyama, and M. Kitano. “Demonstration of negative group delays in a simple electronic circuit”. In: *Am. J. Phys.* 70.11 (2002), pp. 1117–1121.

[87] M. Kitano, T. Nakanishi, and K. Sugiyama. “Negative group delay and superluminal propagation: an electronic circuit approach”. In: *IEEE Journal of Selected Topics in Quantum Electronics* 9.1 (2003), pp. 43–51.

[88] J. C. Garrison, M. W. Mitchell, R. Y. Chiao, and E. L. Bolda. “Superluminal signals: causal loop paradoxes revisited”. In: *Physics Letters A* 245.1 (1998), pp. 19–25.

[89] J. N. Munday and R. H. Henderson. “Superluminal time advance of a complex audio signal”. In: *Applied Physics Letters* 85.3 (2004), pp. 503–505. DOI: 10.1063/1.1773926.

[90] M. Rakhmanov. *Response of LIGO 4 km interferometers to gravitational waves at high frequencies and in the vicinity of the FSR (37.5 kHz)*. LIGO technical report T060237. Pasadena: California Institute of Technology, 2006.

[91] J. R. Wait. "Propagation of pulses in dispersive media". In: *Radio Sci. D* 69 (1965), pp. 1387–1401.

[92] D. E. Vakman and L. A. Vaĭnshteĭn. "Amplitude, phase, frequency—fundamental concepts of oscillation theory". In: *Sov. Phys. Uspekhi* 20.12 (Dec. 1977), pp. 1002–1016. DOI: 10.1070/pu1977v020n12abeh005479.

[93] D. Solli, R. Y. Chiao, and J. M. Hickmann. "Superluminal effects and negative group delays in electronics, and their applications". In: *Phys. Rev. E* 66.5 (2002), p. 056601.

[94] N. S. Bukhman and S. V. Bukhman. "On the negative delay time of a narrow-band signal as it passes through the resonant filter of absorption". In: *Radiophysics and Quantum Electronics* 47.1 (2004), pp. 68–76.

[95] A. Torres-Forné, P. Cerdá-Durán, A. Passamonti, and J. A. Font. "Towards asteroseismology of core-collapse supernovae with gravitational-wave observations – I. Cowling approximation". In: *Mon. Not. R. Astron. Soc* 474.4 (Mar. 2018), pp. 5272–5286. DOI: 10.1093/mnras/stx3067.

[96] P. J. Antsaklis and A. N. Michel. *Linear systems*. Springer Science & Business Media, 2006.